Advanced Laser Applications in Space Safety

PhD Thesis

Lewis Walker

Advanced Space Concepts Lab

Department of Mechanical and Aerospace Engineering

University of Strathclyde

August 30, 2022

Abstract

This thesis presents instrumentation models and mission simulations for three novel use cases of lasers in space.

Firstly, the use of laser ranging in a gravimetry experiment to estimate the masses of near-Earth asteroids and other small solar system objects is presented in the context of a dual-flyby CubeSat mission. The technique is shown to be capable of estimating the mass of small bodies to better accuracy and lower mass than has previously been demonstrated using traditional radioscience.

Secondly, a new method of laser ranging relevant to the above mission scenario is proposed and simulated, which utilises a CCD array as its primary sensor, along with a long-pulse or modulated CW laser. Despite the simple hardware, the new technique is shown to have great potential for precise range measurement which is sufficient for the application of asteroid mass estimation.

Finally, a mission concept for the removal of space debris using a small constellation of satellites carrying high-power lasers is proposed and simulated in detail to determine its impact on a debris population designed to represent a post-collision debris shell. A high-fidelity model of the reaction forces due to photon pressure and laser ablation is developed, which models these forces in more detail than in previous, similar mission concept studies. This interaction model is then used in the mission simulation to statistically determine the impact of the mission over a 10-year operation period. The concept is then adapted for the application of collision avoidance using photon pressure, investigating the achievable deflection of a debris fragment given some notice period, and the time until a threatening fragment passes close enough to a satellite in the constellation to be affected.

Declaration

This thesis is the result of the author's original research. It has been composed by the author and has not been previously submitted for examination which has led to the award of a degree.

Signed: Lewis Walker

Date: 30 August 2022

Acknowledgements

I would like to acknowledge and thank my primary supervisor, Max Vasile, for guidance over the course of my PhD, for his feedback and input to my research, and for continually holding me and my work to a high standard.

I would also like to thank Matthew Warden, Simon Sorensen and John-Mark Hopkins from Fraunhofer CAP for their help and guidance in the lab. Although the practical aspect of my PhD was rudely interrupted by COVID-19 and the focus subsequently shifted to the simulation work at MAE, I nonetheless gained valuable skills working with you in the laser lab which I hope may be useful in the future.

Finally, thank you to my friends Richard Bownes and Maxine Bantleman for proof reading my thesis, giving advice on thesis preparation and the viva, and spending many hours in viva rehearsals before the big day!

This work was funded by the University of Strathclyde and Fraunhofer UK's Centre for Applied Photonics, who I would like to thank for enabling this work to be undertaken for my PhD research.

Contents

Chapter 1

Introduction

The space environment presents many hazards to not only crewed spacecraft, but also uncrewed satellites and even the human presence on Earth's surface. These hazards include satellite-satellite and satellite-debris collisions, the extreme radiation environment outside of the protective magnetosphere of Earth, and even the existential threat of impacts from massive near-Earth objects such as asteroids.

Space agencies around the world are actively working on monitoring these threats and developing remediation methods accordingly. For example, ESA's Space Situational Awareness (SSA) programme, comprised of three main segments dedicated to space weather monitoring, near-Earth object tracking and detection, and space debris tracking, was started in 2009 to address these threats. These three areas pose differing levels of threat, from existential (asteroid impact) to societal (disruption or loss of existing space infrastructure and inability to deploy new space assets due to debris). However, since the existential threat of asteroid impact is balanced by a relatively low probability, and the societal threat of space debris is a near-certainty with inaction, the risk levels is comparable. Space debris tracking and remediation is likely the most pressing issue currently, with mega-constellations such as Starlink and OneWeb beginning to go online (however, Starlink's low altitude orbital regime significantly reduces the negative impact of any debris creation event due to relatively short fragment lifetime). Near-Earth asteroid tracking may be considered primarily a monitoring

effort at this point in time and thus lower priority in terms of funding allocation, as it is estimated that the majority of objects of concerning size having already been identified. Space weather will continually pose a moderate level of risk to space assets and infrastructure and monitoring should continue to be a priority, particularly as society increases its reliance on space assets.

As the SSA programme is primarily focused on threat monitoring rather than remediation, it has relatively low developmental risk, with concerns primarily arising from general risks related to politics, insufficient funding and public support pervasive to most governmental space operations. These stem from an underestimation from the general public and policymakers regarding the severity of these threats, and the impact on society that could be brought by failing to address them adequately.

These topics are also the focus of much research in the global scientific space community. In recent years, several missions, for example OSIRIS-REx, Hayabusa2 and Rosetta (Lauretta et al., 2017; Watanabe et al., 2017; Glassmeier et al., 2007), have visited near-Earth objects in order to better understand, amongst other things, their structure, mass, density and composition. Although these missions did not have planetary defence as their primary motivation, the data returned is key information relevant to any future redirection attempt targeting such objects: for example, highly accurate orbit determination was required for rendezvous, and knowledge of physical characteristics such as mass, material/albedo and rotation rate can help better model the effects of solar radiation pressure on future trajectories. Information on the shape and internal mass distribution (from orbiter trajectories) may also be helpful to better inform strategies such as the gravity tractor. Since these were primarily scientific missions which all involved rendezvous and orbit insertion, the timescales were rather long (arriving at their targets after 27, 42 and 245 months respectively), influenced by the propellant constraint and expenditure required to rendezvous. In a planetary defence scenario, however, rapid response is paramount as it allows more time for small perturbations to the asteroid's orbit to compound, likely resulting in a larger Earth miss distance. Thus, techniques to gather information on redirec-

tion targets in a rapid, flexible way are needed. Only one attempt to prove the ability to affect asteroid orbits has been launched to date - the Double Asteroid Redirection Test (DART) mission (Michel et al., 2022), which arrived at the Didymos-Dimorphos binary asteroid system in September 2022, and successfully deployed a kinetic impactor which perturbed the orbit of Dimorphos, proving the viability of this strategy.

There has also been a growing effort to develop techniques for the remediation of risks posed by orbital debris. RemoveDebris (Forshaw et al., 2017) was a 2019 mission which demonstrated the capture of debris using two methods: a harpoon and a net. It also demonstrated the use of a deployable dragsail to safely deorbit the cleanup spacecraft along with the captured debris, removing it from orbit permanently. Other methods have been proposed such as releasing fine powders on near-radial suborbital trajectories (where the powder particles simply fall back to Earth, and induce high drag on passing fragments due to large relative velocities) (Ganguli et al., 2012), or using lasers to impart momentum at a distance (a topic discussed in detail in this thesis), but very few attempts to actually deploy or flight-prove active removal techniques have been made. Currently, most efforts are focussed on the prevention of future debris creation, ensuring satellites are disposed of safely at the end of operational lifetime and otherwise preventing collisions. The aforementioned strategies involving mechanical capture with a harpoon or net reside firmly in this category - requiring orbit matching and careful proximity navigation near to a specifically targeted piece of debris. While prevention is surely better than cure, it is almost inevitable that eventually, more collisions will occur, resulting in large clouds of debris which may preclude access to, or traversal of, the local region of space. In this eventuality, active removal or remediation methods must be available which are scalable to large numbers of fragments, which unfortunately is not the case with mechanical capture methods due to the huge propellant expenditure required to rendezvous with hundreds or thousands of fragments.

1.1 Applications of Lasers in Space

The tightly collimated, near single-frequency light produced by lasers has found wide-ranging applications in many space missions. Laser altimetry is the application of time-of-flight laser ranging to produce topographic maps of the surface of Earth, or equally other planetary bodies. Many Earth science missions such as ICESat-2 rely on laser technology to obtain high-resolution topographic maps of ice sheets (Schutz et al., 2005; Smith et al., 2019) and monitor changes over time. Laser altimetry is also used to obtain data on ocean height, canopy height and cloud coverage (Neuenschwander and Magruder, 2019; Kwok et al., 2019). The information returned by these scientific missions is absolutely crucial in monitoring climate change and weather patterns.

Earth observation missions often employ lasers in LIDAR (LIght Detection And Ranging) systems for weather monitoring and atmospheric science. LIDAR is a generalisation of laser ranging/altimetry - where the latter simply measures distance to a surface using time of flight, LIDAR systems such as the ALADIN instrument aboard Aeolus (Reitebuch et al., 2009; Paffrath et al., 2009) and many others, also exploit Mie and Rayleigh scattering from aerosols, microparticles and other substances in the atmosphere (Luo et al., 2015b) as well as the main peak from the ground reflection. This backscattered light along with its Doppler shift can be used to probe the atmosphere for the presence of pollutants and water vapour, as well as provide data on wind speed and direction relative to the beam propagation axis (by determining whether the scattered light is red- or blue-shifted) to inform weather prediction models. Laser based ranging is similar to e.g. radar ranging, however the potential for increased spatial resolution makes laser ranging more attractive for Earth imaging applications, at the cost of a poorer ability to penetrate cloud cover (Lefsky et al., 2005).

Laser ranging has also been used to gain precise knowledge of space debris orbits (Sang and Bennett, 2014) by measuring the evolution of their trajectories over multiple obervation arcs, in order to propagate trajectories with lower uncertainty to better assess collision risk than would be possible with angles-only

measurements. It has also been used for orbit determination of lunar satellites from Earth (Zuber et al., 2010), which helps characterise the perturbations in lunar orbit and the lunar interior density distribution by observing trajectory deviations from a constant-density model. Debris laser ranging has also been applied to probing the attitude motion evolution of the defunct satellite Envisat by measuring millimetre-scale changes in range measurements to attached retroreflectors (Kucharski et al., 2014), as well as measuring the influence of solar radiation pressure on defunct satellite orbits (Kucharski et al., 2017).

Lasers have also found other applications in space including intersatellite communication (Sodnik et al., 2010), chemical analysis of the Martian surface using laser induced breakdown spectroscopy (LIBS) (Wiens et al., 2012). Time-of-flight laser ranging has been used to produce high-resolution topological maps of other celestial bodies including Mars, Mercury and the Moon (Zuber et al., 1998; Smith et al., 2010a; Cavanaugh et al., 2007). OSIRIS-REx, a sample return mission to the asteroid Bennu, as part of its scientific payload carried the OLA instrument, a 1064 nm laser altimeter which it used to characterise the surface topology of Bennu (Barnouin et al., 2020), with the help of image data, to sub-metre accuracy. The NEAR-Shoemaker Laser Rangefinder (NLR) is another example of laser altimetry being used to characterise asteroid surface structure. ASTER is a planned Brazilian mission which will carry a laser rangefinder to the triple asteroid system 2001-SN263, again with the primary purpose of surface mapping, but also to be used to assist navigation in the approach phase of the mission (De Brum and Da Cruz, 2017).

1.2 Laser Applications in Space Safety

Various applications of lasers in space safety specifically have been proposed in the literature, particularly relating to space debris and PHA (Potentially Hazardous Asteroid) deflection, although no such mission concepts have progressed beyond the feasibility study phase.

Space debris removal by laser ablation has received considerable attention in

the literature. Laser ablation utilises high-energy pulsed lasers to vapourise material from the surface of debris fragments, creating a plume of gas and plasma which causes the fragment to accelerate in the anti-normal direction. Past research has unanimously demonstrated the viability of laser ablation as a mechanism by which to transfer momentum to small pieces of space debris, for example in the work of Schall (1991), as well as mission concepts such as L'ADROIT (Phipps, 2014) and ORION (Campbell, 1996), which will be discussed in more detail in Chapter 6. Ablation has also been proposed for the detumbling of large space debris such as rocket bodies and defunct satellites by inducing torque from the ablative reaction force (Vetrisano et al., 2015). This is a key capability for the removal of such objects, as rotation of large objects with considerable angular momentum must first be controlled before any mechanical manipulation may begin.

Laser ablation has also been discussed extensively as a method of deflecting asteroids and altering their rotation (Vetrisano et al., 2013, 2016). DE-STAR and DE-STARLITE (Lubin et al., 2016) are two related mission concepts designed for this purpose - using a high-powered laser array to ablate the surface of threatening asteroids, generating a perturbative thrust which, given sufficient time, could deviate an asteroid's trajectory away from an Earth collision. The DE-STARLITE concept was shown to be capable of deflecting a 325 m diameter asteroid by several Earth radii given up to 15 years' notice, although the notice period is heavily dependent on the available power and thus optical flux on the surface of the asteroid. The ablation of asteroid-like materials has also been validated experimentally in the lab (Gibbings et al., 2013; Sloane and Sedwick, 2020).

Momentum transfer via laser ablation has been experimentally demonstrated in several papers (Phipps et al., 2017; Wang, 2017; Phipps et al., 2004) during the course of experiments designed to measure the momentum coupling coefficients of various materials relevant to the space debris problem. The transfer of both linear and angular momentum has also been demonstrated under microgravity and near-vacuum conditions on Earth to perturb freefall trajectories of

a variety of material samples relevant to space debris such as PCB, steel and copper (Lorbeer et al., 2018). While most tested materials in that paper exhibited the expected behaviour - a change in velocity somewhat closely aligned with the beam propagation direction, the authors discovered that green gummy bears [1] actually accelerate in the opposite direction, toward the emitter, when illuminated with high-energy near-IR laser pulses. The authors propose that this is likely due to the soft material allowing total penetration such that vaporised material and solid fragments are expelled from the back of the sample, which is not possible in metals. While there are currently no known green gummy bears being tracked in low Earth orbit, the authors note that this effect may be relevant when considering debris composed of non-metallic and/or transparent materials, and that fragments composed of similar gel-like materials may be poor candidates for ablation-based intervention.

Although several mission concepts to influence debris orbits using lasers have been proposed, there is still work to be done to investigate the feasibility and effectiveness of these strategies. Target shape effects is one such area - most proposed mission concept studies use a heavily simplified method of approximating the net force achieved due to laser irradiation, such as assuming a flat surface or wrapping all shape effects into a single fixed efficiency reduction factor. Target shape effects on the imparted impulse vector from ablation have been considered both analytically (Liedahl et al., 2013) and through numerical simulations (Scharring et al., 2016), however the research performed on this is somewhat limited. It was shown that for more complex geometries, due to the distribution of local normal vectors and self-shadowing, the direction of the net impulse is highly sensitive to the orientation and shape of the target object (Scharring et al., 2016). This effect should be taken into consideration in all new mission concepts that are developed using lasers to impart momentum to debris.

Momentum may also be transferred using laser light below the ablation threshold via photon pressure, a combination of reflection and absorption of the inci-

[1] It is unknown if this effect is also exhibited by other colours of gummy bear. More research is needed.

dent light by the target object. While this mechanism produces a much smaller change in velocity than ablation (with a thrust coupling coefficient several orders of magnitude lower), it has been shown in multiple simulated mission concepts to be promising for debris collision avoidance using ground-based lasers with multiple passes (Yang et al., 2016; Bamann et al., 2020; Cordelli et al., 2022). As will be discussed in Chapter 6, ground-based laser systems suffer several limitations which may be circumvented by using a space-based platform. While concepts employing space-based platforms have been proposed, they are fewer than those using ground-based lasers, and all used ablation; none were identified which used photon pressure from space. Although the effect of solar radiation pressure on debris orbits has been studied (Casanova et al., 2015; Kucharski et al., 2017), no attempt has been made to affect debris orbits using photon pressure. While this is likely due to the far superior momentum coupling offered by ablation (direct comparisons are difficult due to one mechanism employing pulsed lasers and one using CW), photon pressure based interaction would likely face far fewer regulatory hurdles and safety concerns (due to lower potential for damage or physical harm in the event of an unintended object or person being in the beam path) than the high energy pulsed lasers required for ablation, and so the study of laser pressure as an interaction mechanism is still warranted. It would also be much easier to implement, as the thrust generated is far less sensitive to the surface fluence - as will be discussed, thrust generation by laser ablation has an optimal fluence, and relatively small deviations from the optimum can cause large reductions in momentum coupling due to plasma shielding, or even total cessation of ablation. Ensuring optimal fluence thus requires precise, variable, and quickly responsive beam focussing as well as good knowledge of the distance to the target which may be more easily attainable with a ground-based system. However, a ground-based system must deal with increased range to target, necessitating a larger aperture, as well as atmospheric attenuation reducing the fluence by the time the beam reaches the target. To keep the surface fluence close to the optimal level over a broad range of distances (as will be discussed in Chapter 6), the pulse energy must also be widely variable to adapt to changing conditions, making for a more

complex laser system. While the difficulties in implementation for laser ablation may well be solvable with future optics technology, the current state of the art for pulsed systems will likely require significantly more development effort to produce a working, scalable system compared to a CW system for photon pressure. Thus, more study on the use of photon pressure in debris mitigation is certainly warranted.

Although there are numerous applications of lasers in space safety, the deployment of high-powered lasers does of course pose its own safety risks - primarily due to the possibility of inadvertently illuminating an object other than the intended target, be it a space asset such as the ISS, or photosensitive infrastructure - even people - on the ground. Careful consideration should be made with regard to the pointing direction and timing of any laser operation in space, taking into account the orbits of other satellites in the vicinity, and certainly avoiding pointing of the laser toward Earth's surface while over major landmasses.

1.3 Thesis Motivations, Objectives and Methodology

This thesis addresses topics related to the latter two categories of ESA's SSA program. Firstly, a matter pertinent to planetary defence, the estimation of the masses of near-Earth objects with a novel gravimetry technique using intersatellite ranging in a dual-flyby configuration. Asteroid mass is a key parameter both to inform any future asteroid deflection attempts such as kinetic impactors or solar concentrators, as well as estimating the damage potential of smaller objects to determine if an intervention is warranted. While asteroid masses have been probed through other means, the masses that have been estimated in the past have been of kilometre-scale objects. While these are of course threatening, sub-kilometre asteroids are far more numerous, yet still large enough to pose significant risks to Earth. Also, many previous asteroid mass estimation techniques require the spacecraft to orbit the target body, requiring more propellant, a longer mission duration (response time is critical for a reconnaissance mission

to an Earth impactor), larger, more expensive spacecraft and also limiting any such mission to target only one object. A method suited to a fast flyby scenario would enable smaller, cheaper satellites to perform this measurement, with reduced propellant requirement and the possibility of visiting multiple targets with a single satellite and repeating the mass estimation experiment to better characterise and understand the solar system's NEA population. Such a method that is capable of visiting multiple asteroids may in the near future also find relevance in prospecting for asteroid mining.

Secondly, the thesis focuses on active remediation of existing small space debris by use of laser illumination from a distributed space-based satellite swarm. At orbital speeds, even small fragments pose a significant threat to satellites, however their low mass requires a small momentum change to adjust their trajectories, making laser illumination a more viable candidate than for larger objects. Space-based platforms offer the opportunity to circumvent many of the limitations of their ground-based counterparts due to the shorter distance to target, such as improved optical acquisition and reduced laser defocusing, as well as other factors such as lack of atmospheric attenuation and better alignment of the beam axis with the negative velocity direction. Additionally, in previous studies of laser-based debris intervention, low-fidelity models of the laser's interaction with the target objects were used, and there is a clear need for higher-fidelity models to be developed to more accurately simulate the effects of laser illumination.

To summarize, the motivations for the work in this thesis are:

- the need for a method to precisely probe the mass of a threatening asteroid in a fast flyby scenario, both to quickly estimate the mass of an Earth-threatening asteroid, and also enable mass measurement in multi-asteroid flyby missions, increasing scientific return,

- the need for further research to develop viable strategies for remediation of risks posed by large populations of space debris, particularly those fragments which are too small to be tracked from Earth, yet large enough to threaten operational space assets,

- the need for higher-fidelity models to simulate the effect of laser illumination on space debris.

The objectives of the work in this thesis were to investigate the feasibility of a novel method of asteroid mass estimation, and the feasibility of using laser illumination to affect the orbits of small space debris fragments. These were investigated through the development and use of mission and instrumentation simulations - in the case of the gravimetry experiment, spacecraft trajectories were propagated under the perturbative effects of a nearby asteroid's gravity field in a fast, dual flyby scenario. Inter-satellite range measurements from on-board laser rangefinders were used to recover the mass of the asteroid by fitting a dynamic model, parametric in the asteroid mass, to the simulated measurements. Different asteroid masses and a variety of flyby configurations were simulated to assess the system performance in a wide range of scenarios.

For the chapters on space debris remediation, a high-fidelity model was developed which allows simulation of the transferred momentum vector to arbitrarily shaped debris fragments from either photon pressure or laser ablation. A mission concept is then proposed using a constellation of satellites carrying laser sources, which illuminate passing fragments opportunistically and attempts to lower their orbits over a multi-year timeframe. The previously developed model is used to characterize in detail a subset of the identified viable encounter events, and the results of this characterisation are used to statistically assess the long-term impact of the proposed mission concept. The concept is then adapted to the objective of collision avoidance. The new high-fidelity model of laser-debris interaction is also used to investigate off-axis components of the applied $\Delta\mathbf{V}$ which has not previously been studied due to the lack of such a detailed interaction model.

1.4 Main Contributions

The main contributions of the work in thesis are as follows:

- Proposal and study of a novel gravimetry technique which is shown to allow

mass estimation of lighter asteroids, comets and other small bodies than has been achieved previously.

- Proof-of-concept for a novel method of laser ranging, using a standard CCD as the main sensor, which is shown to be capable of achieving high levels of range accuracy.

- Study of a new, constellation-based mission concept for space debris remediation using high-fidelity modelling of laser interaction to estimate mission impact.

During the course of the author's study period, several conference and journal papers were derived from the work presented in this thesis, a list of which can be found below.

- Walker, L., & Vasile, M. (2022). *Space debris surveillance and remediation using space-based lasers.* Advances in Space Research.

- Walker, L., & Vasile, M. (2021). *Mitigation of Debris in LEO using Space-Based Lasers.* In 72nd International Astronautical Congress, Dubai, United Arab Emirates.

- Walker, L., & Vasile, M. (2021). *Feasibility of Active Debris Mitigation Using Space-Borne Lasers.* In 8th European Conference on Space Debris, Darmstadt, Germany

- Walker, L., Di Carlo, M., Greco, C., Vasile, M., & Warden, M. (2021). *A Mission Concept for the Low-Cost Large-Scale Exploration and Characterisation of Near Earth Objects.* Advances in Space Research, 67(11), 3880-3908.

- Walker, L., Greco, C., Di Carlo, M., Wilson, A., Ricciardi, L., Berquand, A., & Vasile, M. (2019). *Nanospacecraft Exploration of Asteroids by Collision and Flyby Reconnaissance.* In 13th IAA Low-Cost Planetary Missions Conference, Toulouse, France.

- Walker, L., & Vasile, M. (2019). *Capabilities of a Nano-LIDAR for Future Reconnaissance Missions to NEOs.* In 70th International Astronautical Congress, Washington DC, USA

- Greco, C., Di Carlo, M., Walker, L., & Vasile, M. (2018). *Analysis of NEOs Reachability with Nano-satellites and Low-thrust Propulsion.* In 4S Symposium 2018-Small Satellites Systems and Services, Sorrento, Italy

1.5 Thesis Structure

This thesis begins with a brief overview of the history of laser technology and some previous applications in space, as well as a review of laser physics and basic principles of operation in Chapter 2. In Chapter 3, a novel technique for measuring the mass of asteroids is presented and its efficacy shown with simulations. The range of possible masses that may be probed with this technique is investigated, as well as testing different flyby configurations to determine better configurations to reach greater precision at lower masses.

Chapter 4 then presents a novel concept for laser ranging using a long-pulse laser and simple CCD sensor, compared with more complex instrumentation which is typically used. It is shown to have potential for highly precise inter-satellite ranging which would be sufficient for the application of asteroid mass estimation presented in Chapter 3.

In Chapter 5, a high-fidelity model of the interaction of laser light with arbitrary objects is presented, which allows the simulation of momentum transfer via both photon pressure and laser ablation, as well as its effects on object attitude motion. This model is then used in Chapter 6 to simulate the impact of a mission concept for space debris remediation, exploring the options of both debris removal and collision avoidance. Finally, Chapter 7 contains an overview of the work presented in the thesis and the results obtained. Each technical Chapter contains a detailed and focused review of literature relevant to the containing Chapter.

Chapter 2

Overview of Laser Physics, Applications and Operation

Lasers are an extremely useful technology with a wide range of both terrestrial and extraterrestrial applications. The theoretical basis of laser physics - absorption, spontaneous emission and stimulated emission of light by atoms - was first proposed in the early 20^{th} century (Einstein, 1917). Over the next several decades, Einstein's theory began to be experimentally validated, and optical pumping was proposed and demonstrated as a method of obtaining the excited states required for stimulated emission and amplification of light. This paved the way for the first so-called 'masers' in the 1950s - conceptually similar to a modern-day laser, but operating at microwave frequencies. In the late 50s, "optical masers" operating in the visible band were proposed along with resonator cavity designs, and the acronym LASER (Light Amplification by Stimulated Emission of Radiation) coined.

Subsequently, the first working optical laser was built in 1960 (Maiman et al., 1960) using ruby as the active medium, pumped optically by a simple flashlamp, to produce laser light at 694 nm. Due to the energy level structure of the ruby crystal used, this laser was only capable of pulsed operation. Soon afterwards, the first lasers employing gas and semiconductors as their active media were developed - using respectively a mixture of helium and neon, and gallium arsenide.

Since their invention, the tightly collimated, monochromatic light produced

by lasers has found a wide range of use cases. Some notable examples of laser applications include interferometry, which is used to detect changes in optical path length on the scale of the laser wavelength. This was instrumental in the first detection of gravitational waves by LIGO (Abbott et al., 2016). Other applications include spectrometry, laser ranging, LIDAR, laser cooling to near absolute zero, nuclear fusion research, and industrial processes such as welding, etching and 3D printing using metal substrates. Lasers have also found applications in medicine such as laser surgeries such as LASIK and treatment of some cancers. This list is far from exhaustive and continues to grow.

Lasers have also found many use cases in space. Perhaps the most common space-based usage of laser systems are applications involving ranging and LIDAR. Laser ranging is achieved by measuring the time of flight of laser pulses reflecting off of the target surface. Pure laser ranging/altimetry has been used in orbiters of extraterrestrial bodies to map elevation. The Mars Orbiter Laser Altimeter (MOLA) was an instrument carried aboard the Mars Global Surveyor orbiter, which remained in operation around Mars from 1997 until 2007. MOLA data allowed the construction of detailed elevation maps of the entire Martian surface from its pulsed 1064 nm laser, with a vertical accuracy on the order of several metres and horizontal uncertainty better than 100 metres (Gwinner et al., 2010). A similar instrument - the Lunar Orbiter Laser Altimeter (LOLA) was also used aboard the Lunar Reconnaissance Orbiter, achieving similar performance (Smith et al., 2010b). LOLA operates in a different manner, splitting its main beam into five individual beams, received by five corresponding sub-detectors to improve the resolution of its range measurements. Similar instrumentation was also used aboard the NEAR mission to obtain topographic measurements of the asteroid 433 Eros, achieving 2 m vertical accuracy and 31.5 cm horizontal resolution (Cole et al., 1996).

LIDAR offers an extension of the capabilities of pure rangefinding and is often used in meteorology and climate science. If the laser pulse is transmitted through a gaseous medium such as Earth's atmosphere without a solid target downrange, backscatter from aerosols, clouds or atmospheric boundaries may be

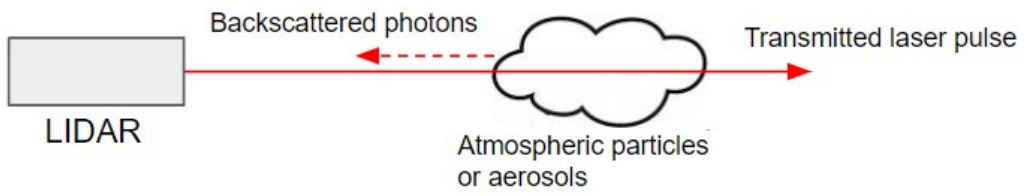

Figure 2.1: Illustration of backscatter LIDAR used for detection of atmospheric particles, aerosols etc.

detected (illustrated in Figure 2.1), as well as differential absorption at different wavelengths allowing detection of different compounds in the atmosphere such as water vapour, ozone or industrial emissions (Eloranta, 2008). Analysis of the Doppler shift of backscattered light from suspended particles also allows wind speed measurements to be taken using LIDAR.

Satellites employing LIDAR technology in Earth orbit are numerous - used also for climate science and meteorology, giving information on, for example, cloud coverage, changes in glaciation, forest coverage as well as some of the same outcomes from terrestrial LIDARs mentioned previously. Examples of such satellites include IceSAT-2 (Markus et al., 2017), ADM-Aeolus (Straume et al., 2018) and MERLIN (Ehret et al., 2017). LIDAR offers some key benefits over radar for these applications - primarily the potential for increased spatial resolution, and the ability to detect aerosols and suspended particles in the atmosphere which would not cause scattering for longer-wavelength radio waves. This comes at the cost of poorer penetration of cloud cover and foliage (Lefsky et al., 2005), making radar perhaps a better option for pure elevation mapping. However, this does enable LIDAR to gather data on cloud and foliage cover which would not be possible using radar.

Pulsed lasers have also been proposed and flight proven for communication purposes, encoding information into the pulse stream and enabling higher data transfer rates than traditional methods thanks to the availability of faster modulation technologies than is available with radio waves (Boroson and Robinson, 2015). The tighter collimation thanks to the shorter wavelength also enables a better-directed, more efficient mode of communication than radio.

One early stage technology whose applications are only beginning to be realised is the use of lasers to assist in formation flight by precisely monitoring the distance between two or more spacecraft. This opens the door to many new applications in astronomy, for example allowing far larger interferometer arms than would be feasible on Earth for the detection of gravitational waves. One proposal using formation flight in astronomy is the mission concept IRASSI (Linz et al., 2020), which proposes the use of five satellites flying in formation, using a high repetition rate femtosecond laser along with a frequency comb to monitor the relative position of the satellite swarm. This enables an extremely high spatial resolution in the astronomical observations taken from these satellites. Another application of precise formation flight is in exoplanet research - direct imaging of exoplanets is extrement challenging due to the light of the parent star being so much brighter than that coming from the planet. A deployable starshade could be used to block this unwanted light and enable direct imaging of orbiting planets. This would require precise formation flight between the starshade and the telescope, which would likely be enabled in part by laser technology, although improvements to orbit control technology would also be required to maintain highly precise relative position.

2.1 Laser Principles of Operation

Lasers operate by exploiting the process of stimulated emission of light. An electron in an excited state will naturally decay to its ground state, emitting a photon of energy equal to the traversed bandgap in the process. This process, however, may be prompted by interaction with a photon of energy equal to the bandgap, in which case the emitted photon will have equal phase and propagation direction to that of the stimulating photon. Thus this provides an amplification effect. Materials known as gain media - typically doped crystals or glasses which may be drawn into long fibres - which have convenient energy level structures, are used to provide this amplification over some traversal distance through the medium. While the first lasers used a single pass through the gain medium, resonant cav-

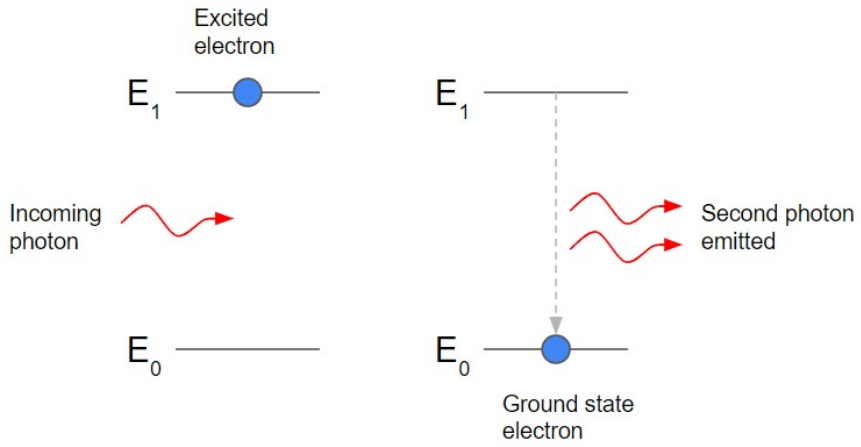

Figure 2.2: Illustration of stimulated emission in a two-level system.

ities may be employed, capped with partially transparent mirrors which enable a continuous output by continually re-amplifying the emitted photons as long as the excited state can be maintained.

This excited state does not occur naturally, however, and must be created by the introduction of additional energy into the atomic system. This is typically done in glass, crystal or doped-glass lasers by using photons from a pump source - be it another laser, concentrated solar light, an intense flashlamp or other source of light. Semiconductor lasers may be pumped by the direct application of electric current, enabling greater efficiency. Semiconductor lasers are often used as pump light sources for other gain media.

2.1.1 Atomic Energy Levels

Due to the quantum nature of atomic systems, electrons may only exist in states with discrete energy, known an energy levels. These are typically visualised with diagrams such as that in Figure 2.2, with energy on the vertical axis and a single spatial dimension on the horizontal axis.

2.1.1.1 Two-level Systems

The simplest possible system is the two-level system, illustrated in Figure 2.2.

In two-level systems, we have only the ground state E_0 and the upper state E_1

separated by a bandgap ΔE_{21}. In optical pumping, the probability of a photon interacting with an electron is characterised by the *effective cross-section* σ of the electronic transition that is to be stimulated. If $N_0(t)$ is the number of electrons that is in the ground state and $N_1(t)$ is the number in the upper state, since their sum must be conserved, we have

$$\frac{dN_1(t)}{dt} = -\frac{dN_0(t)}{dt} \tag{2.1}$$

The rate of population change in a given level must be proportional to the population in that level, and consists of optically stimulated transitions and thermal transitions. If we denote the rate of thermal transition w, and optically stimulated transitions W, with subscripts ij indicating a transition from state i to state j, we have

$$\frac{dN_1(t)}{dt} = -(W_{10} + w_{10})N_1 + (W_{01} + w_{01})N_0 \tag{2.2}$$

Since the rate of stimulated transitions is proportional to the pump power density, in the case of strong optical pumping, W_{01} and W_{10} dominate, simplifying the expression:

$$\frac{dN_1(t)}{dt} = W_{01}N_0 - W_{10}N_1 \tag{2.3}$$

If we define the population difference between the levels $\Delta N(t) = N_1(t) - N_0(t)$, we can take its derivative:

$$\frac{d}{dt}\Delta N(t) = \frac{dN_1(t)}{dt} - \frac{dN_0(t)}{dt} = 2\frac{dN_1}{dt} \tag{2.4}$$

and set this equal to zero to determine the steady-state condition:

$$0 = \frac{dN_1(t)}{dt} = W_{01}N_0 - W_{10}N_1 \tag{2.5}$$

For a given transition, the cross-section (by extension W_{01} and W_{10}) is equal in both directions, and thus the steady state is achieved when $N_0 = N_1$ in the limit of high pump power. This is a problem since the probability of photons to stimulate

emission of another, or be absorbed, is equal, thus no net amplification is possible. Amplification is only possible by achieving a state known as *population inversion*, wherein the number of electrons in the upper state outnumbers those in the lower state, ideally by a large amount to maximise gain.

2.1.1.2 Many-level Systems

Population inversion may be achieved in the simplest way by using a gain medium with an additional upper state to which fast thermal transitions of pumped electrons may occur, illustrated in Figure 2.3. This prevents the equilibrium state that is problematic in the two-level system, as the population in the upper state E_2 is continually quickly decaying into the intermediate state E_1. This means that the laser light produced is of slightly lower energy or longer wavelength than the pump light.

Real gain media often have many multiple intermediate levels (Figure 2.4), broadening the range of photon energies that can be used to pump the medium. Many-level media such as in Figure 2.4 are susceptible to spectral broadening of the output as well, however, necessitating the use of additional components which preferentially allow more amplification for the desired wavelength and dampen all others. This can be achieved by placing the gain medium in a resonant cavity, either tuning the cavity length (Fabry-Perot resonator) to allow repeated passes and amplification in only particular longituinal modes, or by using optical filter components to achieve a similar effect.

2.2 Laser Architectures

Laser system designs may be categorised in different ways, according to the type of gain medium used, the spatio-temporal profile of their output beams, or other parameters. Laser systems may be divided into two broad categories - those with continuous output (*continuous wave* or *CW lasers*), and those with very short pulses,

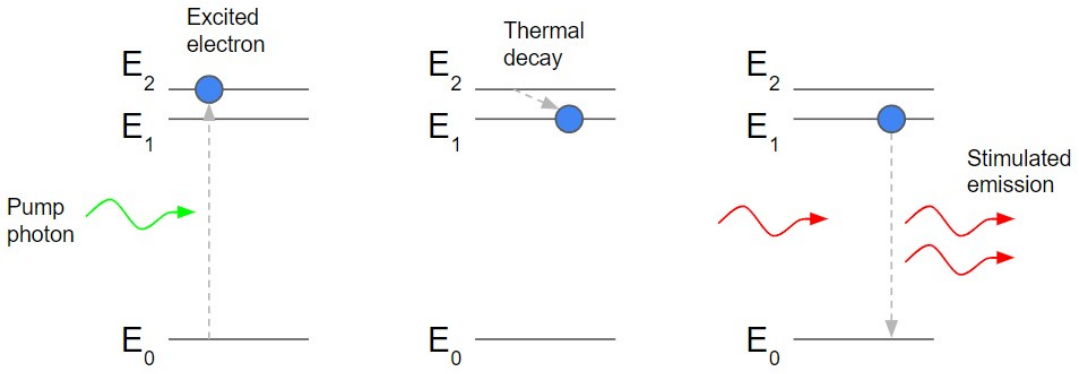

Figure 2.3: Illustration of a three-level system.

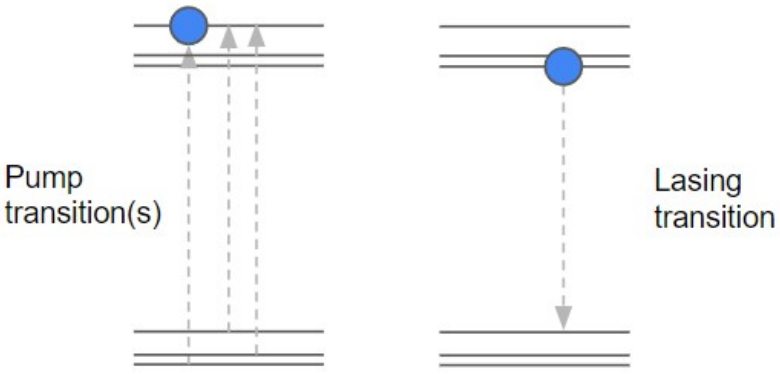

Figure 2.4: Illustration of a many-level system.

2.2.1 Gain Media

Solid-state lasers use, as the name suggests, a gain medium of solid phase - this may be a doped crystalline materials such as the widely used Nd:YAG, Ti-sapphire or ruby lasers, which are optically pumped, or semiconductor lasers, which are pumped by the direct application of electric current. These two types of solid-state laser are often side-pumped, i.e. in a direction perpendicular to the output beam.

Another common form of solid-state laser is the fibre laser - where a glass fibre doped with rare earth elements (ytterbium and erbium being two of the most common dopants) acts as the gain medium and a waveguide, containing the pump and laser light by total internal reflection. Fibre lasers must be pumped longitudinally and thus require filtering of their output to ensure the removal of residual pump light. These offer some significant advantages over bulk crystals - it is easier to achieve a very long optical path length inside the active medium and thus a high gain, since many metres of fibre may be coiled into a small loop and weighs very little. The higher ratio of surface area to volume also assists with heat dissipation in some applications. Fibres may also be made with a thin enough core such that they only permit the transmission of light with wavelength greater than some cutoff wavelength, in the fibre's fundamental mode (Thyagarajan and Ghatak, 2010), which allows better collimation of the output.

Gas and dye lasers use fluid-state gain media, with dye lasers using a liquid suspension or solution rather than a doped crystal or glass.

2.2.2 Continuous Wave Lasers

The simplest design of a CW laser uses a resonating cavity with partially reflective endcap mirrors, as illustrated in Figure 2.5. This can be used for both bulk crystal and fibre lasers, as well as gas or dye lasers. The mirrors may be planar or concave/spherical, and their precise alignment ensures that photons which are not aligned with the cavity axis are quickly lost to the edges, which ensures tight collimation of the output beam.

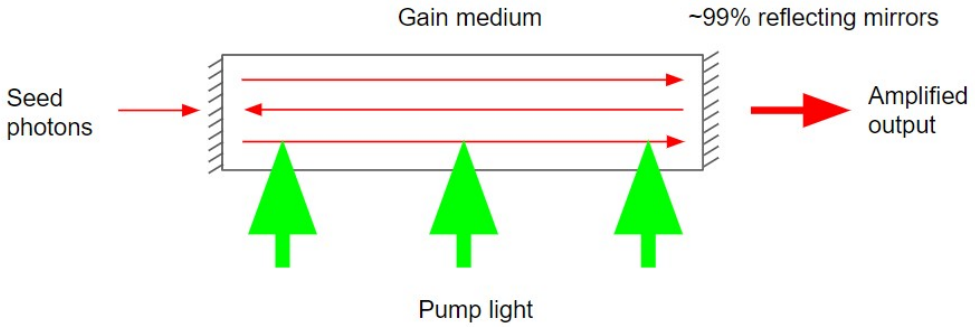

Figure 2.5: Illustration of a CW laser cavity in a bulk gain medium with side-pumping.

2.2.3 Pulsed Lasers

Pulses can be achieved in many different ways. The simplest method to implement is to mechanically modulate the output of a CW laser, by use of for example a fast shutter. However, many of the advantages of pulsed lasers come from the ability to transmit large amounts of optical energy in a short pulse, achieving high fluence. Mechanically modulated CW lasers are limited to a peak power of the CW laser being modulated and are thus less useful than other options.

Semiconductor diode lasers may be electrically modulated, which, similarly to the modulated CW case produces a low-peak-power pulse, with the advantage that the pulses can be made extremely short (ns or shorter). These may be used in combination with amplification stages, to produce short, high-energy pulses.

Q-switched lasers function by adding a variable attenuator (which affects the 'Q factor' of the cavity) inside the cavity, which can be rapidly electrically switched to allow or prevent the positive feedback amplification loop of light inside the resonant cavity. After population inversion has been achieved (the active medium is said to be *saturated*), the attenuation is switched off, allowing amplification to begin which rapidly de-excites all of the ions in the medium, extracting all of the stored energy into one very short, high-energy pulse.

More complex techniques exist for producing ultrashort, high-energy pulses such as chirped pulse amplification, but will not be explained in detail here.

Pulsed and CW lasers are in general used in different applications which can-

not effectively utilise the other operation mode. For example, pulsed lasers enable accurate, macro-scale time-of-flight ranging due to having a consistent temporal profile. Pulsed lasers also enable, on a practical level, ablation or vaporisation of solid-phase materials, due to the extremely high peak fluence achievable. CW lasers on the other hand are better suited for micro- or nano-scale ranging using interferometry (e.g. LIGO (Abbott et al., 2009)), where sufficiently short pulses and high temporal resolution in sensors is not available to enable time of flight implementations. They are also more commonly used in optical cooling and atom traps, where steady illumination is desirable.

Chapter 3

Asteroid Mass Estimation using Laser Ranging

Asteroids are incredibly numerous in our solar system. Of particular interest is an asteroid sub-population known as Near Earth Asteroids (NEAs), which are asteroids whose orbits have close crossings with that of Earth. A further subset of these which have the smallest intersection distances with Earth's orbit have been identified as Potentially Hazardous Asteroids (PHAs), as they pose a collision risk with Earth in the future. Although the majority of asteroids are very small and would likely burn up in the atmosphere before impact, larger and more massive objects are common enough that asteroids do pose at best a non-negligible risk to our civilisation, and at worst an existential threat to all life on Earth. Planetary defence from the threat of NEA impacts is thus an area of active research, given that it is all but inevitable that such an asteroid will one day be discovered which has a significant risk of impact.

Much research has already been done on various methods to perturb the orbits of NEAs. Since the impact threat scales with the mass of the asteroid, and hence its inertia, these techniques generally involve the application of a very slight impulse several years in advance of the potential collision date, thus allowing the perturbation to the orbit to compound over time into a large miss distance.

Several methods to nudge asteroids off of a collision course have been proposed, and a detailed analysis and comparison of some of the most promising

techniques was presented by Thiry and Vasile (2017a). Vasile and Maddock (2010) proposed the use of satellties carrying large mirrors to concentrate light on the surface of an asteroid in order to enhance the Yarkovsky effect - which is a force resulting from the anisotropic emission of thermal radiation from a rotating body illuminated by sunlight. Thiry and Vasile (2017b) modelled in detail the use of a high-power continuous-wave laser to ablate surface material from an S-type asteroid, using the resulting plume of vapour and plasma to generate a small amount of thrust. Kinetic impactors, which impart kinetic energy by intentional collision of a satellite or deployed inert projectile have been studied (Syal et al., 2016; Jutzi and Michel, 2014), indicating viability in their use for asteroid deflection. Other methods include momentum transfer from high-velocity ion beams (Bombardelli and Peláez, 2011), gravity tractors (Lu and Love, 2005), and detonating nuclear explosives in the vicinity of the asteroid (Syal et al., 2013). As of the writing of this thesis, the only technique to have been demonstrated in practice is the kinetic impactor. It is also technologically the simplest to implement, and unlikely to face many political challenges unlike e.g. the use of nuclear weapons to destroy an asteroid. Considering this, the kinetic impactor is likely the technique carrying the lowest development and implementation risk. The work of Thiry and Vasile (2017a) also showed that the kinetic impactor was the most likely to achieve a deflection of 2 Earth radii out of the considered non-nuclear methods, given a maximum notice period of 10 years and launch mass constrained by the Delta IV Heavy's payload capacity. There were some exceptions where laser ablation outperformed, but all considered the kinetic impactor appears to be the most promising technique available.

Obviously, the effect of any intervention method in terms of velocity change is very sensitive to the mass of the asteroid, but also the density or porosity in the case of kinetic impactors, as was shown by Syal et al. (2016). Accurate knowledge of the mass and density of an asteroid prior to attempting any intervention is thus imperative, as the result of the intervention may be quite different if these parameters take different values than was estimated.

Planetary defence, however, is not the only motivation for the exploration

and characterisation of asteroids - they are also of great interest scientifically. Since asteroids are geologically inactive, their materials have remained mostly unchanged for millions of years, providing insight into conditions of the early solar system when the planets were still forming. Exploration of such primordial bodies could give insights into the history of the solar system and possible origins of life. The raw materials present in asteroids (metals for construction and water for survival and propellant production, both available outside of a deep gravity well) is also of great interest for future space industry and a serious motivation for NEA exploration. Since asteroids have an extremely low escape velocity, it may in the future be cheaper to source raw materials for space industry and construction from NEAs rather than from the surface of Earth or the Moon.

There have been numerous missions to explore asteroids and other minor bodies in the past, both flybys and orbiters. Several flyby missions were performed en route to some other primary target, either another asteroid or a planetary body. A list of these missions and the number of visited targets can be found in Table 3.1.

Mission	# Targets	Flyby Distance
NEAR Shoemaker	2	1212 km, orbit
Galileo	2	1604, 2110 km
Deep Space 1	1	28 km
Stardust	1	3079 km
Hayabusa	1	Orbiter
Rosetta	3	800 km, 3162 km, orbit
Dawn	2	Both orbited
Chang'e 2	1	3.2 km
Hayabusa2	1	Orbiter
ORISIS-REx	1	Orbiter
Lucy	7	TBD
Psyche*	1	Orbiter
DESTINY*	1	TBD
ZhengHe*	1	TBD

Table 3.1: List of missions that have achieved - or plan to perform - flybys or orbits of minor bodies in the inner solar system and main belt. * denotes future missions.

These missions returned valuable scientific data on properties of the visited asteroid such as size, structure and composition, with Hayabusa2 and OSIRIs-

REx collecting samples for return to Earth.

The masses of asteroids have been estimated by measuring the perturbations of other objects' trajectories due to the gravity of the asteroid in question. NEAR Shoemaker, en route to Eros, flew by its secondary target 253 Mathilde, enabling estimation of its mass by analysis of the Doppler shift of communications signals before and after the flyby to determine the change in the spacecraft's line-of-sight velocity with Earth.. The mass of 253 Mathilde was measured at 1.03 x10^{20} kg with 1σ error 4x10^{18} kg, or 3.88% (Yeomans et al., 1997). A similar technique was employed by the Rosetta spacecraft to determine the mass of 21 Lutetia, which was estimated to be 1.7x10^{18} kg.

All of these mass estimations have 1-σ uncertainties on the order of 5-10% of the actual mass, with the exception of Rosetta's measurement of Lutetia's mass which has an uncertainty of approximately 1%. Additionally, most have rather large masses, on the order $> 10^{18}$ kg. The lightest asteroid whose mass has been measured in the literature is 433 Eros, which has a mass of 6.7 x10^{15} kg (Yeomans et al., 2000), measured from orbit by the NEAR Shoemaker spacecraft. This forms a benchmark of the performance of current techniques.

This Chapter will present a new technique for estimating the mass of asteroids using laser ranging in a dual flyby scenario. The technique was first proposed by the author in the context of the NEOCORE mission concept (Walker et al., 2021), which will be reviewed in this Chapter. A sensor model will be constructed which allows the performance of the laser rangefinders to be estimated, before constructing a dynamic model of the dual flyby and using the estimated rangefinder performance to determine the mass of a hypothetical asteroid from simulated data. The performance of the new technique will be shown to exceed that of the aforementioned techniques such as Doppler measurements in terms of the minimum mass that may be measured, and the accuracy to which equivalent masses may be measured far exceeds that of previously performed experiments.

3.1 Mass Estimation Experiment

The mass of a celestial body can be estimated by observing the movement of nearby objects under the influence of the gravitational field of the main body. This is relatively easy for large bodies such as planets, with large, bright natural satellites that can be observed from Earth - the gravitational parameter GM (the product of the gravitational constant G and the object's mass M, typically denoted by μ) of the central body of a system can be estimated from observations of the orbits of these satellites. However, for smaller bodies such as asteroids or moons this becomes more difficult, as they often do not have any natural satellites. Additionally, less massive bodies are often irregularly shaped, leading to more complex orbits due to higher-order harmonic effects in the gravitational field, and so simple observations of the orbital period may not be sufficient to estimate the mass.

Masses of celestial bodies have previously been estimated from gravitational interactions with spacecraft, by monitoring the spacecraft trajectory relative to Earth using the time of flight of radio signals. For example, the Voyager 2 probe used this method to estimate the masses of the Uranus system and some bodies in the Saturn system (Tyler et al., 1986, 1982). The bodies probed by this method in the past were much more massive than the kilometre and sub-kilometre scale asteroids which are of interest in the context of planetary defence - for example, the mass of Mimas is of the order 10^{19} kg, compared with 10^{12} kg for a 1 km diameter spherical asteroid with the density of olivine. For a 100 m diameter asteroid, the mass is of the order 10^{9} kg. For these smaller targets, it is still technically possible to estimate the mass via gravitational deflection of spacecraft trajectory, however modifications to the mission architecture and instrumentation must be made if this is a primary objective.

If a mission were to employ two spacecraft flying in formation, their trajectories relative to one another may be able to be tracked to a greater degree of accuracy than could be achieved with Earth-based observations of a single satellite's trajectory. Additionally, by choosing an appropriate flyby configuration -

for example, by having the two spacecraft fly by on opposing sides of the asteroid as illustrated in Figure 3.1 - the effect of the asteroid's gravity on their relative trajectories could be stronger than the effect on their individual Earth-relative trajectories.

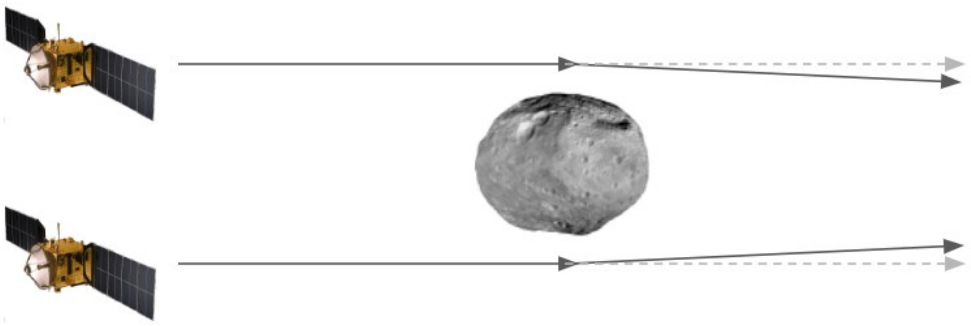

Figure 3.1: Illustration of the proposed opposing dual flyby configuration.

A laser rangefinder (LRF) is one device which can be used to precisely measure the distance to an object, given high enough timing resolution and ideal target surface profile. In their most simple form, an LRF operates by transmitting a short pulse of laser light, which scatters off the target object, and the backscattered light is detected. The time difference between the transmitted pulse and received backscatter peak are used to determine the distance to the object. Often a small portion of the transmitted pulse is siphoned onto the detector to accurately determine the pulse launch time and hence the time of flight. The use of laser-based metrology lends itself well to measuring kilometer scale distances in space due to the lack of atmospheric absorption, meaning little light is absorbed travelling to and from the target object.

Despite the lack of atmospheric scattering, simple backscatter detection ranging still suffers large amounts of light loss, which is important when dealing with space-based instruments as weaker signals will require larger, heavier light-collection optics to detect. Firstly, if the target does not have an albedo close to 1 (asteroids are typically in the range of 0.1-0.2), much light is lost in absorption by the target. Secondly, for diffusely reflecting targets, yet more light is lost by being reflected at angles that result in it not being collected by the receiver. This effect compounds over larger distances, as the total amount of reflected light is

effectively spread over a hemisphere of ever-increasing size. In some applications this can be countered by attaching a retroreflector array to the target object, which directs incoming light back in the same direction it originated from. Five such retroreflectors were left on the Moon during the lunar exploration campaigns of the 60s and 70s and are still used to this day in laser ranging experiments to monitor the distance to the Moon to millimetre-level accuracy (Müller et al., 2019). This not only increases the strength of the detected reflected pulse, but also reduces the impact of target shape effects on the temporal pulse profile if the retroreflector is flat. A large retroreflector, however, if not aligned closely with the beam propagation axis can result in pulse stretching and introduce additional uncertainty to range measurements. Light loss could also be ameliorated by the use of higher pulse energies, so that the small fraction of light collected by the receiver is large enough to be detected. However, similarly to increased aperture size, this will increase the size, mass and power consumption of the laser system, which should be avoided if possible.

Another disadvantage which is inherent to backscatter ranging and cannot be overcome even with larger receiver apertures, is temporal pulse distortion. If the target object is anything other than a perfect plane orthogonal to the beam axis, target shape effects will result in broadening and distortion of the return pulse, making it more difficult to obtain extremely accurate distance measurements, as is required for highly precise ranging. For cases where the local surface does not vary significantly over the laser spot, this is not an issue, however due to beam divergence at kilometer scale distances, a tightly focused spot at the target would be neither possible nor desirable, as this vastly increases the pointing accuracy requirement. If the beam spot is much larger than the target, pointing requirements are reduced.

An alternative mode of operation for laser ranging is what is known as two-way ranging (TWR). TWR employs the use of two transmission and recieving stations, A and B. A transmits a pulse, which is received by B's detector. This triggers a response pulse from B back in the direction of A. If the timing of B's detection and response circuitry can be characterised by a response time $t_{response}$

with known mean and standard deviation, the net pulse time of flight can be recovered and thus the distance between the stations measured. To compare the two techniques, let E_c be the total pulse energy collected by satellite A, E_e be the emitted pulse energy for A or B, α_B the albedo of satellite B, and $A_b(z)$ the beam area at distance z from the emitter. Assuming isotropic scattering of the laser light over a hemisphere, and assuming that the target object is smaller than the beam area to allow for pointing inaccuracies, for the backscatter case the collected pulse energy is

$$(E_c)_{BS} = E_e \frac{A_T}{A_b(z)} \frac{\eta_{col} A_{col}}{2\pi z^2} \alpha_B \tag{3.1}$$

where A_{col} and η_{col} are respectively the collector aperture area and the total photon collection efficiency of the collection optics. Similarly, for the TWR configuration (again, assuming large distance such that the receiver is smaller than the beam radius):

$$(E_c)_{TWR} = E_e \frac{\eta_{col} A_{col}}{A_b(z)} \tag{3.2}$$

.

From here, the increase in returned power from using TWR over backscatter can be expressed as

$$\frac{(E_c)_{TWR}}{(E_c)_{BS}} = \frac{2\pi z^2}{A_T \alpha_B} \tag{3.3}$$

which is proportional to z^2. Thus at large distances, the TWR configuration vastly increases the strength of the signal arriving at A. This improvement in received signal strength is visualised in Figure 3.2 for kilometre scale distances with $A_T = 0.06$ m^2, the area of the largest face of a 12U CubeSat, and $\alpha_B = 0.5$. As can be seen, at only a couple of kilometres, the collected pulse energy is more than nine orders of magnitude higher than the backscatter mode of operation, thus allowing significantly less sensitive optical sensors, smaller collection optics, a significantly less powerful laser and the subsequent mass and power saving.

The TWR configuration should also be compared with a one-way setup util-

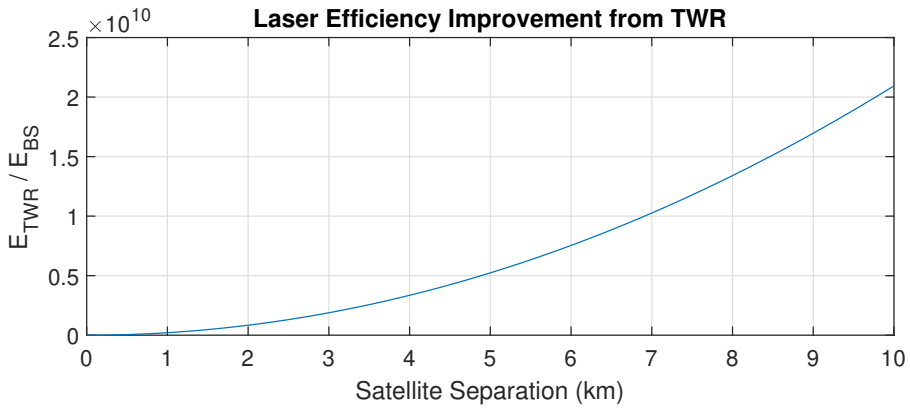

Figure 3.2: Ratio of returned optical power density using TWR with that of using backscattered light, over increasing distances.

ising a retroreflector. Similarly to Equations 3.1-3.2, the collected pulse energy in the retroreflector case is

$$(E_c)_{RR} = E_e \frac{A_{RR}}{A_b(z)} \frac{A_{col}}{A_b(z)} \eta_{col} \tag{3.4}$$

where the first quotient term is the fraction of total pulse energy incident on the reflector array, and the second quotient term is the fraction of retroreflected light (which has the same divergence as the incoming pulse) that subsequently is collected by the collector at satellite A. Here a perfect retroreflector is assumed with zero absorption and perfect ray redirection.

Thus, the performance of TWR compared with a retroreflector array can be expressed as

$$\frac{(E_c)_{TWR}}{(E_c)_{RR}} = \frac{A_b z}{A_{RR}} \tag{3.5}$$

.

The equation for the beam divergence (3.7) is included in Section 3.1.1 and is also quadratic in z. The improvement for TWR over retroreflection can be seen in Figure 3.3, for a 2cm emitter and a Gaussian beam with quality factor $M^2 = 1.3$, as well as a retroreflector array covering 1U, or 0.01 m^2.

It can be seen that, again, TWR performs better, but only by 1-2 orders of magnitude in the range of distances applicable to a close flyby (<20 km). Thus a

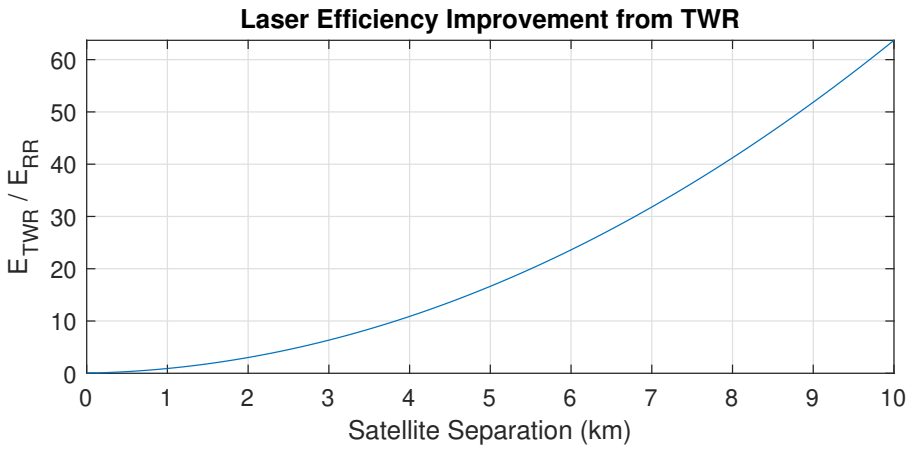

Figure 3.3: TWR signal strength improvement over retroreflector-based ranging at a range of distances.

retroreflector array may be a viable alternative, particularly as a backup should one of the lasers fail. However, due to the significantly improved performance without the need for an additional spacecraft component, TWR was chosen as the primary method of obtaining the inter-satellite range (ISR) data for this mission.

3.1.1 Two-Way Ranging Model

In order to determine the performance of the mass estimation experiment, the performance of the instruments must first be known. Since TWR has thus far had limited terrestrial application, there is no readily available space-proven commercial instrumentation with specifications which can be simply read. Thus, a model of the entire sensor signal chain was developed to assess potential performance and will be presented in this Section.

3.1.1.1 Signal Photon Rate

The detector being modelled is a single-photon avalanche photodiode (APD) array - a sensitive semiconductor light sensor consisting of a set of pixels which convert incoming photons to electron-hole pairs. In the case of single-photon sensors, the bias voltage is increased beyond the breakdown voltage, and thus a single ionisation event (i.e. an incoming photon, but thermal noise may also

trigger an ionisation) will create a self-sustaining ionisation cascade which creates a conduction channel between the p- and n-type regions and their electrodes. Since the bias voltage is so high that the cascade is self-sustaining, this conduction channel remains open (i.e. the pixel is triggered) until the bias is removed, resetting the pixel.

The first step in modelling the TWR system is to determine the primary electron generation rate in the sensor as a function of time. Let the arbitrary temporal profile of a laser pulse leaving the transmitter be $P_e(t)$. At some location z along the beam propagation axis, the incident power density at the collector on satellite B is thus

$$\Phi_c(z,t) = \frac{P(t - \frac{z}{c})}{A_b(z)} \tag{3.6}$$

where $A_b(z)$ is the beam radius at distance z from the emitter. For a Gaussian beam with the beam waist located at the emitter ($z = 0$), the $1/e^2$ radius can be approximated by

$$A_b(z) = \pi(w_0 + z\tan(\theta_{div}))^2 \tag{3.7}$$

where w_0 is the beam waist radius, and θ_{div} is the divergence half-angle of the beam.

At this point, the equations diverge from those of the simple backscatter LIDAR. Since a new pulse is transmitted by B (of the same wavelength and profile), triggered by the reciept of the pulse from A, the returned signal is not some transformation of the transmitted pulse, but a new pulse entirely. Thus, there is no need to divide again by A_b^2, and no consideration of the albedo of satellite B is required. Accounting for the round-trip distance, Equation 3.6 becomes

$$P_c(t) = \frac{P(t - \frac{2z}{c} - t_{response})}{A_b(z)} \tag{3.8}$$

where $t_{response}$ is a small time delay which models the time required to receive and process the incoming pulse, and trigger a response. $t_{response}$ is modelled as a

normally distributed time offset, with standard deviation t_{jitter}. Thus the total power delivered to the detector per pixel is

$$P_c(t) = \frac{1}{2n_{px}} A_{col}\eta_{col} \frac{P(t - \frac{2z}{c} - t_{response})}{A_b(z)} \tag{3.9}$$

where n_{px} is the number of pixels in the array, and A_{col} and η_{col} are respectively the collecting area of the aperture and the overall optical efficiency of the system. Here a factor of 1/2 is added to avoid sensor dead time and ensure continual observation. The only source of uncertainty to be concerned with in Equation 3.9 is the jitter in response time, as uncertainties in, for example, optical efficiency will not result in a temporal shift of the detected pulse. In APD or SPAD arrays, generally pixels are not reset on an individual basis after triggering, rather the entire array is reset simultaneously. This results in appreciable dead time between successive range gates which is typically on the order of tens of milliseconds. Since the distance to the target is not known precisely in advance and is variable, sensor resets cannot be strategically timed. Since shorter pulses allow for more precise return timing, the pulse length would likely be on the order of a few nanoseconds, so it is possible that some returning pulses could be missed if they arrive during a sensor reset period. To circumvent this, the signal could be split evenly between two sub-arrays, with offset range gates, to ensure net zero dead time is achieved and no pulses are missed.

It follows then, that the primary signal electron generation rate per pixel $R_{PSE}(t)$ can be obtained by simply dividing by the average photon energy at wavelength λ, multiplying by the detector quantum efficiency η_q, and the SPAD array fill factor F_f. This fill factor is the 'spatial efficiency' of the sensor array - the fraction of total array area which is either photosensitive or filled with microlenses, resulting in incident photons impinging on photosensitive components.

$$R_{PSE}(t) = \frac{1}{2} \frac{F_f \eta_q \lambda A_{col} \eta_{col}}{hcn_{px}} \frac{P(t - \frac{2z}{c} - t_{response} - t_{jitter})}{A_b(z)} \tag{3.10}$$

Here t_{jitter} is subtracted as it is a random variable which takes a new value, positive or negative, for each pulse. Adding additional terms for noise photons

R_{NPE} and dark counts R_D (which are assumed to be constant and will be discussed in Section 3.1.2), the total primary electron (i.e. electrons which begin an ionisation cascade and result in a pixel trigger) generation rate per pixel is

$$R(t) = R_{PSE}(t) + R_{NPE} + R_D \tag{3.11}$$

3.1.1.2 Sensor Model

Since photon counting is a probabilistic process following Poisson statistics, the probability of detecting k photons in a given time window t_b, given an average photon rate $R(t)$ is given by

$$P(k) = \frac{K^k}{k!}e^{-K} \tag{3.12}$$

(Luo et al., 2015a) where $K = R(t)t_b$ is the average number of photons expected in the time window. Now consider an array of SPAD pixels which are sampled at a rate of $1/t_b$. To generate a synthetic SPAD output, a time series of triggers per time bin, each pixel may be simulated individually over the course of the time bins in a single range gate.

Setting k = 0 in Equation 3.12 gives the probability for a given pixel to *not* be triggered in the time bin corresponding to time t, which we shall call P_{NT}. Thus, setting $k = 0$ the probability of an individual pixel triggering in a single range gate, $P_T = 1 - P_{NT}$, is

$$P_T = (1 - e^{-R(t)t_b})T \tag{3.13}$$

where T is a binary number which takes the value 0 if the pixel has previously been triggered, and 1 if it has not. Using Equations 3.11 and 3.13 along with a uniform random number generator one can generate time series data for each of the n_{px} pixels in the array, and sum these together to obtain the simulated SPAD output. An example of a range gate containing the spike from the returning pulse can be seen in Fig. 3.4. The range measurement is extracted by smoothing the histogram and fitting a Gaussian curve.

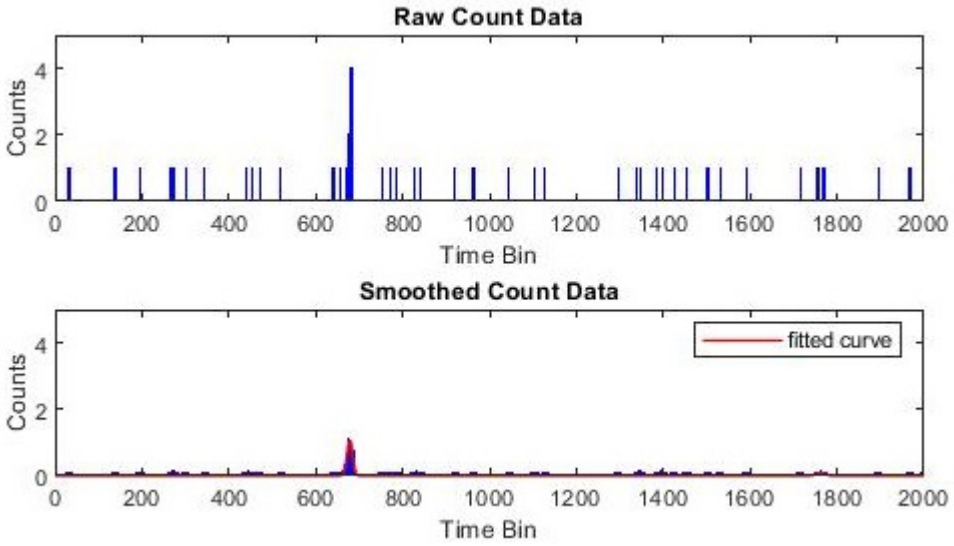

Figure 3.4: Simulated measurement of a single range gate with fitted Gaussian curve.

This completes the model of the two-way ranging system. This can now be used to estimate the standard deviation of range measurements that are likely to be possible using such an instrument. This is done by simulating 500 pulses at a fixed distance with the instrument parameters in Table 3.2, and noise counts as will be discussed in Section 3.1.2. The values in Table 3.2 are somewhat arbitrary as no real system exists, but chosen values are within the bounds of what is reasonable to expect currently or in the near future: sub-ns pulse widths are not uncommon in modern laser systems, SPAD arrays with 1024 pixels have been produced in recent years (Conca et al., 2019), and commercial photodiodes and laser diode drivers are readily available with rise times less than 10 ps and pulse stability on the order of picoseconds. The results of this can be seen in Figure 3.5, showing a standard deviation of range measurements of 1.13 mm. This value will be used when generating TWR measurements in the simulation of the gravimetry experiment.

3.1.2 Noise Sources

Two primary sources of noise were included in the sensor model - dark counts and solar photons. Dark counts arise from spontaneous pair production in even

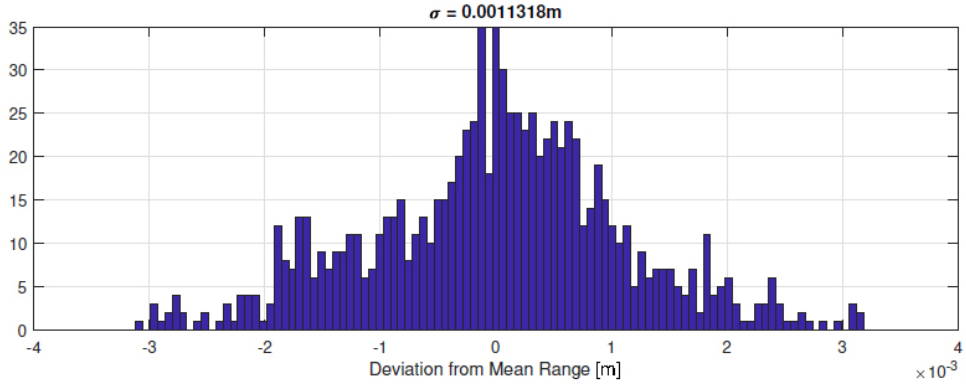

Figure 3.5: Distribution of simulated range measurements for static-target ISR measurements.

Parameter	Value/unit
σ_{jitter}	5 ps
t_{pulse}	100 ps
n_{px}	1024
t_b	10 ps

Table 3.2: Parameters used in TWR model.

an unilluminated photodiode due to thermal effects, thus their effect is reduced when active cooling of the sensor is available. Dark count rate (DCR) in InGaAs SPADs of 1 kHz per pixel has been shown to be possible (Itzler et al., 2011). The same paper also demonstrated a high dependency of DCR on sensor temperature. To assume a pessimistic case with poor cooling, a DCR of 50kHz per pixel was chosen for the modelling of TWR performance.

Background signal-wavelength photons from the Sun were also included in the noise terms. This is modelled as having a spectral irradiance equal to that of sunlight at the signal wavelength of 1064 nm and at a distance of 1 AU from the Sun, which is 0.647 $\mathrm{Wm^{-2}nm^{-1}}$ (Sun et al., 2006). A bandpass filter of width 5 nm centered on the signal wavelength was assumed. The worst case scenario for sunlight noise was modelled, with the collector being exposed to normally incident sunlight, although in reality it is likely that there would be some form of sun-blocking baffle which would reduce the solar photon rate to much lower levels. Solar photons reflected from the target object at a phase angle of 90 degrees (i.e. the object is illuminated from the side, from the point of view of the sensor) and

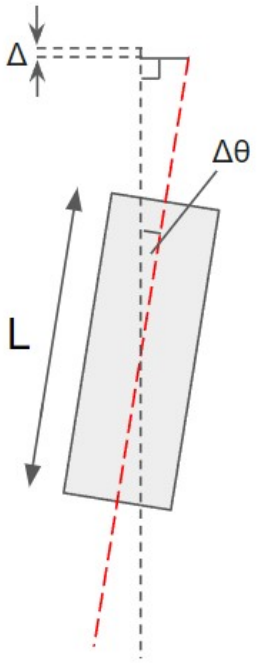

Figure 3.6: Illustration of the effect of pointing misalignment. Sensor plane is offset by the small distance Δ.

impinging on the collector were also accounted for.

3.1.2.1 Effect of Pointing Errors on Range Measurement

An additional error may arise from slight misalignment of the pointing axes of the spacecraft, as illustrated in Figure 3.6. This is likely to be a small oscillation around the desired pointing direction. Here the round-trip distance is made slightly longer by the amount Δ due to this misalignment. Here L is the length of the spacecraft along the axis parallel with the beam/camera axis, and $\Delta\theta$ is the 1-σ pointing error.

From this, it can be seen that the additional error in the ISR measurements can be written as

$$\Delta = \frac{L}{2}(1 - \cos\Delta\theta) \tag{3.14}$$

.

Current state of the art CubeSat ACDS systems are available with attitude determination accuracies of $< 0.5^o$ (Guo and Han, 2016), with the best performing

options boasting 1-σ accuracies of $\pm 0.007^o$ (Guo and Han, 2016; Blue Canyon Technologies). For a 12U CubeSat with $L = 30$ cm, accounting for both satellites' pointing uncertainties the more pessimistic of these would lead to a total 1-σ range uncertainty of ± 5.71 μm, and the best case giving ± 1.12 nm. Even the worst case of these is three orders of magnitude smaller than the errors present from the pulse centroid detection method, so this error source is neglected in this model.

3.2 Experiment Simulation

In this section, performance metrics for the TWR system obtained in previous sections will be used with simulations of the dual flyby to estimate the lower limit of this mass estimation technique given a particular set of flyby conditions.

3.2.1 Dynamic and Measurement Models

A physical model describing the gravitational interactions between the Sun, the asteroid and the satellite must now be constructed, which will be used to propagate state vectors, generate simulated TWR data, and estimate the mass of the asteroid.

The dynamics are described using the standard inertial heliocentric Cartesian coordinate system, with the x-y plane on the ecliptic and the x axis aligned with the direction of the vernal equinox. Time is defined such that $t = 0$ is the instant that the asteroid crosses the ecliptic plane.

The state of the two spacecraft system is described using a single state vector:

$$\mathbf{X}(t) = \begin{bmatrix} \mathbf{x}_1(t) \\ \dot{\mathbf{x}}_1(t) \\ \mathbf{x}_2(t) \\ \dot{\mathbf{x}}_2(t) \end{bmatrix} \tag{3.15}$$

where $\mathbf{x}_1$, $\mathbf{x}_2$ are the position vectors of spacecraft 1 and 2, and $\dot{\mathbf{x}}_1$, $\dot{\mathbf{x}}_2$ are their respective velocity vectors.

The rate of change of the state vector $\dot{\mathbf{X}}(t)$ is described by

$$\dot{\mathbf{X}}(t) = \begin{bmatrix} \dot{\mathbf{x}}_1(t) \\ -\mu_{sun}\frac{\mathbf{x}_1(t)}{\|\mathbf{x}_1(t)\|^3} - \mu_{ast}\frac{(\mathbf{x}_1(t)-\mathbf{p}_{ast}(t))}{\|\mathbf{x}_1(t)-\mathbf{p}_{ast}(t)\|^3} \\ \dot{\mathbf{x}}_2(t) \\ -\mu_{sun}\frac{\mathbf{x}_2(t)}{\|\mathbf{x}_2(t)\|^3} - \mu_{ast}\frac{(\mathbf{x}_2(t)-\mathbf{p}_{ast}(t))}{\|\mathbf{x}_2(t)-\mathbf{p}_{ast}(t)\|^3} \end{bmatrix} \tag{3.16}$$

where $\mu_{sun} = GM_{sun}$ and $\mu_{ast} = GM_{ast}$ are the gravitational parameters of the Sun and the asteroid respectively. Here the acceleration terms are derived from Newton's law of gravitation, accounting for the gravitational acceleration towards both the Sun and the asteroid. A more complete model would include expressions for the gravity of Ceres, Jupiter and other planetary bodies, but these small perturbations are ignored in this formulation of the dynamic model as the satellites will be only a few kilometres apart and hence planetary bodies several astronomical units away will not cause a significant enough differential gravitational force to impact the measurement. $\mathbf{p}_{ast}(t)$ is obtained from prior propagation of the asteroid's state $\mathbf{X}_{ast}(t)$, according to a similar dynamic model which only accounts for the position of the asteroid and the gravity of the Sun. The state vector describing the state of the asteroid is

$$\mathbf{X}_{ast}(t) = \begin{bmatrix} \mathbf{p}_{ast}(t) \\ \dot{\mathbf{p}}_{ast}(t) \end{bmatrix} \tag{3.17}$$

and its derivative is

$$\dot{\mathbf{x}}_{ast}(t) = \begin{bmatrix} \dot{\mathbf{p}}_{ast}(t) \\ -\mu_{sun}\frac{\mathbf{p}_{ast}(t)}{\|\mathbf{p}_{ast}(t)\|^3} \end{bmatrix} \tag{3.18}$$

.

This allows the state of the asteroid to be propagated in advance of the spacecraft state propagation, and the resulting states used in Equations 3.15-3.16. States are propagated using the MATLAB ode45 solver.

In order to propagate the spacecraft dynamics however, a value of μ_{ast} (i.e. the mass of the asteroid m_{ast}) must be supplied. In a real mission scenario, the mass would be estimated by performing least squares regression analysis on m_{ast}

with respect to some set of real-world measurements from the two-way LIDAR. These true measurements however must here be substituted with a simulated set of measurements for the proof of concept. By propagating the dynamics with $m_{ast} = m_{true}$, the 'true' mass of some hypothetical asteroid, and employing a measurement function $g(t)$ which acts on the state vector at time t and returns a simulated range measurement for that instant, this simulated set of measurements may be generated. After the generation of measurements, m_{true} is considered to be unknown, and the objective is to recover its value from the simulated set of measurements. The measurement function $g(t)$ returns only the scalar range between the two satellites:

$$g(\mathbf{X}(t)) = h(\mathbf{X}(t)) + \mathcal{N}(0, \sigma_{noise}) \tag{3.19}$$

where $\mathcal{N}(0, \sigma_{noise})$ is a random Gaussian noise term with standard deviation $\sigma_{noise} = 1.13\text{x}10^{-3}$ m, from previous sections. No systematic error is included here as these can be accounted for and effects removed by proper instrument calibration before launch. Although there is the possibility of system degradation introducing a small systematic error over the course of a long mission duration, such effects are not studied in detail here. $h(\mathbf{X}(t))$ extracts the noise-free distance between the satellites at time t:

$$h(\mathbf{X}(t)) = \sqrt{(\mathbf{x}_1(t) - \mathbf{x}_2(t)) \cdot (\mathbf{x}_1(t) - \mathbf{x}_2(t))} \tag{3.20}$$

.

We can now construct a vector containing the set of simulated measurements which we shall call $\mathbf{z}$:

$$\mathbf{z} = \begin{bmatrix} g(\mathbf{X}(t_0)) \\ g(\mathbf{X}(t_1)) \\ g(\mathbf{X}(t_2)) \\ \vdots \end{bmatrix} \tag{3.21}$$

3.2.1.1 Initial Conditions

The measurement phase of the flyby begins at $t = -86400$ s, or one day before the flyby. Initial conditions are found by first arranging the satellites with respect to the asteroid to the desired flyby configuration at $t = 0$, and then propagating both spacecraft back in time to the beginning of the measurement phase using the true mass value. Since this thesis is focussed on the mass estimation experiment, this approach was chosen to ensure particular flyby configurations may be achieved without consideration of the GNC chain. In real deployment however, the incoming trajectories may be different given the prior uncertainty on the asteroid's position before orbit determination is completed. Although the spacecraft orbits may not be circular, for simplicity the spacecraft are initialised in circular orbits with zero inclination, perfectly coincident with the position of the asteroid at $t = 0$. From here, small position adjustments are made to achieve the desired flyby configuration. Different configurations will be discussed later, but the first configuration considered consists of the two spacecraft being equidistant from the asteroid at the moment of flyby, one 2 km closer to the Sun and one 2 km further from the Sun - i.e. the asteroid passes perfectly between the two spacecraft.

The asteroid target chosen for these simulations was the real asteroid 2015 MQ116, which is one of the targets in the NEOCORE reference tour (Walker et al., 2021). The orbital elements for the asteroid when at its ascending node can be found in Table 3.3.

a (AU)	e	i (^{o})	Ω (^{o})	ω (^{o})	ν (^{o})
1.0906	0.1814	14.8014	281.63	258.79	101.21

Table 3.3: Keplerian elements of asteroid 2015 MQ116.

The resulting state at $t = -86400$ s was taken as the initial state. To simulate the trajectories taken by the two spacecraft, this is propagated using the dynamic model with some test value for m_{ast} until 5 days after the flyby, for a total measurement period of 6 days. A time-asymmetric observation period is chosen to allow for trajectory correction maneuvers to continue until very close to the flyby,

and also because the most significant deflection from the unperturbed trajectory will occur after the flyby. The propagation was performed using an adaptive timestep limited to 500 s (when close to the asteroid, the timestep dramatically reduces). TWR measurements were assumed to be taken at a rate of 0.1 Hz, and so intermediate states corresponding to the time of each range sample were interpolated from the propagator output. These are used as inputs to the noise-free measurement function $h(t)$ to return the set of expected measurements $\mathbf{y}$. This definition is effectively reused in the calculation of $\mathbf{z}$ (Equation 3.21) by adding sensor noise onto the ideal measurement set to obtain the simulated, noisy measurement set. Since $\mathbf{y}$ will contain different values depending on which value of m_{ast} is used to propagate the state, it is denoted $\mathbf{y}(m_{ast})$:

$$\mathbf{y}(m_{ast}) = \begin{bmatrix} h(t_0) \\ h(t_1) \\ h(t_2) \\ \vdots \end{bmatrix} \tag{3.22}$$

It should be noted that in reality there may not be strictly continuous measurement throughout the entire 6 day period, as during the flyby the spacecraft will be required to change orientation to allow optical observations of the asteroid before resuming TWR measurements. However, this is ignored as it does not change the subsequent method to extract the mass.

The ISR measurements over the measurement period for two different asteroid masses are shown in Figure 3.7, showing the difference in the relative trajectory that is seen by changing the mass of the asteroid.

3.2.2 Mass Estimation

In order to determine the mass of the asteroid from TWR data, one must find the value for m_{ast} in the dynamic model that best explains the data set gathered during the flyby. This can be done by least-squares minimisation between the model and observations. We define a cost function $\epsilon(m_{ast})$ which must be minimised to find the estimated mass m_e:

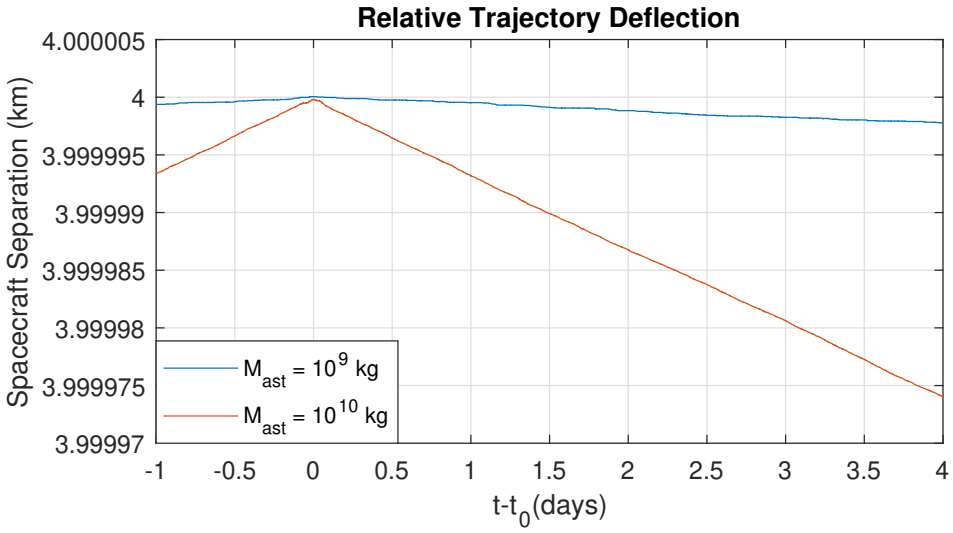

Figure 3.7: Noise-free ISR curves in the case of 10^9 kg and 10^{10} kg asteroids.

$$\epsilon(m_{ast}) = \sum_{i=1}^{N} (\mathbf{z}_i - \mathbf{y}_i(m_{ast}))^2 \tag{3.23}$$

$$m_e = \min_{m_{ast}} \epsilon(m_{ast}) \tag{3.24}$$

where the subscript i denotes the i-th elements in the vectors $\mathbf{z}$ and $\mathbf{y}(m_{ast})$, N is the number of TWR samples obtained over the measurement period.

A gradient descent algorithm may not reliably converge to the global minimum since calculating the required gradients about m_{ast} is unreliable due to noise, as well as time-consuming. Instead, a simple grid search was performed with respect to m_{ast}. This was done in two steps, first obtaining a coarse estimate across many orders of magnitude, then using finer steps to obtain a more precise estimate. It was found that when the mass is not close to the lower limit of this technique, the m_{ast} - ϵ curve generally took a similar shape, with the trough about m_{true} becoming shallower and wider as m_{true} decreases. The typical shapes of coarse and refined search results can be seen in Figures 3.8 - 3.9.

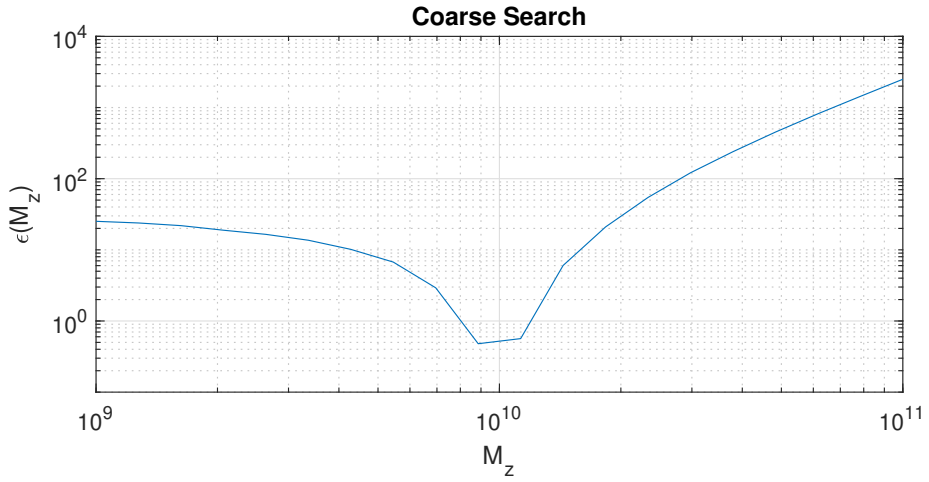

Figure 3.8: Typical coarse search curve on m_{ast} ($m_{true} = 10^{10}$ kg).

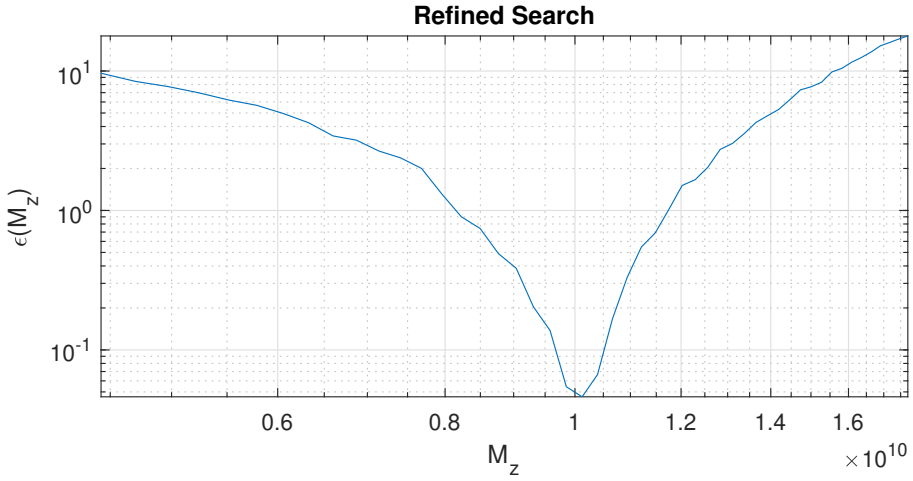

Figure 3.9: Typical refined search curve on m_{ast} ($m_{true} = 10^{10}$ kg).

When plotted on a linear scale, these can be very well-fit with a quadratic curve, whose turning point's location is taken as the estimated mass measurement. This is shown in Figure 3.10, again for a true mass $m_{ast} = 10^{10}$ kg.

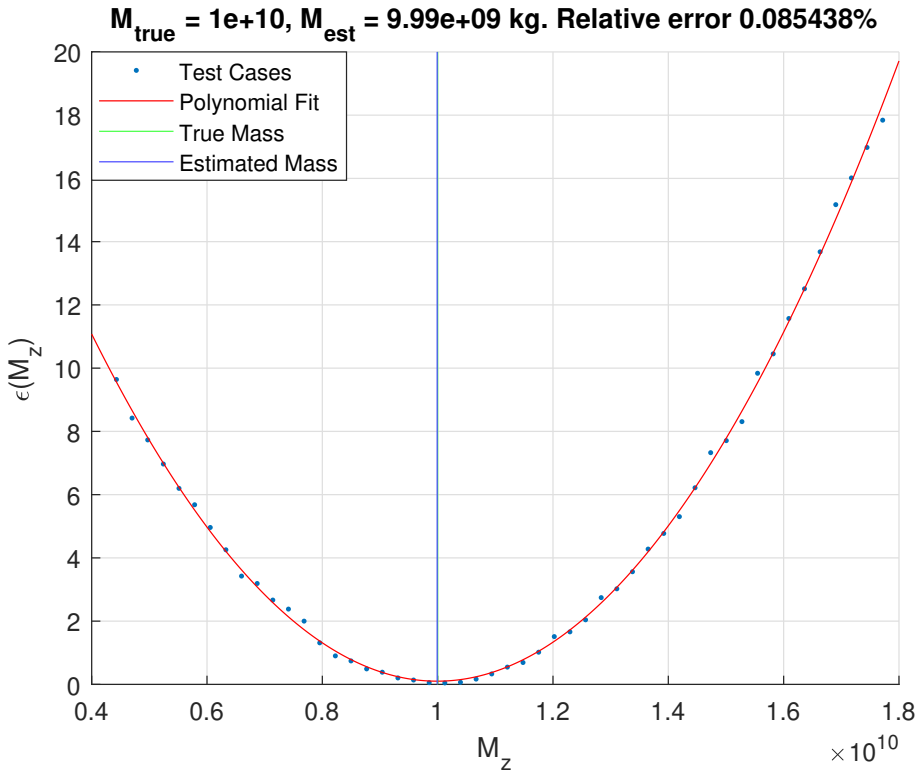

Figure 3.10: Refined search on linear scale. Local quadratic fit applied and derivative used to obtain M_{est}.

3.3 Lower Mass Limit

When the mass of the asteroid is not close to the limits of the technique, such as the 10^{10} kg asteroid in Figures 3.8-3.10, this method yields very good estimates of m_{true}. However, as the mass becomes smaller, the dip in the $\epsilon(M_z)$ curve becomes shallower and wider, and the quadratic approximation begins to break down. This can be seen clearly in Figures 3.11-3.12, which is the result for a 10^7 kg asteroid with the same encounter distance (2 km) and trajectory. Here the asteroid is so light that no discernible dip can be seen in the cost function curve.

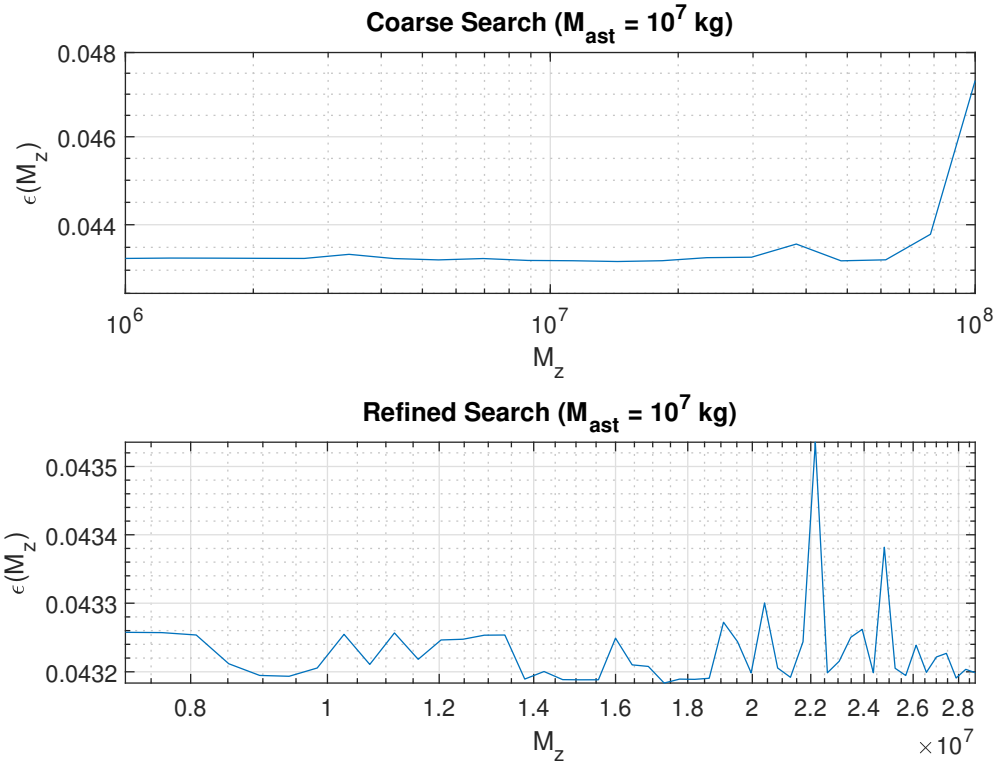

Figure 3.11: Parameter search for a 10^7 kg asteroid yielding no discernible dip in the cost function.

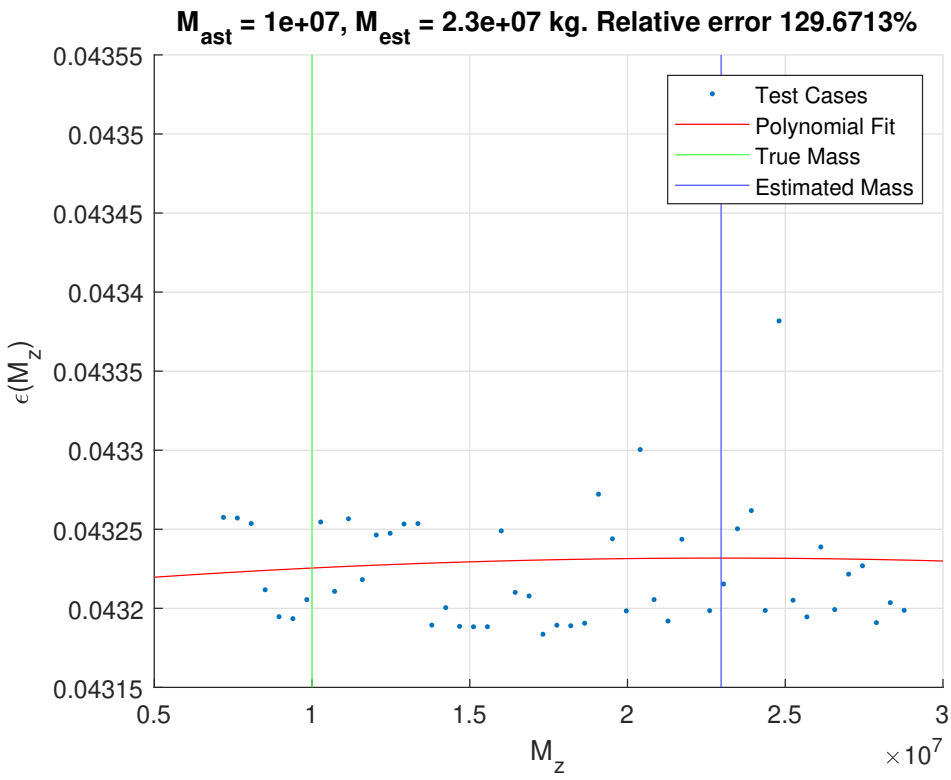

Figure 3.12: Poor quadratic fit for the 10^7 kg asteroid leading to an estimate with high error.

As this happens, the error on the mass estimate also increases. In order to investigate the performance of the system, this process was repeated for many different values of m_{true} to observe how the estimation error changes with m_{true}. The results of this analysis for the nominal flyby distance of 2 km can be seen in Figure 3.13.

This gives an important insight into the order of magnitude of the lower limit of mass estimation for this technique, depending on the desired level of accuracy. For example, if an accuracy of $\pm 20\%$ is desired, this technique may be suitable for asteroids down to the 10^8 kg mass range dependent on flyby conditions. For a monolithic, spherical asteroid with the density of olivine, this corresponds to a radius of 20.7 m. A rubble-pile type asteroid of the same mass would likely be larger, but of the same order of magnitude. For perspective, a monolithic asteroid weighing 10^{10} kg would have a diameter of 192 m.

It should be noted that the dynamics of the particular flyby will affect the gravitational interaction and thus the detectability of the perturbation. All sim-

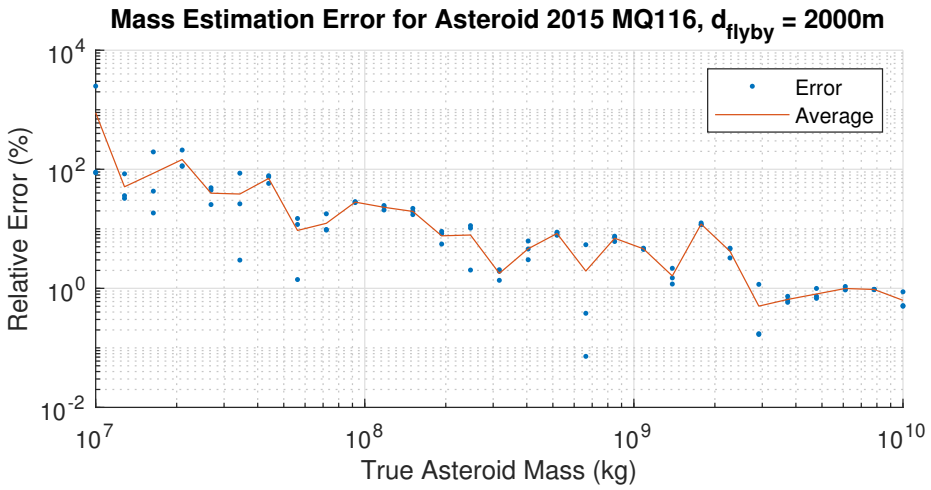

Figure 3.13: Accuracy of mass estimate in the base case of the NEOCORE flyby of asteroid 2015 MQ116, with a flyby distance of 2 km.

ulations up until this point have been performed for one specific target and flyby scenario, however the speed of the flyby will likely have an impact on the mass that can be probed with this technique - slower flybys would allow the same mass to produce a stronger perturbation, allowing lighter masses to be probed.

3.3.1 Addition of Angular Measurements

As well as range measurements, there is also scope for the full relative position of each satellite to be measured with respect to the other from optical data. If the camera already carried by the satellites for navigation and surface imaging is sensitive to the laser wavelength and shares a common pointing axis with the LRF receiver, the other satellite would appear as a bright point of light in the image. Combined with knowledge of the attitude of spacecraft A from star trackers, this would allow the full relative position of B to be measured in spherical coordinates. In total there are 5 possible observables - the two-way range, and 2-dimensional angle data from each spacecraft. These additional measurements may enhance the above method of mass estimation.

New equivalent measurement functions were constructed which extracts also the angle measurements in the heliocentric reference frame from the state at time t, thus for each time point we have 5 scalar values. Let the new measurement

set be $\mathbf{Z}$, the noise-free predicted measurement vector be $\mathbf{Y}(m_{ast})$, and their respective measurement functions be G and H:

$$\mathbf{Z} = \begin{bmatrix} G(\mathbf{X}(t_0)) \\ G(\mathbf{X}(t_1)) \\ G(\mathbf{X}(t_2)) \\ \vdots \end{bmatrix} \tag{3.25}$$

$$\mathbf{Y}(m_{ast}) = \begin{bmatrix} H(\mathbf{X}(t_0)) \\ H(\mathbf{X}(t_1)) \\ H(\mathbf{X}(t_2)) \\ \vdots \end{bmatrix} \tag{3.26}$$

$$G(\mathbf{X}(t)) = \begin{bmatrix} R(\mathbf{X}(t)) \\ \theta_1(\mathbf{X}(t)) \\ \theta_2(\mathbf{X}(t)) \\ \phi_1(\mathbf{X}(t)) \\ \phi_2(\mathbf{X}(t)) \end{bmatrix} \tag{3.27}$$

$$H(\mathbf{X}(t)) = G(\mathbf{X}(t)) + \begin{bmatrix} \mathcal{N}(0, \sigma_r) \\ \mathcal{N}(0, \sigma_\theta) \\ \mathcal{N}(0, \sigma_\theta) \\ \mathcal{N}(0, \sigma_\phi) \\ \mathcal{N}(0, \sigma_\phi) \end{bmatrix} \tag{3.28}$$

Here the functions $R(\mathbf{X}(t))$, $\theta_1(\mathbf{X}(t))$, $\theta_2(\mathbf{X}(t))$, $\phi_1(\mathbf{X}(t))$ and $\phi_2(\mathbf{X}(t))$ extract the 5 scalar observables, which have uncertainties σ_r on the range, and σ_θ, σ_ϕ on the angular measurements. Note here that $G(\mathbf{X}(t))$, the set of measurements collected at time t, is now a 5-element vector. An equivalent cost function was used which incorporates the additional angle measurements:

$$\epsilon_5(m_{ast}) = \sum_{i=1}^{N} (\mathbf{Z}_i - \mathbf{Y}_i(m_{ast}))^2 \tag{3.29}$$

where all 5 observables are equally weighted. σ_θ and σ_ϕ were set to 1 mrad,

equivalent to one pixel width for a wide-angle camera with a 60 degree field of view and a 1024-by-1024 pixel sensor. In reality the angular uncertainty may be less than this due to the ability to locate the centroid of a point source to sub-pixel precision and accuracy, but only the pessimistic case was considered here. It was found that when using this new 5-dimensional cost function, no improvement in the performance of the estimation technique was gained over the range-only case. This is likely because the flyby configurations investigated did not cause any significant differential perturbation in directions orthogonal to the vector connecting the two spacecraft. Thus, moving forward, the one-dimensional case (range) only was considered.

3.3.2 Effect of Flyby Distance on System Performance

One important factor in the strength of the gravitational interaction and thus the magnitude and detectability of any deflection is the flyby distance. Until now we have considered only symmetrical, 2 km flybys of the asteroid as the base case, but it is not yet clear how the flyby distance impacts the mass estimation process.

To investigate this, the previous assessment of estimation error was repeated for different flyby distances - 0.5 km, 5 km, 10 km and 25 km, again with a symmetrical flyby with the asteroid directly in the middle of the two satellites. A separate assessment of the GNC chain and orbit determination capabilities for both the satellites and the asteroid would be required to determine the closest possible flyby that is achievable safely, however, this is beyond the scope of this Chapter and thesis and is left for future work. The estimation performance as a function of m_{ast} for each of these cases can be found in Figures 3.14 - 3.16.

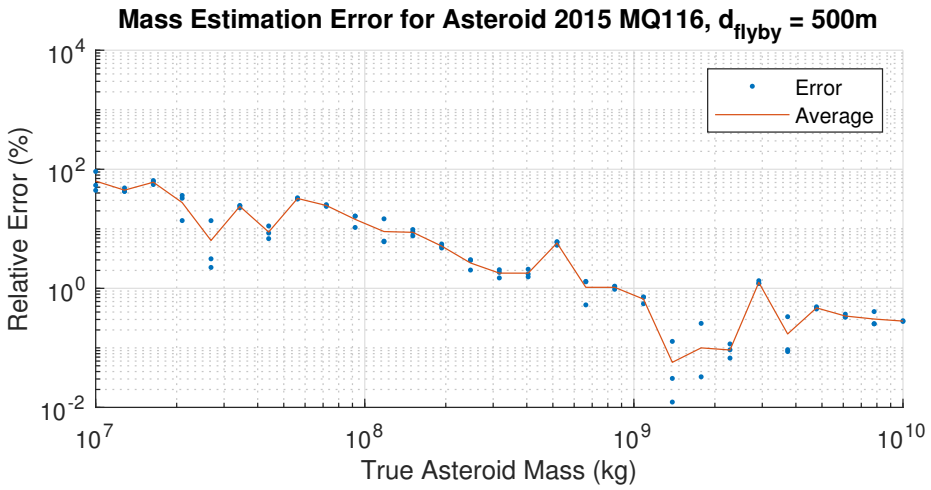

Figure 3.14: System performance for asteroid 2015 MQ116, flyby distance 500 m.

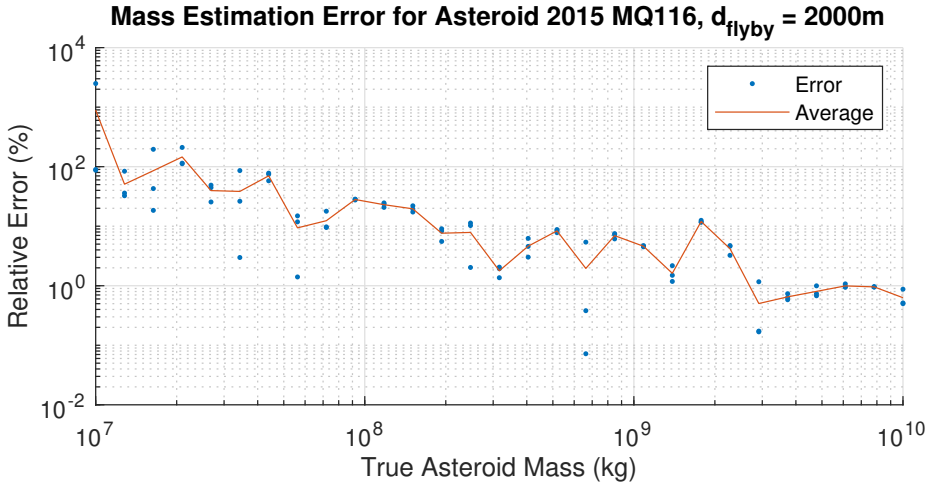

Figure 3.15: System performance for asteroid 2015 MQ116, flyby distance 5 km.

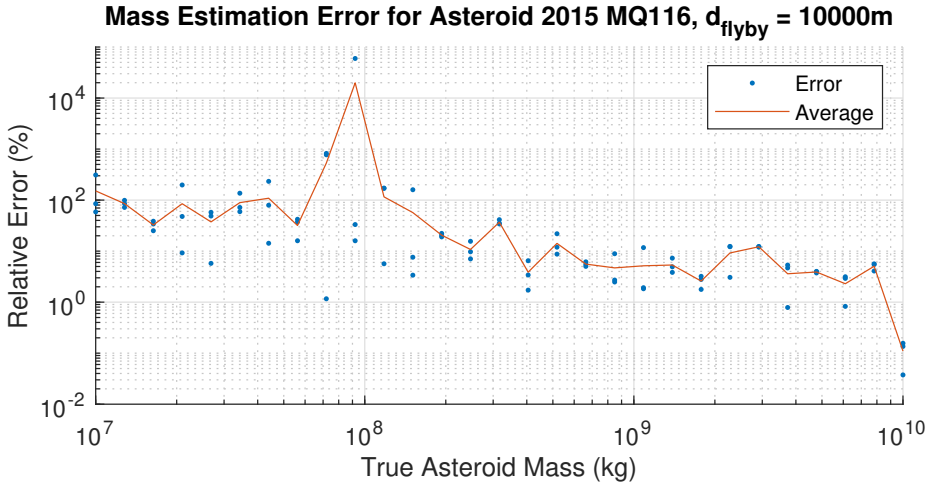

Figure 3.16: System performance for asteroid 2015 MQ116, flyby distance 10 km.

It can be seen from these results that there is indeed a noticeable advantage to achieving a close flyby - for example, comparing a 10 km flyby with a 500 m flyby, for the 10^9 kg asteroid there is a reduction in estimation error of around one order of magnitude. This helps inform the selection of flyby distance depending on the desired level of estimation accuracy - for example, for asteroid deflection attempts the accurate estimation of the mass is more critical than for purely scientific missions, as the penalty for error may be far larger.

3.3.3 Alternative Flyby Geometries

The base case for flyby geometry up until this point, has been for both spacecraft to be equidistant from the asteroid, with the asteroid on the connecting line between the satellites at the moment of flyby. this is illustrated in Figure 3.17, where the relative positions and velocities of the two spacecraft with respect to the asteroid are denoted by $\mathbf{r}_{1,2}$ and $\mathbf{v}_{1,2}$ respectively. However, it is entirely possible that other configurations may enhance or reduce the performance of the system. Thus the efficacy of this new technique under different flyby geometries should be investigated also.

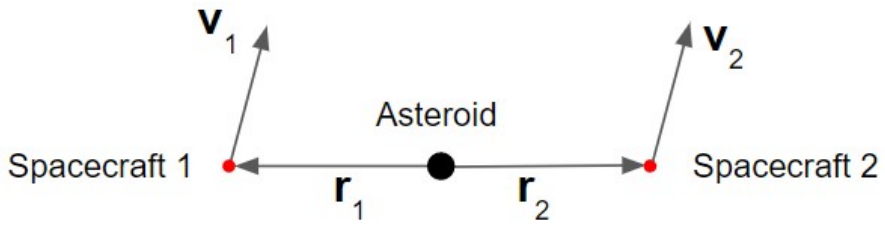

Figure 3.17: Illustration of the moment of closest approach in the base case.

Approximating the net gravitational change in velocity as an impulsive ΔV applied at the moment of closest approach (since the flyby is extremely fast, on the order of 10 kms^{-1}), the magnitude of the velocity change of satellite i must be proportional to $1/r_i^2$ and in the direction of $-\hat{\mathbf{r}}_i$, where r_i is the distance between the satellite and the asteroid's centre of mass:

$$\Delta \mathbf{v}_1 \propto -\frac{\hat{\mathbf{r}}_1}{r_1^2} \tag{3.30}$$

$$\Delta \mathbf{v}_2 \propto -\frac{\hat{\mathbf{r}}_2}{r_2^2} \tag{3.31}$$

Since we aim to measure the *relative* deflection only, the magnitude of the relative change in velocity is the only parameter of importance. This can be written as

$$\|\Delta \mathbf{v}_{rel}\| \propto \|(\frac{\hat{\mathbf{r}_2}}{r_2^2} - \frac{\hat{\mathbf{r}_1}}{r_1^2})\| \tag{3.32}$$

.

Since in the base case they are collinear, the imparted Δv will be along this same line. Generalising this to cases where the asteroid is not on the line connecting the two spacecraft, which we shall call $\mathbf{s}$, we have

$$\|\Delta \mathbf{v}_{rel}\| \propto \|(\frac{\hat{\mathbf{r}_2}}{r_2^2} - \frac{\hat{\mathbf{r}_1}}{r_1^2}) \cdot \hat{\mathbf{s}}\| \tag{3.33}$$

.

In the reference frame of the spacecraft pair, Equation 3.33 can be used to compute the magnitude of the relative trajectory deflection if the asteroid passes by the pair at different points. This can be seen in Figure 3.18 where the logarithm of $\|\Delta \mathbf{v}_{rel}\|$ is represented by the contour. Here brighter areas indicate regions where, if the asteroid were to pass though these locations, the relative velocity change would be larger.

This result indicates that the base case is not that which will produce the strongest and most detectable deflection for a given mass of asteroid. Cases where the asteroid passes closer to one of the satellites while still residing on the connecting axis will produce stronger and more easily detectable deflections.

To confirm this, several different alternative flyby geometries were simulated as follows:

- On-axis, asymmetric. Asteroid is closer to one satellite, but remains on the

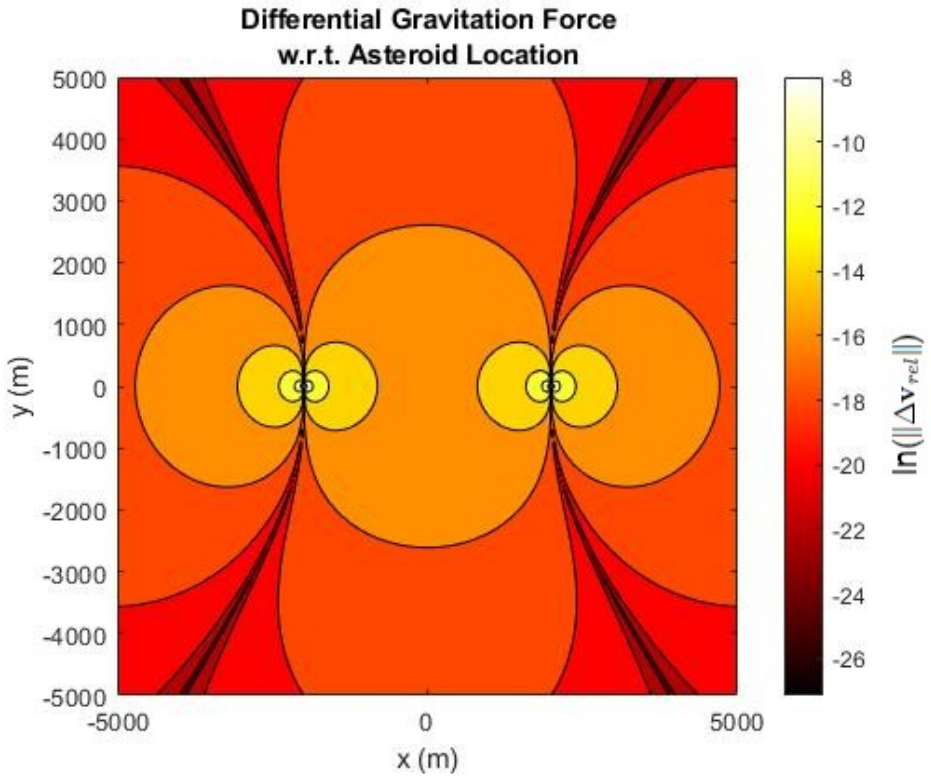

Figure 3.18: Strength of differential gravitational force w.r.t. asteroid flyby location. Satellites are located at y = 0 and x = ± 2000 m. Logarithm of relative velocity change displayed on the colour axis.

connecting axis.

- Off-axis, asymmetric. Asteroid is closer to one satellite, and off the connecting axis.
- On-axis miss. Asteroid is on the connecting axis, but does not pass between the spacecraft.
- Off-axis miss. Asteroid does not pass between the spacecraft, and is not on the connecting axis.

It should be noted that this is not an exhaustive test of all possible configurations - for example, configurations with the satellites arriving non-simultaneously (one trailing the other) represents a different category of geometries that could be considered. In some of these cases, the deflection would not be primarily along the connecting vector between the two spacecraft, but there may also be a more significant orthogonal component, perhaps making angle data more relevant. However, in this Chapter and thesis we will focus primarily on configurations with a simultaneous flyby.

System performance was again simulated for a range of masses in each configuration. Results for each configuration, and illustrations of each configuration, can be seen in Figures 3.19 - 3.26.

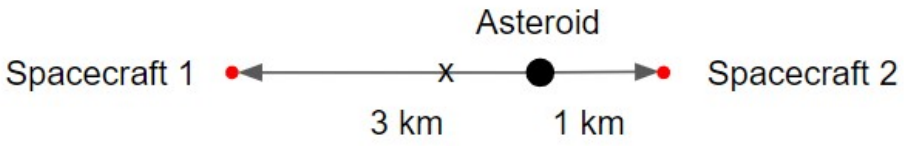

Figure 3.19: On-axis, asymmetric configuration. Central point between the satellites marked by X.

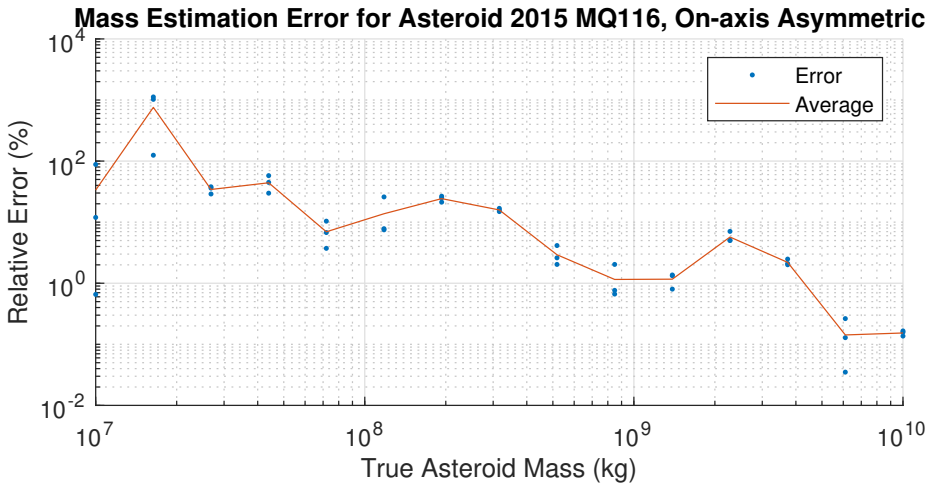

Figure 3.20: Mass estimation error vs true mass for on-axis asymmetric flyby geometry (Figure 3.19).

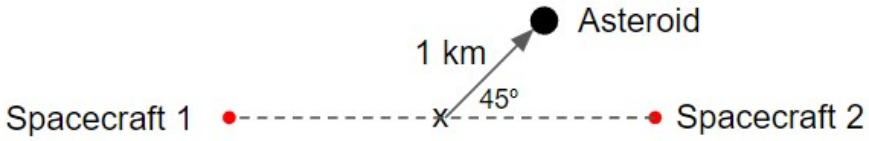

Figure 3.21: Off-axis, asymmetric configuration. Distance from centre point is the same as in the on-axis asymmetric case.

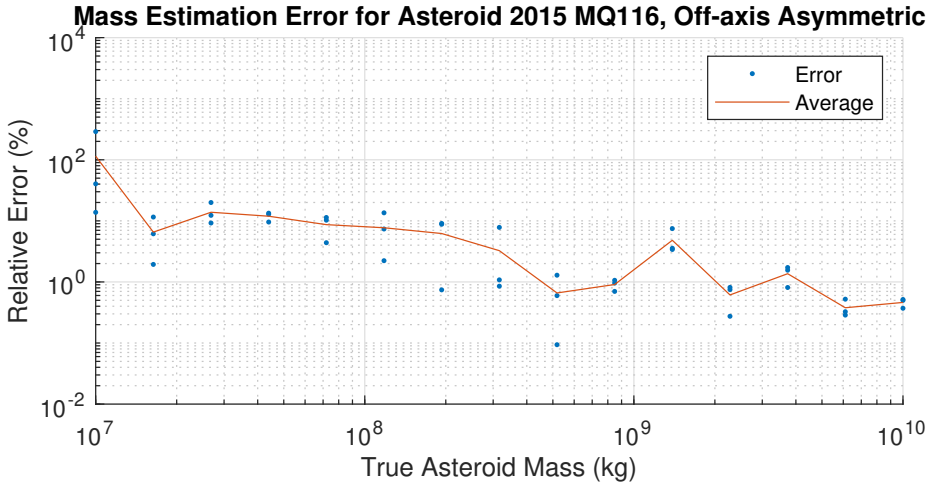

Figure 3.22: Mass estimation error vs true mass for off-axis asymmetric flyby geometry (Figure 3.21).

These results in combination with prior results in Figure 3.13 which uses the

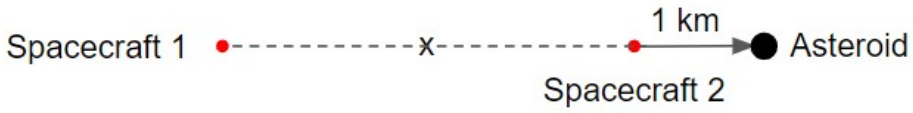

Figure 3.23: On-axis miss configuration.

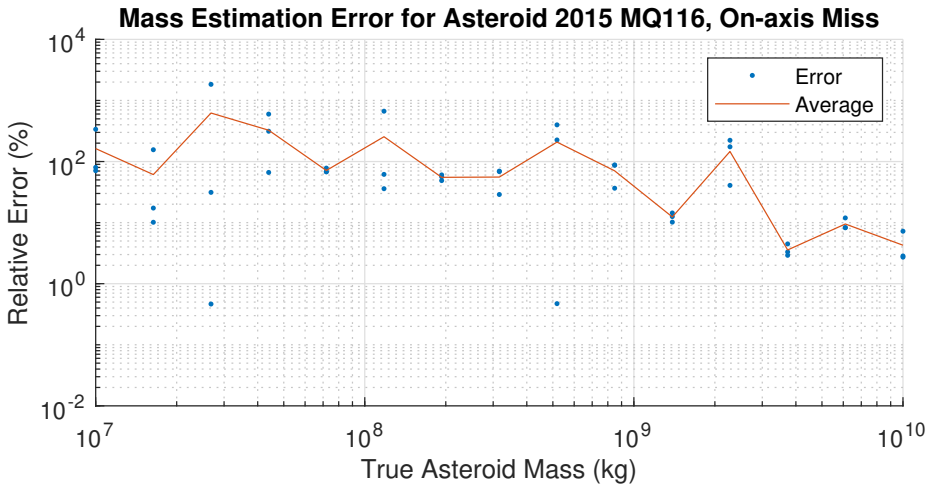

Figure 3.24: Mass estimation error vs true mass for on-axis miss flyby geometry (Figure 3.23).

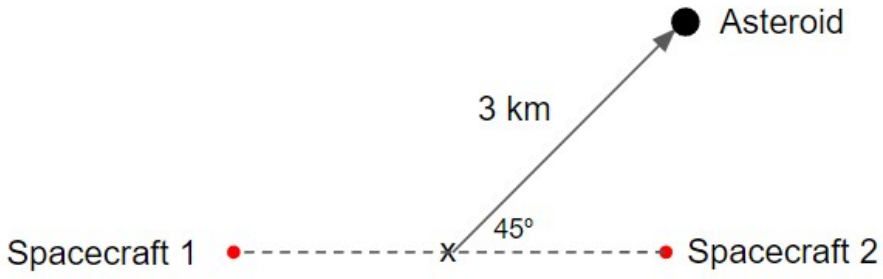

Figure 3.25: Off-axis miss. Distance from centre point is the same as in the on-axis miss case.

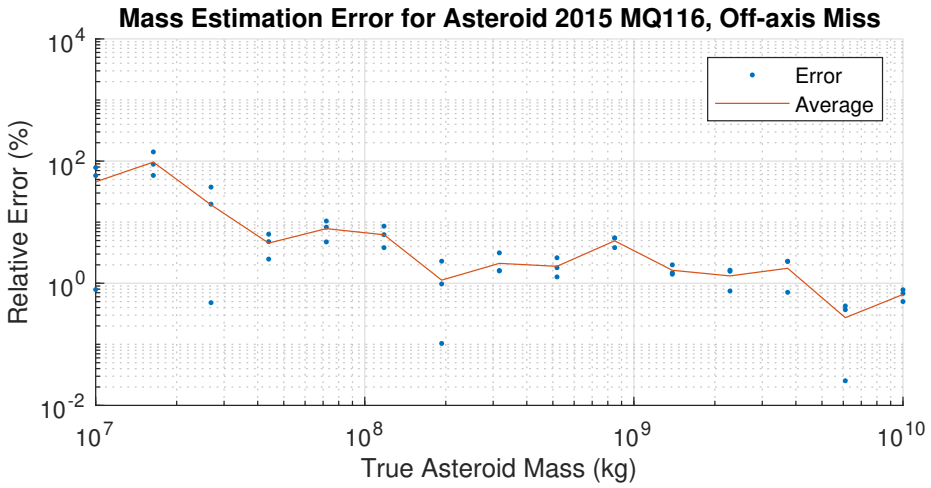

Figure 3.26: Mass estimation error vs true mass for off-axis miss flyby geometry (Figure 3.25).

same satellite separation, show that these four alternate geometries perform similarly or slightly better than the original nominal geometry. This is in agreement with Figure 3.18, which shows that the central point between the two satellites is not the optimal position for the asteroid to fly by to maximise the differential gravity, and rather alternative configurations should be considered.

3.4 Flyby Targeting Error

Until this point, uncertainties in the state vector have been neglected to determine the best flyby configuration to target under ideal circumstances, however to better estimate the real-world mass estimation error attainable, these effects should be included.

Relevant errors in the state vector are the spacecraft pair's barycentre with respect to the asteroid, and the two spacecrafts' state relative to each other. Since the spacecraft will carry high-accuracy ranging equipment, only the former will be studied in detail as the uncertainty will clearly be significantly larger and have a more significant effect than the uncertainty in the spacecraft's position relative to one another.

Although a rigorous treatment of the GNC systems is outside the scope of this thesis and not within the author's area of expertise, we may still obtain

an order of magnitude estimate by considering that the dual cameras, allowing binocular vision and parallax to be leveraged, may be used to estimate range and asteroid diameter on approach, as well as the asteroid's approximate location on the flyby plane. This means that the computer will be able to update the actual position of the three bodies at the moment of flyby retrospectively, and that the experiment is not limited by the estimated relative trajectory prior to the flyby. In the ideal case, images of the asteroid at the instant of flyby will be obtained, likely allowing the asteroid's centre of mass (CoM) position to be reconstructed to sub-asteroid-diameter accuracy. In the more likely scenario, the asteroid will be out of frame at the instant of flyby, and its position would need to be inferred from the observed trajectory in the s leading up to the flyby, causing errors on the order of several asteroid diameters in the CoM position reconstruction. This is the case which we will study for the final mission simulation.

Previously, trajectories were simulated by 'arranging' the configuration of the spacecraft w.r.t. the asteroid at the moment of flyby, propagating backward in time one day to the beginning of the observation period to obtain the initial state, and then propagating this initial state through the flyby and using intermediate states to extract simulated measurements. The same process is performed when attempting to fit the flyby model to this set of simulated observations. The process is now modified slightly to include targeting error: in the run that produces the simulated measurement set, the flyby configuration is modified by moving both spacecraft relative to the asteroid by an error vector in the plane of the 3 bodies, with constant magnitude and random direction. Subsequent runs in the model fitting process have no knowledge of the error and simulate for the perfectly targeted case, thus there is an error between the assumption of the model and the 'true' flyby scenario which generated the simulated measurement set.

For these final simulations with targeting error included, we will simulate only the on-axis asymmetrical configuration from before (1 km and 3 km flyby distance), as previous results indicated this configuration has the best potential for accurate mass estimation. Results for this case, with standard deviation of the targeting error of 100 m and 1000 m can be found in Figures 3.27-3.28. These

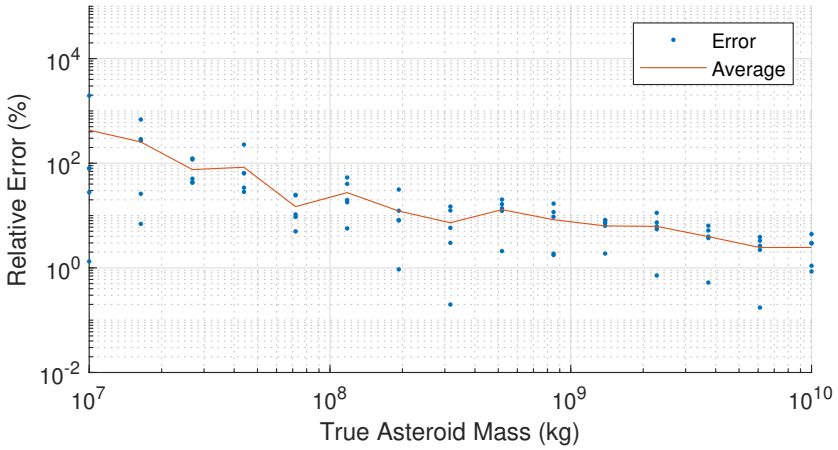

Figure 3.27: On-axis asymmetric flyby configuration with targeting error, $\sigma = 100$ m.

results show an increased mass estimation error compared to Figure 3.20, with approximately 7% error for the 10^9 kg asteroid with 100 m targeting error, and a 30% estimation error with 1000 m targeting error.

3.5 Application in the NEOCORE Mission

The NEOCORE mission concept (Walker et al., 2021) proposes a new mission framework to enable the large-scale exploration of asteroids at a comparatively low cost per object visited, while also maximising scientific return from each object, recovering information including accurate orbital elements, topological characterisation, and estimation of object mass.

NEOCORE trajectories are designed with the aim of maximising the number of NEAs that can be explored within the given $\Delta\mathbf{V}$ budget, and per launch. To achieve this, many identical satellites are launched together, each embarking on different trajectories. No single trajectory was targeted for the concept, rather a flexible algorithm to find viable trajectories dependent on launch date was developed. To reduce the overall propellant expenditure and maximise the number of targets, only flybys were considered. By comparison with the entire JPL Small Body Database, solar orbits with a naturally high number of NEA approaches were identified. This allows relatively small trajectory correction ma-

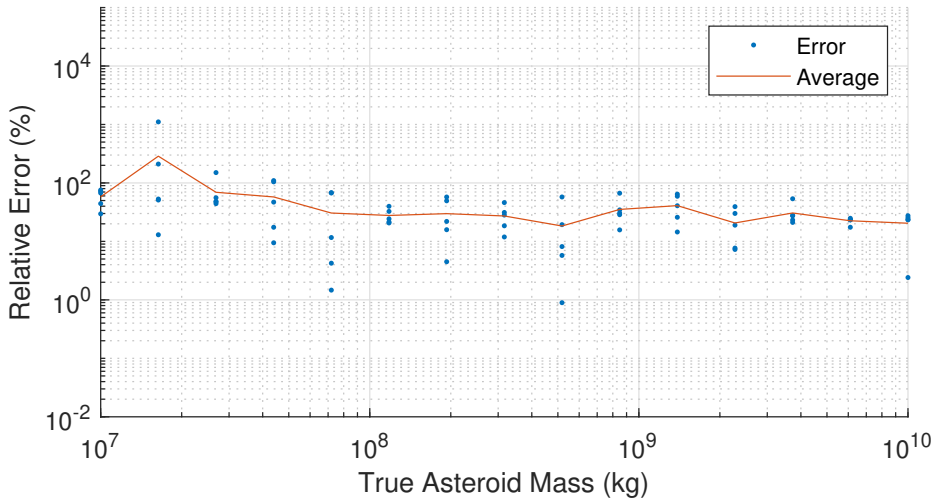

Figure 3.28: On-axis asymmetric flyby configuration with targeting error, $\sigma = 1000$ m.

neuvers (TCMs) to be performed to adjust the orbit, reducing the flyby distance with each object to nearly zero.

The mission timeline proceeds as follows. After launch, satellites escape Earth's sphere of influence with assistance from a kick stage carrying, in the baseline design, 6 satellites. After being released from the kick stage, each satellite commences its own separate asteroid tour, beginning with a transfer to its initial solar orbit (ISO). After transfer to the ISO, the satellite waits until the first encounter nears, at which point an optical observation campaign begins to better determine the orbit of the asteroid and improve its ephemeris beyond what is possible using only Earth-based measurements. This allows TCMs to be calculated and performed to achieve an extremely close flyby of the asteroid in the remaining time before the flyby. After TCMs are completed, the spacecraft enters the measurement phase of the mission, capturing images and other scientific data. After the flyby, the spacecraft then awaits the next set of TCMs which adjust the trajectory to fly by the next object. This process repeats for each asteroid in the tour. It was common to find trajectories which enabled >5 asteroids to be flown by within a ΔV budget of 2 kms^{-1} and mission duration of 3 years, and some trajectories were even found with over 10 asteroid encounters.

Since the NEOCORE concept employs fast flybys, the technique for mass es-

timation proposed in this Chapter is well-suited for application to this mission concept. The low required pulse energy, and hence low size, mass and power of instrumentation is compatible with the CubeSat platform. This does require, however, that the NEOCORE satellites be launched in pairs rather than single satellites, which effectively doubles the cost per object visited. However, since the original concept already proposed a multi-satellite launch with all satellites being identical, this fundamentally requires no change to the mission architecture. Travelling in pairs has the added advantage of redundancy, where if one satellite fails, the other may still continue and continue to return useful data, albeit without the mass estimation experiment. This also enables one spacecraft to be used as an impactor in the final asteroid of the series, with the other imaging the ejecta to probe composition and structure.

In the NEOCORE concept (Walker et al., 2021), objects with a diameter of less than 50 m were discarded from the database as these are less interesting from a planetary defense perspective. Assuming a spherical asteroid comprised of olivine, this lower size limit translates to a lower mass limit of $1.5\text{x}10^9$ kg. From the results presented in this Chapter, it is expected that mass estimation on objects of this size could be performed with $\pm 10\%$ error.

3.6 Discussion

In this Chapter, a novel method of mass estimation for asteroids and similarly sized celestial bodies was proposed and investigated to determine the efficacy and performance of the method. A detailed sensor model was constructed to estimate the performance of a two-way ranging system, which was then used to develop a full mission simulation, producing simulated measurement sets for asteroids of arbitrary mass.

It was shown that the simulated TWR data from such a flyby could be used to accurately estimate the mass of asteroids down to approximately 10^8 kg with 10% error depending on the flyby distance, using the nominal case of a symmetrical, 2 km dual flyby. This is a significantly lower mass than has been probed in previous

missions, with the additional key advantage of being attainable using a fast flyby rather than an orbiter. The addition of angle measurements of each spacecraft's relative position was tested, but did not improve the mass estimation.

Additional flyby geometries were also investigated, first analytically by approximating the net gravitational perturbation as an impulsive ΔV, and then by numerically simulating several alternative scenarios. It was found that the base case in the original NEOCORE proposal was not the optimum geometry for maximising the relative trajectory deflection; more asymmetric geometries offer improved mass estimation performance.

Chapter 4

Laser Ranging using CCD Sensors

In the previous Chapter, formation flight and relative state monitoring between two satellites was used to estimate the mass of asteroids during a dual flyby. New applications for formation flight such as the aforementioned technique for exoplanet observation are beginning to be explored, and will require methods to monitor the relative position and velocity of two or more satellites. This Chapter will outline and present simulations of a novel technique for ranging using a standard CCD camera sensor as the only detection component, eliminating the need for high-precision pulse timing circuitry. The new technique also does not require ultrashort pulses in order to achieve high range accuracy; in fact, its performance is improved with longer pulses in the millisecond range. Thus it is feasible to use this technique with a modulated CW source. The effect of clock asynchronisation will also be analyzed, and it will be shown to have little impact on the accuracy of the measurement. These attributes together mean that the hardware required to construct this new sensor is extremely simple and cheap to manufacture. The tradeoff is that the integration time is longer, however due to the nature of the mass estimation experiment, where range measurements are collected over a period of days, this will not be a problem. Thus this technique may be an attractive option for ranging in the context of the NEOCORE mission or similar scenarios where the distance to be measured is not rapidly changing.

4.1 Technique Overview

Consider two stations A and B connected by a lossless laser link, separated by a distance s. Emitter A transmits a series of pulses, each with a predetermined yet random duration and followed by a pause, also of predetermined, random duration. If B knows in advance the transmission schedule and pulse shape emitted by A, $P_A(t)$, then it is trivial to predict the total number of photons that will be collected by receiver B in any given time window $t_0 < t < t_0 + t_E$:

$$N_B(s, t_0) = \frac{hc}{\lambda} \int_{t_0}^{t_0+t_E} P_A(t - \frac{s}{c})dt \tag{4.1}$$

where λ is the laser wavelength.

This integration requires knowledge of s, however the total collected energy can be indirectly measured from the CCD array, as their raw output is simply photon count data on a per-pixel basis. Equation 4.1 represents the number of photons collected in a single frame - if we introduce the possibility of having multiple frames, we can construct the measurement vector $\mathbf{y}(s)$, which contains the expected number of counts measured in each frame if the distance between the stations is s:

$$\mathbf{y}(s) = \begin{bmatrix} N_B(s, t_0) \\ N_B(s, t_1) \\ N_B(s, t_2) \\ \vdots \end{bmatrix} \tag{4.2}$$

where the frames begin at times t_0, t_1 etc. There is no requirement that the frames are contiguous, subsequent exposures may begin after any arbitrary processing time required to read the CCD. We can also construct the vector $\mathbf{g}(s)$ which is the vector that in reality would contain the true measurement data, but here contains simulated data:

$$\mathbf{g}(s_{true}) = \begin{bmatrix} \mathcal{P}(N_B(s_{true}, t_0)) \\ \mathcal{P}(N_B(s_{true}, t_1)) \\ \mathcal{P}(N_B(s_{true}, t_2)) \\ \vdots \end{bmatrix} + \mathbf{N} \tag{4.3}$$

where $\mathcal{P}(\lambda)$ represents a number generated according to the Poisson distribution with mean λ, and $\mathbf{N}$ is a vector containing aggregated noise terms for each frame - for example from dark counts.

We can now obtain an estimate of the separation s_{est} by minimising the following cost function with respect to s:

$$F(s) = \sum_{i}^{N_{frames}} (\mathbf{y}_i(s) - \mathbf{g}_i(s_{true}))^2 \tag{4.4}$$

$$s_{est} = \min_{s} F(s) \tag{4.5}$$

The data sets $\mathbf{g}_i$ for each frame would be recovered by integrating the counts over several pixels in the immediate vicinity of the source in the sensor plane. At any significant distance, the source, likely a small laser diode, would be small enough to be treated in the model as a point source, and thus its image would be equivalent to the point spread function of the optics. Thus the photon count would be taken as the sum over some region surrounding the centroid of the point's image which contains the entire PSF (illustrated in Figure 4.1).

4.2 Feasibility Study

A simple model is now constructed to determine if this approach is feasible and the possible accuracy that may be attainable. The pulse train $P_A(t)$ is created by generating normally distributed random durations for each successive pulse and pause state. Pulse shape is modelled as a square, with an instantaneous transition between on and off states at each boundary, although other pulse profiles are equally valid. For both pulses and intervals, the mean and standard deviation

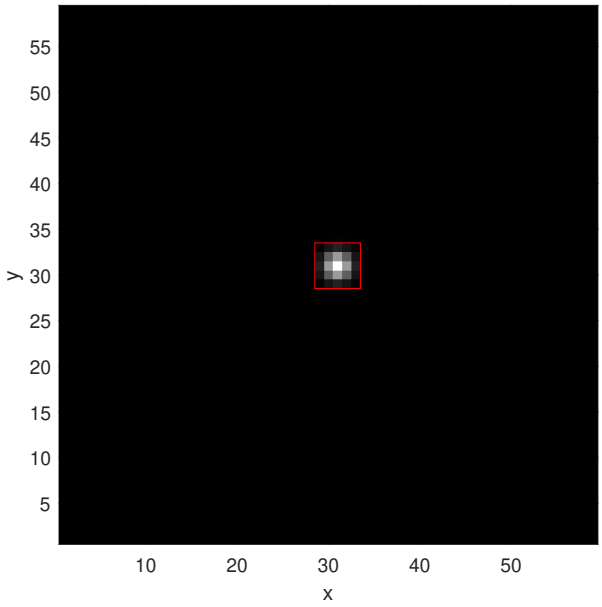

Figure 4.1: Example of a region surrounding the PSF centroid over which pixel counts should be aggregated to obtain **g** for real measurements. Axes correspond to individual pixels on the sensor.

of durations is 5 ms and 1 ms respectively. Relatively long pulse and interval durations were chosen for two reasons - firstly, if the duration of pulses and intervals is much shorter than the exposure, then from the camera's perspective this becomes similar to a CW laser and very little difference would be observed as s varies. Secondly, this has the added advantage of not requiring complex short pulse generation hardware - a simple electrically modulated diode laser would suffice. This modulated diode laser in combination with the standard CCD sensor means the entire system requires very simple, readily available components.

For this initial test, a true separation of $s = 1000$ m was used, with an exposure duration of 5 ms and 100 frames, or a total integration time of 0.5 s, and the noise term **N** was neglected. A plot of the cost function $F(s)$ can be found in Figure 4.2, where no noise sources have yet been included. It is clear from this that not only is there a significant reduction in the cost function around the true station separation - hence the proposed technique indeed allows the distance to be extracted from this data set - but also that the performance is rather good with sub-centimeter levels of precision appearing to be possible in this ideal case.

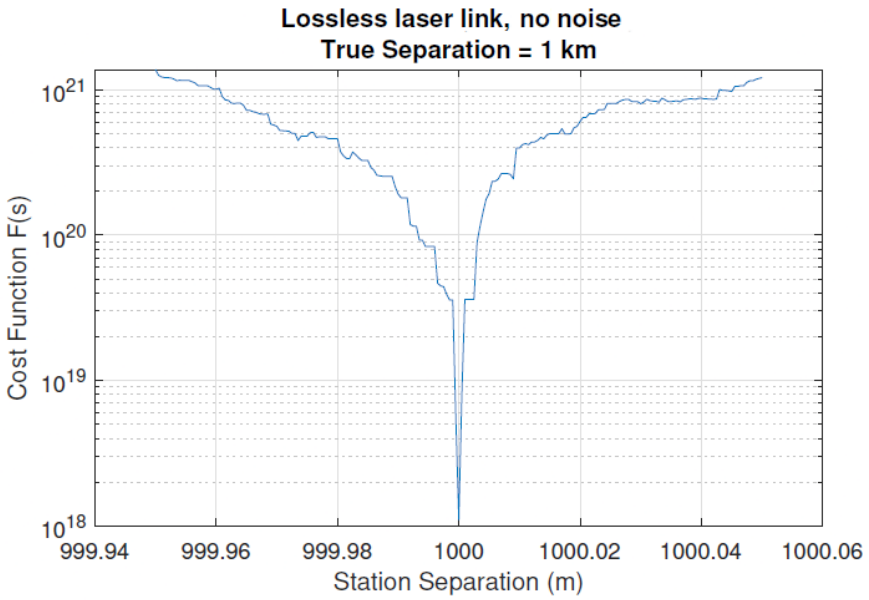

Figure 4.2: Feasibility study with a lossless laser link operating at 1 km station separation and 100 frames of 5 ms each.

4.3 Model Improvements

In the initial model, some details and noise sources were neglected for the sake of the proof of concept, which will be added to the model in this section in order to estimate both the possible performance and requirements in terms of total exposure duration.

Firstly, several modifications must be made to Equation 4.1 to account for real-world effects (i.e. the laser link is not lossess) to more accurately model a real system. The most important of these are beam divergence, optical efficiency losses and clock asynchronisation.

4.3.1 Optical Losses

Real free-space laser beams are not perfectly collimated. This means, at large distances, the effective beam area and hence power are dependent on the distance to the source and the divergence angle.

For a Gaussian beam profile, the effective spot area varies along the beam axis with distance s from the beam waist according to Equation 4.7:

$$r_b(s) = w_0 + s \tan \theta_{div} \tag{4.6}$$

where w_0 is the waist radius and θ_{div} is the divergence half-angle. Thus the beam area at distance s is

$$A_b(sz) = \pi(w_0 + s \tan \theta_{div})^2 \tag{4.7}$$

.

To loosen the pointing accuracy requirement, this finite beam area should be significantly larger than the aperture. This ensures that the satellite does not drift in and out of the beam during integration, and enables easier acquisition of the target in the sky before the sensor has 'locked on' to the emitter location. Due to this effect, a large portion of the beam misses the aperture and does not contribute to the signal collected, i.e. Equation 4.1 becomes

$$N_B(s, t_0) = A_{col} \frac{hc}{\lambda} \int_{t_0}^{t_0+t_E} P_A(t - \frac{s}{c}) \frac{1}{A_b(s)} dt \tag{4.8}$$

assuming a flat power distribution across the beam radius. In reality the beam would have a non-flat profile, such as a Gaussian profile, however any misalignment from the centre would not affect the location of the local minimum of the cost function, so long as the lateral drift rate of the aperture with respect to the beam axis is low. Equation 4.8 can be used again with the same cost function to estimate the separation of the stations. Results after accounting for these effects can be seen in Figure 4.3.

It can be seen that, again, sub-centimeter range resolution can be achieved, and also that the curve is much smoother, making local minimum detection easier.

Now, additional instrumentation noise terms must be added to the model. A CCD dark count rate of 10 Hzpx^{-1} was used, consistent with dark count rates demonstrated in cameras for spacecraft utilising active cooling of the sensor (Gilard et al., 2010). For the previous 5 ms exposure, this results in an average of only 1.25 counts per exposure in the integrated area. For the readout noise, a value of 5 counts per exposure per pixel was used. Pixel-level noise terms are

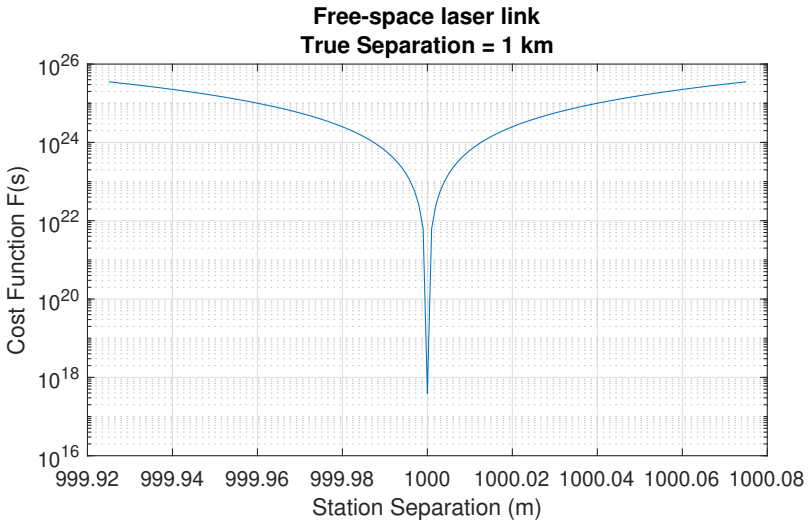

Figure 4.3: Improved model including effects of free-space laser propagation. Poisson noise only.

added by choosing a number of pixels to integrate across, which is large enough to contain the full PSF of the imaging system - for example, a 5x5 pixel region. In this case, a noise term corresponding to 25 pixels is added to the overall signal collected from the source. The noise term is thus

$$N = n_i(\mathcal{P}(Dt_E) + \mathcal{P}(R)) \tag{4.9}$$

where n_i is the number of pixels that the count is aggregated across, in this case 25, D is the dark count rate per pixel, and R is the readout noise per pixel.

Adding these new noise terms and optical efficiency corrections, the final expression for the number of photons collected is

$$N_B(s, t_0) = A_{col}\eta_{optics}\frac{hc}{\lambda}\int_{t_0}^{t_0+t_E} P_A(t - \frac{s}{c})\frac{1}{A_b(s)}dt + N \tag{4.10}$$

where the final term captures the two noise count sources in the form of a sum over n pixels, each contributing a Poisson-random number of photons with their respective means. Here η_{optics} is the overall photon-to-electron efficiency of the optical system, from aperture to CCD, set at 0.2 as an estimate. The peak power value (laser-on state) of P_A is now adjusted from the previous value of 1 W to 5 mW, and radius of the collecting optics is set to 1 cm. Results with these

modifications can be seen in Figure 4.4.

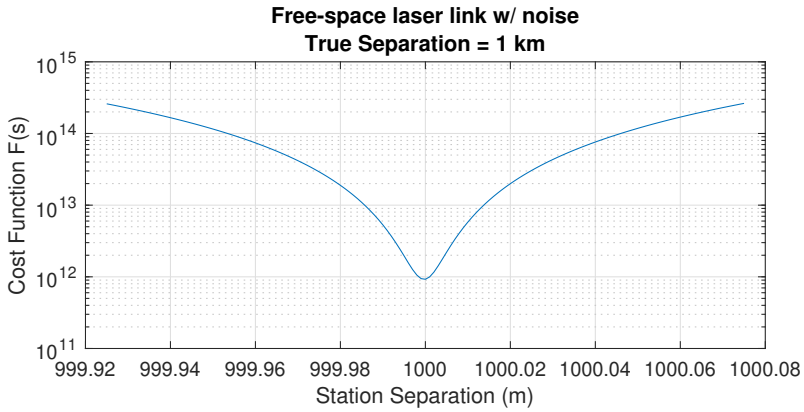

Figure 4.4: Further improved model including dark and read noise terms with adjusted laser/optics parameters.

It can be seen that the curve shape remains quadratic with a very clear, smooth local minimum even after adding noise terms, reducing aperture size, reducing laser power and using a highly divergent beam. The curve is now significantly smoother than before due to the addition of Poisson noise smoothing out the thresholds as temporal 'edges' of individual pulses move from one exposure to the next. The overall magnitude of the cost function values is now lower primarily due to the reduction in laser power. Fitting a quadratic to the above curve, the station separation recovered from the simulated measurement data was accurate to within 0.3 mm. Repeating this simulation 10 times yielded a near-zero mean error of -0.115 mm with a standard deviation of 1.40 mm.

4.3.2 Clock Asynchronisation

The described method relies on prior knowledge of the start time of the pulse train - which, to know to high precision, requires synchronisation of the clocks between the two spacecraft. The two clocks cannot be synchronised to infinite precision, and will both be subject to differential drift over time as any mission progresses. The effect of clock asynchronisation is investigated here by adding a new time offset term t_{async} inside the expression P_A which captures this mismatch of clocks when calculating the simulated measurements. Note that this new term

is not included in the calculation of $\mathbf{y}(s)$ since it is unknown to the operating satellite.

Setting t_{async} to a nonzero value shifts the pulse train in time - in a traditional short-pulse TWR system, any unknown time offsets lead to systematic errors on the measured range equal to the equivalent light travel distance. Chip scale atomic clocks are currently available for space applications (for example, the Microsemi SA.45s CSAC) with accuracy better than 10^{-10} s, corresponding to a light travel distance of approximately 3 cm which is a limiting factor in accuracy for such systems.

When setting t_{async} to 1 ns in this model however, the error is not noticeably larger than the previous model which effectively had $t_{async} = 0$ s. This indicates lesser dependence on clock synchronisation than traditional systems. t_{async} was then increased to higher values to determine if and when clock asynchronisation becomes a problem. The effects of increasing t_{async} on the estimation error can be seen in Figure 4.5.

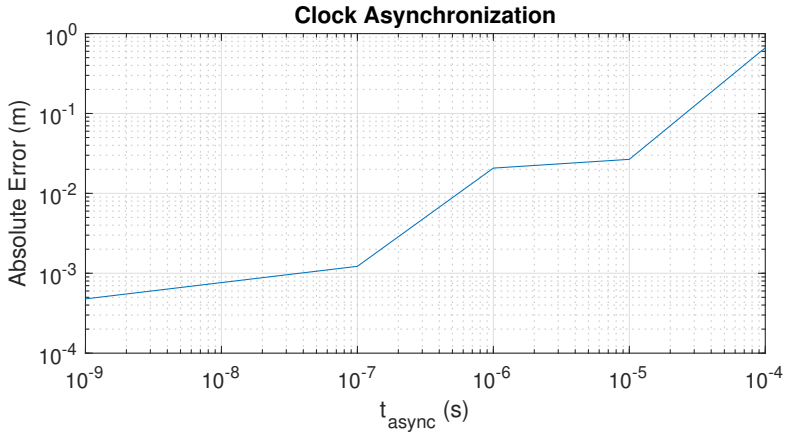

Figure 4.5: Effect on increasing clock asynchronisation on measurement error at 1.5 km separation.

It can be seen from Figure 4.5 that even with a relatively high asynchronisation of 10^{-7} s, the error is still on the order of millimetres, which is sufficient for high-precision space applications such as the mass estimation experiment proposed previously.

With this architecture, since the timescale of pulses and pauses is on the order

of 10^{-3} s, these variations have effectively no impact on the collected power in a given exposure. For example, in the worst case scenario, a section of a pulse with width t_{async} will be either missed or added to the integrated exposure. With the above parameters, the number of photons collected in a single frame is of the order 10^{10}, while the photon rate when the laser is on is $4.4\text{x}10^{12}$ photons s^{-1}. An asynchronous offset of 10^{-10} s typical of atomic clocks would thus only cause a difference of 440 photons - an almost undetectable change. It is clear how even larger offsets on the order of nanoseconds would still be many orders of magnitude smaller than the cost function and thus only quite large asynchronisation errors would cause a large systematic range error.

This implies that this system, despite using nonspecialised hardware, has the potential to outperform traditional pulsed one-way ranging systems by circumventing accuracy limitations imposed by clock asynchronisation.

4.3.3 Exposure Duration Uncertainty

There is also a nonzero uncertainty on the exposure duration, which directly affects the number of photons collected. This effect can be included in the model by modifying Equation 4.10 further:

$$N_B(s, t_0) = A_{col}\eta_{optics}\frac{hc}{\lambda}\int_{t_0}^{t_0+t_E} P_A\left(t - \frac{s}{c} - \Delta t_e\right)\frac{1}{A_b(s)}dt + N \tag{4.11}$$

where the new term $\Delta t_e = \mathcal{N}(0, \sigma_e)$ is a random change to the exposure duration, modelled by a normal distribution with standard deviation σ_e. Here we assume the exposure uncertainty is zero mean (no systematic error) and variable exposure-to-exposure.

The performance of the system was characterised by performing 100 simulations for varying values of σ_e. The results of this are shown in Figures 4.6-4.8. As can be seen, the addition of this additional uncertainty significantly degrades the performance of the range estimation, to the point of being the most likely limiting factor. A requirement may be set, then, that for this technique to be

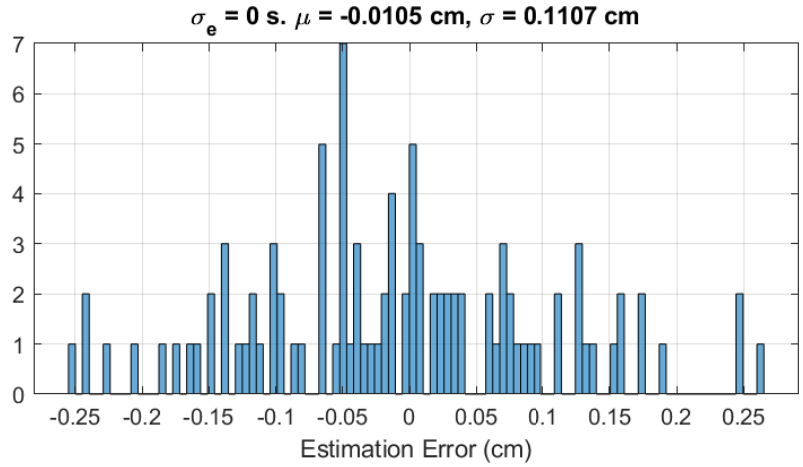

Figure 4.6: Range estimation performance at 1.5 km with $\Delta t_e = 0$ s.

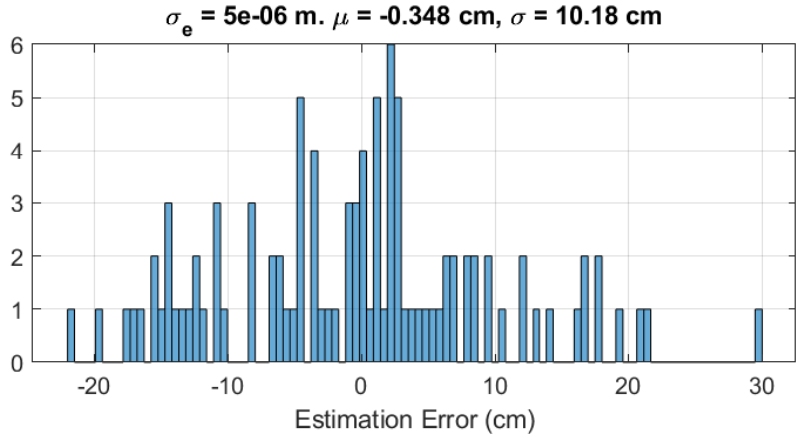

Figure 4.7: Range estimation performance at 1.5 km with $\Delta t_e = 5\text{x}10^{-6}$ s.

useful in practice, the exposure duration must have a low standard deviation, or at least be precisely measurable as the system is integrating, in order for this technique to yield highly accurate range data in a single sample. Since the mean remains near-zero, however, multiple observations may improve the estimation of the range beyond the single-sample performance.

4.4 Discussion

In this Chapter, a novel method of performing laser ranging between two stations (or satellites) was proposed and modelled. The technique exploits the randomness of a train of pulses along with knowledge of the time the train began to be transmitted to determine the distance to the emitter, using photon counts from

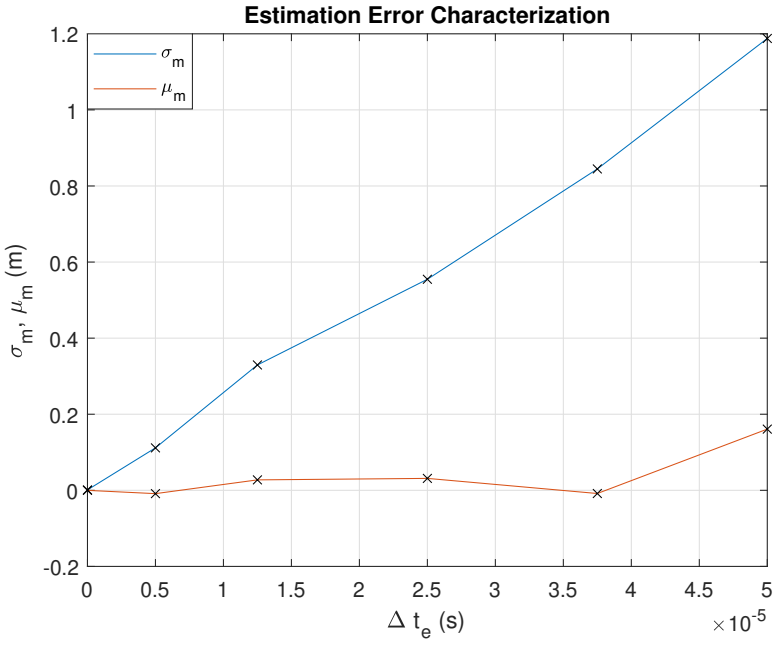

Figure 4.8: Mean and standard deviation of ranging error at 1.5 km as a function of Δt_e. 100 simulations were performed for each value of Δt_e.

the CCD sensor. It was found that this technique is not only theoretically capable of recovering range data to millimetre-level precision, but is also relatively insensitive to clock asynchronisation between the two satellites, which is a key limiting factor in standard time-of-flight pulsed laser ranging. It was shown that a key parameter affecting the attainable accuracy of this new technique is the stability of the exposure duration. Fluctuations in the length of the exposure resulted in larger single-measurement errors, although taking the mean of several consecutive measurements resulted in a more precise estimation of the true range.

Chapter 5

High-Fidelity Modelling of Momentum Transfer via Photon Pressure and Laser Ablation

Chapter 5 will present an impact assessment of a mission concept for the mitigation of space debris using lasers carried by satellites. In order to simulate this with as much accuracy as possible, a highly detailed model for the transfer of momentum using lasers was required. The details of this model shall be presented in this Chapter, along with comparisons between an often-used simplifying assumption and the results obtained using this higher-fidelity model.

The use of light to affect the orbits of space debris is not a new idea. Momentum transfer using laser illumination is a particularly attractive intervention strategy as it allows the piece of debris in question to be affected without the need for rendezvous maneuvers and the subsequent propellant expenditure, which effectively renders rendezvous-and-capture methods useless against large numbers of small fragments. A powerful enough ground-based or space-based laser could be used to apply a perturbative force to threatening objects in space as they pass through the operational range of the laser due to their relative velocity, even over multiple orbits or close approaches to compound the effect. However, before any such laser system could ever be deployed, the response of debris fragments' trajectories to laser illumination must be fully understood to ensure that the desired

outcome is brought about, and to ensure there is no risk of accidentally causing a collision rather than preventing one.

Relatively little work has been published regarding the use of lasers for debris remediation. The focus of this Chapter's literature review will be on those works pertaining to the modelling of the physics of the light-matter interaction processes and the resultant effect on the motion of debris objects, and the literature review in Chapter 5 will focus on previously proposed mission concepts.

Few publications have proposed detailed models to calculate the force on space objects due to ablation and/or photon pressure. Most previously proposed concepts (Yang et al., 2016; Mason et al., 2011; Bamann et al., 2020) have employed relatively high-level models for the imparted force on debris fragments by simply considering the area-to-mass ratio and effectively performing a shapeless areal integration over a flat surface, treating the debris fragment as a simple planar object with surface normal parallel with the beam propagation axis. Others (Peltoniemi et al., 2021) use a similar approach by considering only the *radiation pressure cross-section*, i.e. the area of the object projected onto the laser focal plane. All of these examples thus neglect all geometric effects of the objects being illuminated, including any off-axis components of the ΔV. Off-axis components are particularly important when considering ablative interactions, as the stronger forces compared with photon pressure may result in the object abruptly veering laterally with respect to the beam axis and being very difficult to track.

Liedahl et al. (2010) proposed an analytic model for calculating the ablative recoil velocity accounting for shape effects, which integrates a quantity they refer to as the *area matrix* over the surface of simple geometric shapes in 3D, yielding convenient analytic expressions for the recoil velocity vector. While this method does account for off-axis recoil components when the shapes are not perfectly aligned, it only works for simple shapes such as spheres and cylinders whose geometries can be easily integrated across analytically. These off-axis force components are important to model when considering multi-pulse interactions, as they may result in the object being kicked out of the beam radius. It is therefore important to understand the likely magnitude of the orthogonal $\Delta\mathbf{V}$ component

in order to design tracking capabilities appropriately. For many small space objects it is reasonable to assume that their shapes will not be precisely known *a priori*, and thus an approximation to one of these algebraically convenient proto-shapes is a good-enough approximation. However, for larger objects such as small satellites or even upper stages, the shapes of these bodies will likely be known with a high level of accuracy in advance of any intervention. Additionally, it is likely that any proof-of-concept of orbit lowering by laser ablation would be performed on such a well-understood target as a first step, and so there is a clear need for more precise, numerical models which will allow the response to ablation to be more accurately calculated for arbitrary geometries.

To the best of the author's knowledge, no previously published research has used a high-fidelity numerical model to capture the geometric effects of specific shapes on the net force vectors from laser pressure and ablation. The applications of such a model extend beyond the case of affecting the velocity of small fragments for collision avoidance or orbit lowering, and could also be applied to, for example, investigating the possibility of detumbling larger uncontrolled objects in LEO before they are able to be removed with other methods such as harpoons. To this end, a general model was developed to allow the accurate calculation of photon pressure and laser ablation forces. The model fully accounts for arbitrary object shape and self-shadowing. For the case of photon pressure, the model also fully captures the various components of light forces including off-axis forces. The model is also capable of calculating the effect of an illumination on the rotation state (orientation and angular velocity) of an object.

5.1 Modelling Illumination of Complex Geometries

The model works by integrating numerically across the surface of an arbitrary 3-dimensional shape, calculating small contributions to the net force and torque due to each surface element. The model takes as an input a triangulated 3D model of the object to be simulated, and optionally subdivides the surface elements to be-

low a given maximum element size before calculating each element's contribution according to the equations of either photon pressure or laser ablation. Additionally, the model propagates the rotational and, optionally, translational motion of the object, taking into account the effects of the laser on these motions. Thus the model fully accounts for the effects of tumbling objects in free space, which is the reality when considering space debris.

An example of one of the shapes used (a hex nut measuring 1.86cm from opposing vertices) can be seen in Figure 5.1. This was chosen to represent a typical fragment which may be produced in a collision, and one which is more complex than simple planar objects such as paint flecks or spheroids such as NaK droplets. The hex nut shape also presents some self-shadowing due to the inner hole.

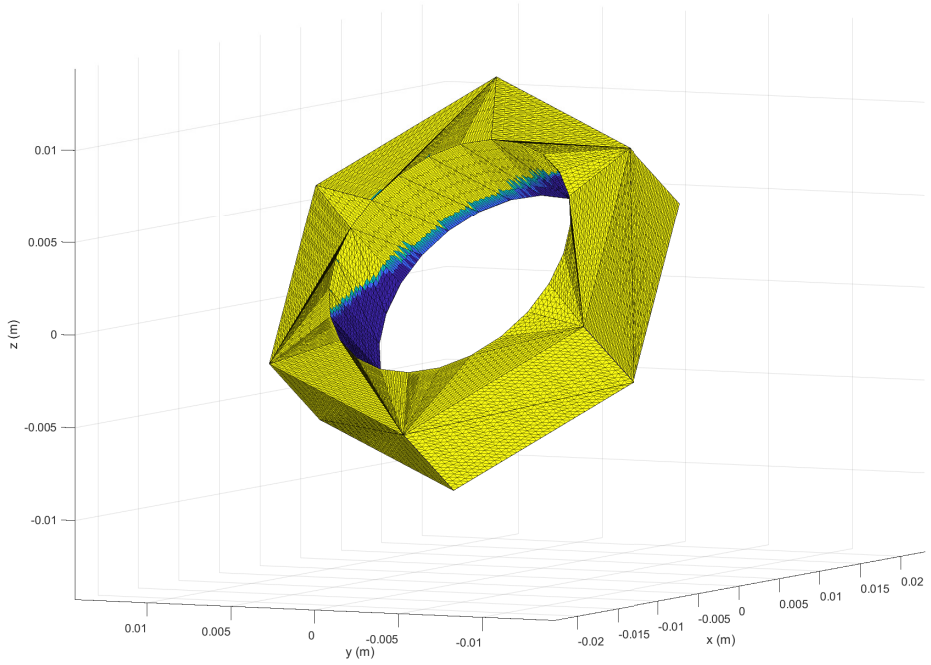

Figure 5.1: Tessellated 3D model of a hex nut, used to represent debris fragments. Colour represents illumination state, with dark blue being completely shadowed.

An overview of the model algorithm is presented in Algorithm 1.

Algorithm 1: Overview of laser force calculation algorithm.

Import 3D model of fragment;

Import dynamics of interaction to model;

Tessellate 3D model;

Set initial rotation state (rate, direction) of fragment;

for *All timesteps* t_i **do**

Retrieve incident light direction $\hat{\boldsymbol{i}}(t_i)$*;*

Calculate illumination state of all elements;

Calculate force and torque contribution from each element $\boldsymbol{F}_e, \boldsymbol{\tau}_e$*;*

Sum element contributions to obtain net force and torque;

Update rotation state;

Update position and velocity relative to reference frame (optional);

end

Calculate total momentum transferred over entire interaction;

To determine the illumination state of the elements, the model takes a time-dependent unit vector $\hat{\mathbf{i}}(t)$, representing the incidence direction of the laser. Illumination states between 0 and 1 are now assigned to each element in the triangulated mesh by determining which vertices in the point cloud have a direct line-of-sight to the laser source. This assumes that the laser spot is much larger than the object, as will be the case when illuminating space debris from large distances, so beam shape effects are not encoded in the model. However, these would be trivial to include in order to adapt the model to more precise applications such as detumbling, where the fluence varies significantly across different regions.

Katz et al. (2007) presented a fast algorithm for computer graphics applications which can determine the visibility of points in a point cloud from an arbitrary viewpoint, accounting for occlusion/self-shadowing and back-facing elements. Using this algorithm, a binary illumination state can be assigned to each vertex in the 3D model. Then, by checking how many vertices are illuminated for each triangular element, an illumination state for individual elements can be

calculated, taking on values between 0 and 1 in increments of $\frac{1}{3}$. Katz' algorithm is extremely fast and does not require manually searching for intersections between each element's centroid and all other elements in the model, thus it is ideal for this model as the illumination state must be re-checked at every timestep. However, it should be noted that it is not a full ray-tracing algorithm and only accounts for direct visibility, not secondary reflections.

After the calculation of each element's illumination state, the force on each element can be calculated using the relevant equations (detailed in Sections 5.1.1-5.1.2), as well as the torque, according to Equation 5.1.

$$\boldsymbol{\tau}_i = \mathbf{r}_i \times \mathbf{F}_i \tag{5.1}$$

From here all equations are in the body frame, i.e. r_i is in a frame whose axes are aligned with the object's principal axes of inertia and whose origin coincides with the object's centre of mass. Then, the total force and torque are summed across all elements to find the net force and net external torque, according to Equations 5.2 and 5.3.

$$\mathbf{F}_{net} = \sum_i \mathbf{F}_i \tag{5.2}$$

$$\boldsymbol{\tau}_{net} = \sum_i \boldsymbol{\tau}_i \tag{5.3}$$

The net external torque is then used to calculate the instantaneous rate of change of the angular velocity in the body frame according to Euler's equations of rigid body dynamics (Avanzini, 2008):

$$I_1\dot{\omega}_1 + (I_3 - I_2)\omega_2\omega_3 = \tau_1 \tag{5.4}$$

$$I_2\dot{\omega}_2 + (I_1 - I_3)\omega_3\omega_1 = \tau_2 \tag{5.5}$$

$$I_3\dot{\omega}_3 + (I_2 - I_1)\omega_1\omega_2 = \tau_3 \tag{5.6}$$

where $I_{1,2,3}$ are the diagonal elements of the fragment's inertia tensor in the body

frame, and $\omega_{1,2,3}$ are the components of the instantaneous angular velocity in the body frame. Representing the rotation state of the object using a quaternion $\mathbf{q}(t)$, the rate of change of $\mathbf{q}(t)$ is calculated from the instantaneous angular velocity in the body frame according to Equation 5.7 (Avanzini, 2008):

$$\dot{\mathbf{q}}(t) = \begin{bmatrix} \dot{q}_1 \\ \dot{q}_2 \\ \dot{q}_3 \\ \dot{q}_4 \end{bmatrix} = \frac{1}{2} \begin{bmatrix} 0 & -\omega_x & -\omega_y & -\omega_z \\ \omega_x & 0 & \omega_z & -\omega_y \\ \omega_y & -\omega_z & 0 & \omega_x \\ \omega_z & \omega_y & -\omega_x & 0 \end{bmatrix} \begin{bmatrix} q_1 \\ q_2 \\ q_3 \\ q_4 \end{bmatrix} \tag{5.7}$$

Together, Equations 5.4-5.7 allow the propagation in time of the angular velocity and the rotation state $\mathbf{q}(t)$ accounting for the net external torque due to the laser fluence τ. By propagating from one time step to another, at each time step recalculating τ for updated rotation state and illumination condition, the net effect of the interaction can be integrated over some finite interaction period.

5.1.1 Photon Pressure Force Model

For a flat, specularly reflecting surface, the reaction force due to photon pressure can be calculated as follows. Force is defined as the rate of change of momentum:

$$\mathbf{F}_{rp} = \frac{d\mathbf{p}}{dt} \tag{5.8}$$

where $\mathbf{F}_{rp}$ is the radiation pressure force. A photon's momentum is

$$p_{ph} = \frac{E_{ph}}{c} \tag{5.9}$$

where E_{ph} is the photon energy, and c is the speed of light in the medium - in this case, a vacuum. For light reflecting off a surface in the incident direction, an additional factor of 2 mush be included to account for the light leaving in the same direction it came from. Thus for this idealised case, the magnitude of the radiation pressure force (directed into the surface) can be written as

$$F_{rp} = \frac{2P_{inc}}{c} \tag{5.10}$$

where P_{inc} is the total light power incident on the surface. This is the best-case scenario, with purely specular reflection, the outgoing rays perfectly aligned with the incoming light, and 100% reflectivity. In reality, this optimal case is unachievable. The incoming light momentum leaves the surface by three mechanisms: diffuse reflection, specular reflection, and absorption, which all impart a portion of the incoming momentum in different directions (illustrated in Figure 5.2). There is also the thermal emission of electromagnetic radiation by the object itself, however, at the temperatures of typical space objects (several hundred Kelvin), this will contribute a negligible force in comparison to the photon pressure reaction forces.

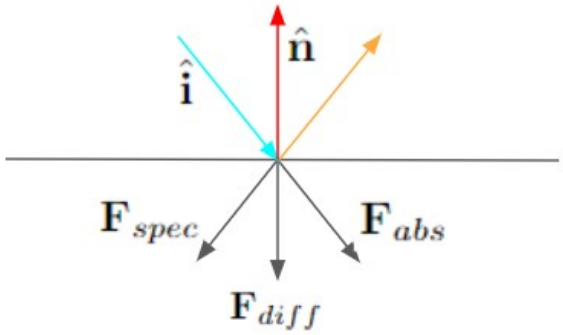

Figure 5.2: Illustration of the components of photon pressure recoil force. $\hat{\mathbf{n}}$ is the local surface normal vector and $\hat{\mathbf{i}}$ is the direction of incident light.

To account for this decomposition, Equation 5.10 is replaced with the vector equation:

$$\boldsymbol{F}_{rp} = \boldsymbol{F}_{spec} + \boldsymbol{F}_{diffuse} + \boldsymbol{F}_{abs} \tag{5.11}$$

Each component of Equation 5.11 will now be derived. Firstly, an albedo term α must be included to account for the reflectivity of the surface being less than 1, which determines the fraction of incoming light that is absorbed.

The specular component, $\boldsymbol{F}_{spec}$, acts in the opposite direction to that of the specularly reflected rays, and its magnitude is simply

$$\boldsymbol{F}_{spec} = -\alpha S \frac{P_{inc}}{c} \hat{\boldsymbol{r}} \tag{5.12}$$

where α is the albedo or reflectivity of the surface material, S is a factor that determines the fraction of total reflected light which is reflected specularly, and $\hat{\boldsymbol{r}}$ is the unit vector in the direction of the specularly reflected rays. $\hat{\boldsymbol{r}}$ is calculated using the vector form of the law of reflection.

The diffuse component, $\boldsymbol{F}_{diffuse}$, must be calculated by integrating the diffusely reflected component of light across a hemisphere. Diffuse reflection follows Lambert's cosine law, whereby the intensity of light reflected in any direction $\hat{\mathbf{r}}$ from the surface depends only on the polar angle ϕ between $\hat{\mathbf{r}}$ and the local mean normal $\hat{\mathbf{n}}$. This is written in vector form in Equation 5.13

$$\mathbf{I}(\phi) = I_0 \cos\phi \hat{\mathbf{r}} \tag{5.13}$$

where ϕ is the angle between the direction of interest and the local mean surface normal. To obtain I_0, one must integrate Equation 5.13 over a hemisphere. Due to conservation of energy, the total diffusely reflected light power over the hemisphere must be

$$P_{t,d} = \alpha(1 - S)P_{inc} \tag{5.14}$$

Performing the hemispherical integration, one obtains the following expression for I_0:

$$I_0 = \frac{\alpha(1 - S)P_{inc}}{\pi} \tag{5.15}$$

In order to obtain the net force due to the diffuse component, any components perpendicular to the local normal may be neglected, since the reflection is axisymmetric. Thus, the total reflected power which contributes to the recoil force can be obtained integrating the dot product of the local normal with the reflection over a hemisphere in spherical coordinates:

$$P_{diffuse} = \int_0^{2\pi} \int_0^{\frac{\pi}{2}} \hat{\boldsymbol{n}} \cdot \boldsymbol{I}(\phi) \sin\phi d\phi d\theta \tag{5.16}$$

Substituting Equation 5.13 and replacing $\hat{\boldsymbol{n}} \cdot \hat{\boldsymbol{r}} = \cos\phi$:

$$P_{diffuse} = I_0 \int_0^{2\pi} \int_0^{\frac{\pi}{2}} \cos^2\phi \sin\phi d\phi d\theta \tag{5.17}$$

Integrating by substitution, and substituting the previous expression for I_0 (Equation 5.15):

$$P_{diffuse} = \frac{2}{3}\alpha(1-S)P_{inc} \tag{5.18}$$

Thus, from Equations 5.8, 5.9, and 5.18, the total force due to the diffusely reflected component of light is

$$\boldsymbol{F}_{diffuse} = -\frac{2\alpha(1-S)P_{inc}}{3c}\hat{\boldsymbol{n}} \tag{5.19}$$

which acts in the $-\hat{\boldsymbol{n}}$ direction, since all orthogonal components cancel.

Finally, the force component due to the absorbed fraction of light must be calculated. This component is in the direction of the incoming light $\hat{\boldsymbol{i}}$, and can be simply calculated by considering conservation of momentum regarding the absorbed fraction of light:

$$\boldsymbol{F}_{abs} = \frac{P_{inc}}{c}\hat{\boldsymbol{i}} \tag{5.20}$$

Substituting Equations 5.12, 5.19 and 5.20 into Equation 5.11 gives the total recoil force due to photon pressure on a finite, flat surface element:

$$\boldsymbol{F}_e = -\frac{\alpha S P_e}{c}\hat{\boldsymbol{r}}_e - \frac{2\alpha(1-S)P_e}{3c}\hat{\boldsymbol{n}}_e + \frac{P_e}{c}\hat{\boldsymbol{i}}_e \tag{5.21}$$

$$\boldsymbol{F}_e = \frac{\alpha P_e}{c}\left(-S\hat{\boldsymbol{r}}_e - \frac{2}{3}(1-S)\hat{\boldsymbol{n}}_e + \frac{1}{\alpha}\hat{\boldsymbol{i}}\right) \tag{5.22}$$

where $P_e = \Phi A_e(\hat{\boldsymbol{n}} \cdot -\hat{\boldsymbol{i}})$ is the total power incident on element e of area A_e, and Φ is the irradiance of the illumination. $\hat{\mathbf{n}}_e$ and $\hat{\mathbf{r}}_e$ are the local normal and specular reflection directions for surface element e.

This more complete description of the photon pressure reaction forces can now be used to compare with naive assumptions of the reaction force being parallel

with either $-\hat{\mathbf{n}}_e$ or $\hat{\mathbf{i}}$. Figures 5.3-5.4 show the angular deviation of $\mathbf{F}_e$ from these two vectors respectively, as functions of α and S, for an incidence angle of 45 degrees. Clearly, for most combinations of α and S, the assumption that the recoil force is parallel to either $-\hat{\mathbf{n}}$ or $\hat{\mathbf{i}}$ is locally highly inaccurate, demonstrating the need for higher-fidelity models such as this.

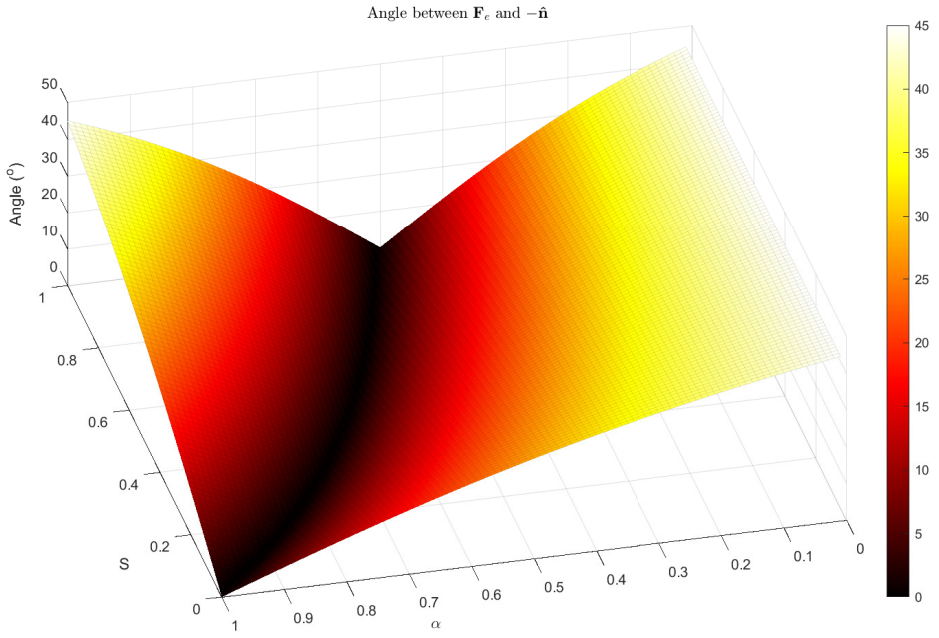

Figure 5.3: Deviation of $\mathbf{F}_e$ from $-\hat{\mathbf{n}}$ w.r.t. α, S .

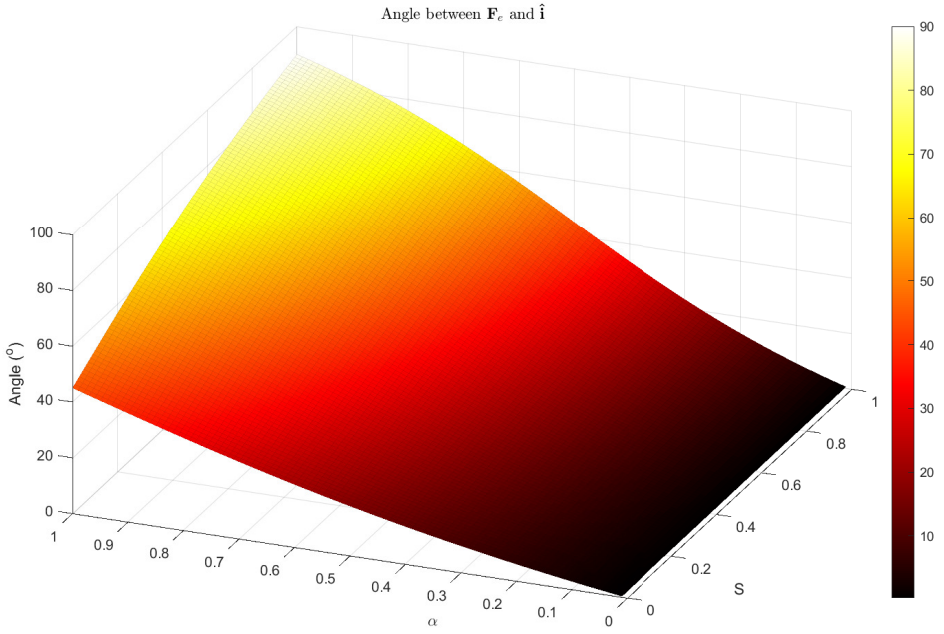

Figure 5.4: Deviation of $\mathbf{F}_e$ from $\hat{\mathbf{i}}$ w.r.t. α, S .

However, considering only single surface elements does not show the net effect over the whole object when geometry is also considered. Monte Carlo simulations were performed using random orientations of the hex nut in Figure 5.1, to investigate how significant the deviation from the assumption of parallelism with $\hat{\mathbf{i}}$ is. Figure 5.5 shows the results for $\alpha = 0.8$ and $S = 0.3$, chosen to approximate brushed aluminium. It can be seen that rather large deviations remain, indicating that the geometry of the object has reduced the effect compared with the single element case, but the deviation of the net force over the entire object is significant.

Using different combinations of α and S, different results can be seen however. When α is low, the absorption term dominates, and the deviation from $\hat{\mathbf{i}}$ reduces. Figure 5.6 shows the same results for the case of $\alpha = 0.2$ and $S = 0.1$, chosen to approximate a rough, black painted object. For this type of object, the simplified assumption of the direction of $\mathbf{F}_{net}$ is likely a sufficiently accurate approximation of reality.

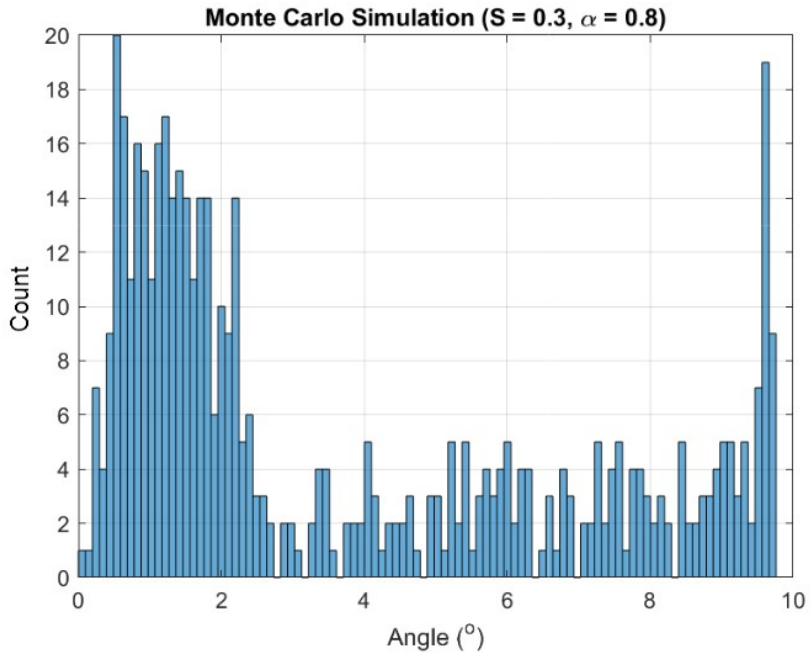

Figure 5.5: Angular deviation of $\mathbf{F}_{net}$ from $\hat{\mathbf{i}}$ for $\alpha = 0.8$, $S = 0.3$.

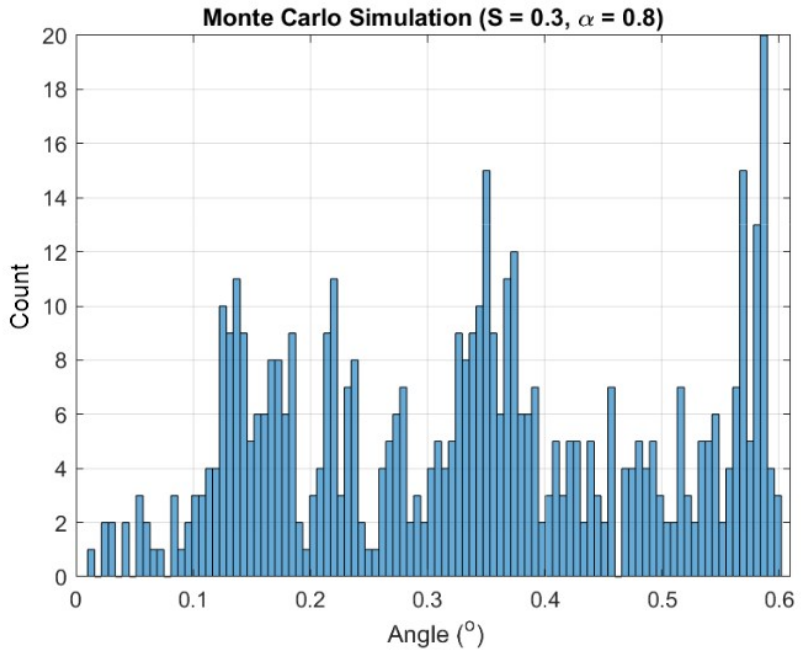

Figure 5.6: Angular deviation of $\mathbf{F}_{net}$ from $\hat{\mathbf{i}}$ for $\alpha = 0.2$, $S = 0.1$.

5.1.2 Laser Ablation Force Model

While the interaction of intense laser pulses with solids is relevant to many applications such as 3D printing, laser welding, laser induced breakdown spectroscopy and others, there are very few applications where the transfer of momentum is relevant. Attempts to better understand the transfer of momentum via laser ablation have only been motivated by applications in debris removal and high specific impulse microthrusters for space applications, so the body of literature available to draw from is rather limited, data is sparse and some inconsistencies between different publications appear. In this section the available literature will be reviewed and used to inform the development of the ablation force model.

The mechanism of momentum transfer by laser ablation will now be described. As the laser fluence incident on a surface increases, at some point the energy density becomes high enough to vapourise small amounts of surface material. The resultant gas plume expands into the gas or vacuum surrounding the surface. When the laser spot is small compared with the size of the object, observations show that the resulting gases leave the surface with a bias towards the normal direction rather than expanding isotropically in all directions (Amoruso et al., 2007; Sallé et al., 1999). This expanding plume of gas exerts a reaction force on the ablated surface, imparting momentum. The efficiency of the momentum transfer is characterised by a momentum coupling coefficient, with units of Newton seconds per Joule. The value of the momentum coupling coefficient is a function of the material, laser wavelength and pulse duration.

Upon further increasing fluence beyond the ablation threshold, the momentum coupling coefficient increases, until the onset of ionisation of the plume by incoming pulses shields the surface due to absorption in the resulting plasma (Phipps et al., 2004; Brandi et al., 2010). Hence, an optimum fluence Φ_{opt} exists, just before the onset of plasma generation and shielding. The decay due to plasma shielding with increasing fluence has been observed to be less rapid than the increase with fluence on the other side of the peak (Phipps et al., 2004), however the slope on both sides of the maximum is rather steep. In an ideal situation, the material and geometry of an ablation target would be well understood in order to

accurately target this optimum surface fluence, although in space applications, likely dealing with uncooperative targets, this may be difficult. It is therefore important to include this effect in any modelling efforts in order to capture the near-certain deviation from the optimally-coupling scenario.

It has been shown that laser incidence angle plays a significant role in the momentum coupling coefficient even when correcting for decreased surface fluence with oblique incidence (Wang, 2017; Zhao et al., 2016). This is because of the shape of the ablation plume - it has been observed experimentally that even at 45 degrees incidence, the ablation plume remains centered around the surface normal for flat metal surfaces (Amoruso et al., 2007). Thus, an incoming beam closer to parallel with $\hat{\boldsymbol{n}}$ will have to traverse a greater depth of plume and will be absorbed more strongly. This effect is stronger for higher fluence, when there is more ejected material and, at even higher fluence, plasma. However, these studies like most other papers on laser ablation were done with a small, tightly focused spot on the surface of a plate. From the plume shape, it is obvious that while this dependence on incidence angle should hold for $d_{spot} << d_{target}$, when this is reversed this may not be the case. For a relatively small target, especially a tiny surface element of such a target, it is reasonable that the entire surface will have a thin layer of gas or plasma instantaneously covering it, which would not lead to a strong dependence of plume depth traversal on incidence angle. For this reason, dependence of C_m on incidence angle due to different amounts of plume traversal is not included in the model, however the effect of the incidence angle on reducing the fluence will be accounted for.

In the scenario of ablating distant, small objects with a laser beam, it is unlikely that the pointing stability and knowledge of relative position would be precise enough to keep the spot on-target when $d_{spot} << d_{target}$. Besides, the large range and variable, unknown distance to the target preclude precise focussing of the beam. Thus laser ablation for space debris remediation should employ a very wide beam to ensure the target remains within the beam, and fluence must be raised to compensate for the larger size to ensure the ablation threshold is met. A wide beam with sufficient fluence to ablate metal at hundreds of kilometres

presents significant risks to most satellites operating in a similar orbital altitude, and so the orbits of nearby satellites should be considered when determining whether or not to engage a target. Additionally, targets should not be engaged when the line of sight intersects with Earth's surface to protect people and infrastructure below. Considering all the information above taken from the reviewed literature, it is justified to construct the model for ablation in a similar fashion to the photon pressure model, with a force contribution from each element parallel with the local normal.

Since ablation efficiency rises with decreasing pulse duration (i.e. increasing fluence at the same pulse energy) and most ablation research is focused in the picosecond to femtosecond regime, momentum transfer per pulse is modelled as an instantaneous impulse. The impulse vector from a single pulse, due to ablation occurring over a given surface element e is calculated according to Equation 5.23.

$$\Delta \boldsymbol{p}_e = -A_e \Phi_e C_m(\Phi_e) \hat{\boldsymbol{n}}_{\boldsymbol{e}} \tag{5.23}$$

where A_e is the area of the element, $C_m(\Phi_e)$ is the momentum coupling coefficient for the material comprising element e as a function of Φ_e. Φ_e is the local fluence in Jm^{-2} on element e. This can be calculated according to

$$\Phi_e = \max(0, -\hat{\boldsymbol{i}} \cdot \hat{\boldsymbol{n}}_{\boldsymbol{e}} \frac{E_p}{A_{beam}(z)}) \tag{5.24}$$

where E_p is the pulse energy and $A_{beam}(z)$ is the area of the beam at distance z from the emitter. The max term sets the impulse to zero for all elements where the angle between $-\hat{\mathbf{i}}$ and $\hat{\mathbf{n}}_e$ is greater than 90 degrees. For an approximately Gaussian beam profile, the beam diameter at some distance z from the emitter along the propagation axis can be expressed as

$$w(z) = w_0 + (\sqrt{z - z_0})^2 \tan(\theta_d) \tag{5.25}$$

where w_0 is the spot radius, and the focal plane is located at $z = z_0$ and θ_d is the divergence half-angle of the beam. The beam area can then be calculated trivially.

Author (Year)	$C_{m,opt}$ (μNsJ^{-1})	Φ_{opt} (Jcm^{-2})	τ_{pulse}	Pred. Φ_{opt}
Phipps et al. (2004)	18	1.17	130 fs	0.017
Phipps et al. (2017)	28	3	80 ps	0.429
Wang (2017)	14.25	10	6 ns	3.718
Tran et al. (2017)	25	19	5 ns	3.394

Table 5.1: Literature values for optimum fluence and optimum momentum coupling for aluminium.

In order to develop as complete a model as possible, the dependence of C_m on the local fluence must be included - i.e. C_m becomes $C_m(\Phi)$. The dependency of C_m on Φ for metal targets in vacuum has been investigated previously. Wang (2017) noted that the region near to the maximum of C_m could be approximated using a 4th-order polynomial, the coefficients of which are noted in said work. An empirical relation for the optimum fluence (Φ_{opt}) (at which the highest momentum coupling coefficient $C_{m,opt}$ occurs) was identified by Phipps (Phipps and Luke, 2002; Phipps et al., 2004) that when the pulse duration is greater than 100 ps, the optimum fluence can be approximated Equation 5.26, although the fit of this empirical relation with lab data is rather loose as can be seen in their paper.

$$\Phi_{opt} = B\sqrt{\tau} \tag{5.26}$$

with $B = 480$ MJm^{-2}.

Very few sources are available in the literature for experimental measurements of $C_{m,opt}$ and Φ_{opt} for aluminium targets in vacuum or low-pressure environments. These are summarised in Table 5.1, with the final column showing the value of Φ_{opt} that is predicted from the pulse duration by Equation 5.26. In the work of Tran, only three discrete fluence values were measured. The authors note that the best tested fluence was the closest one to model prediction of $\Phi_{opt} = 34$ Jcm^{-2}. In addition to this, Battocchio et al. (2020) measured C_m for aluminium in a low pressure environment but did not attempt to measure Φ_{opt}. They observed a value of $C_m = 20$ μNsJ^{-1} at a laser fluence of 70 Jcm^{-2}.

The experimental results in the literature for nanosecond pulses correspond reasonably well - on the same order of magnitude - with Phipps' empirical formula as can be seen from Table 5.1. The experimental values of Φ_{opt} in the nanosecond

regime from Wang and Tran are factors of 5.6 and 2.7 times higher than their predicted values respectively, however the empirical forumla gives a reasonable approximation.

To model the momentum coupling as accurately as possible, the dependence $C_m(\Phi_{inc})$ was implement ed using the polynomial coefficients of Wang, with the addition of small shifts of the curve such that the peak occurs at $\Phi_{opt} = 14.5$ Jcm^{-2} and $C_m = 19.6\mu$NsJ^{-1}, which are the average of the available experimental data for nanosecond pulses ablating aluminium. The nanosecond regime was chosen due to the difficulty in achieving extremely short pulses in a compact system suitable for space applications. The resulting curve can be seen in Figure 5.7. Since this is only an empirical formula valid over a limited range of Φ, it may return negative values, and so the value of C_m in the model is additionally constrained to be greater than or equal to zero. This approach is the most significant source of uncertainty in the model developed, as the accuracy of calculating C_m is currently quite limited by the lack of extensive research in the area. This could be improved with more research and data on the momentum coupling coefficient for various materials, with the most likely best solution in the near future being an empirical formula for C_m for each of a set of common space materials as a function of pulse duration, energy, wavelength and fluence.

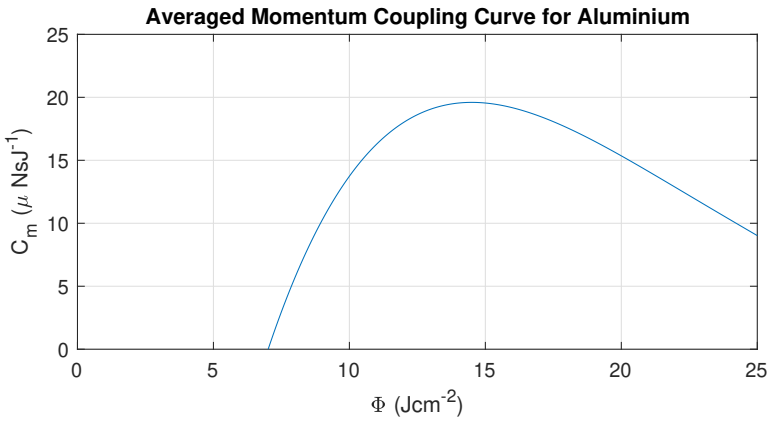

Figure 5.7: Momentum coupling curve used in the ablation impulse transfer model obtained from averaged literature nanosecond pulse results.

Thus, for a given pulse, the net change in velocity of the fragment is calculated by simply performing a vector sum of the contribution from all surface elements

(Equation 5.27) and dividing by the mass of the object (assuming the fragment is composed entirely of aluminium, and taking the interior volume of the 3D model).

$$\Delta \boldsymbol{v} = -\frac{1}{m_{frag}} \sum_{e} A_e \Phi_e C_m(\Phi_e) \hat{\boldsymbol{n}}_{\boldsymbol{e}} \tag{5.27}$$

Chapter 6

Space Debris Remediation using Space-Borne Lasers

Ever since the first orbital spacecraft, Sputnik 1, human activities in space have led to ever-increasing amounts of debris in Earth orbit. The debris population is very diverse, ranging from paint flecks and small pieces of solid rocket motor slag, all the way to entire spent stages and defunct satellites. In addition, there are also satellite fragments produced by collision and breakup events such as the 2009 Iridium-Kosmos collision. Due to the thin atmosphere at higher altitudes, the effect of atmospheric drag is small, and these fragments can remain in orbit for decades or even centuries.

According to the European Space Agency website, as of April 28 2022, there are approximately 31050 pieces of space debris actively being tracked by space surveillance networks worldwide. In addition to this, statistical models predict a vast additional untracked population of 1,000,000 fragments between 1 and 10 cm, and 130 million fragments between 1 mm and 1 cm. This number grows every year as more satellites are launched into orbit (between beginning and completing this thesis, the number of tracked fragments increased by approximately 10%). Even these small fragments pose a considerable risk - depending on the orbits of the bodies involved, relative velocities in a collision could be well over 10 kms^{-1}. At such speeds, even small fragments can impart more energy than a bullet on Earth. Due to the difficulty of tracking very small objects (both finding

them and accurately predicting their orbits) combined with their high damage potential, these may be considered one of the most dangerous classes of space debris.

Satellites and satellite technology are only becoming more vital to modern life, and with the advent of reusable launch vehicles allowing mass to orbit costs to decrease, space will become rapidly more accessible and be exploited by more commercial and research organisations as time goes on. This rapid expansion of launch activity brings serious concerns about debris production and the possibility of collisions. Kessler syndrome (Kessler et al., 2010) describes a cascading series of collisions, leading to an extremely rapid and self-sustaining increase in small fragments: large debris are hit and break up, creating thousands of smaller fragments, which then collide with other objects, creating further debris and so on. This could feasibly render entire orbital bands too dangerous to use, and in the extreme case, could block our access to space entirely until the shell decays naturally, unless human intervention reduces the debris lifespan.

Satellite breakup events are not just a hypothetical future risk - there have been several in recent years. Perhaps the most notable of these was the collision between Kosmos 2251 and Iridium 33 on February 10th 2009 (Kelso et al., 2009), where the defunct Kosmos 2251 collided with the active Iridium 33. In addition to this, other notable debris source events include the 2007 anti-satellite missile test by China, where their Fengyun 1C satellite was intentionally destroyed, and a similar test in 2019 by India (although this test was performed at low altitude to minimise debris lifetime). Although anti-satellite missile tests and uses could be banned or otherwise discouraged by sanctions, the Iridium-Kosmos collision shows the very real risk of non-military satellite breakup, even when active control over one body is available.

Numerous strategies have been proposed to help mitigate the threat of debris and lower the likelihood of the onset of Kessler syndrome. The majority of proposed strategies aim to remove larger pieces or defunct and out-of-control satellites - which represent future sources of debris should another fragment hit them.

Many proposed debris removal approaches involve mechanical manipulation of defunct satellites by a second satellite which must rendezvous and match orbits with the targeted piece of debris. RemoveDEBRIS (Forshaw et al., 2016) was a British satellite deployed from the ISS in 2018 with the goal of testing several mitigation strategies on dummy targets. Two CubeSats deployed from the main craft which simulated defunct satellites to be removed. RemoveDEBRIS demonstrated the capture of one CubeSat with a net, which could then be used to drag the captured satellite into a lower disposal orbit using thrusters. It also successfully demonstrated the use of a harpoon to attach to the other CubeSat, which could then be towed similarly. Finally, it demonstrated a dragsail - a passive device which could be deployed at a satellite's end of operational life to increase drag and reduce its orbital lifetime.

Another proposed strategy to mitigate debris production by removal of defunct satellites is the use of electrodynamic tethers, which induce a deceleration on the satellite by interacting with Earth's magnetic field (Sanmartín et al., 2015).

Another class of strategies target smaller fragments, which represent the main direct threat to spacecraft, with the objective of collision avoidance. Here, a potential collision is identified, and the fragment is slightly nudged by some artificial force to change its orbit. This small change in velocity compounds over time to a large enough separation at the point of orbit intersection to reduce collision probability to acceptable levels. In the past, this has primarily been proposed with photon pressure in mind as the perturbing force, usually from laser illumination. There have been strategies of this class proposed which do not involve laser induced photon pressure, one being the deployment of powder clouds on a sub-orbital trajectory which intersects the target orbit to induce drag on debris fragments (Bonnal et al., 2019).

Laser interaction with debris has been proposed in several different concepts for space debris mitigation by collision avoidance. Many proposed concepts involve Earth-based laser systems, which illuminate debris as it passes overhead. Most concepts are similar and relatively simple - employing high-power CW lasers at various ground stations to impart a small force on the fragment in question.

One such proposal utilised a 5kW ground-based laser to interact with fragments via photon pressure multiple times, finding in simulation results that it is possible to achieve kilometre-level displacements from unperturbed trajectories with multiple passes over 48 hours (Mason et al., 2011). LightForce (Yang et al., 2016) is a similar concept utilising photon pressure from three geographically separated 20 kW lasers with a 1.5 m diameter aperture. In the LightForce paper, the efficacy of the strategy was analyzed by propagating the orbits of the entire catalogued LEO population (both debris and active satellites) for one year, and identifying potential collision events. Orbits were then re-propagated including perturbations from the LightForce laser targeted at fragments which were on a collision course. It was found that a system such as this could prevent up to 85% of the potential collisions in this timeframe.

As well as photon pressure, laser ablation is an alternative interaction mechanism that facilitates impulse coupling via light, as discussed in the previous Chapter. In ablation, pulsed laser light of sufficient intensity is applied such that a small amount of surface material is vapourised. This material then rapidly expands in a plume, exerting a reaction force on the fragment. This mechanism has a momentum coupling coefficient up to 4 orders of magnitude larger than photon pressure, if optimum surface fluence can be achieved. Impulse coupling via laser ablation has been studied experimentally for several decades, with the primary motivation often being applications in high specific impulse thrusters using metallic or energetic polymer fuels, however it has attracted some attention for application in space debris mitigation.

Project ORION (Phipps et al., 1996; Campbell, 1996) proposed in 1996 the use of laser ablation to re-enter debris fragments. In this case, the chosen laser parameters were 530 nm wavelength (frequency doubled Nd:YAG), with a 6 m launch aperture diameter, with the laser focal plane located at a fixed 1400m from the source. At the focal plane, the spot diameter is 40 cm. The laser here has a pulse energy of 20 kJ and a repetition rate of 1 Hz. The authors performed a detailed study of their concept, including analysis on the tracking of fragments, and detailed modelling of the effect of atmospheric extinction at

the laser wavelength. They estimated that the system could completely clear low Earth orbit (altitudes below 1000 km) of small debris fragments within 4 years of operation. It should be noted however that the ORION concept was developed in the mid-90s when the debris population, both known and unknown, was significantly smaller than today.

A key requirement for ground-based approaches is the need for the fragment to be visible and trackable from ground, since multiple passes requires reasonably accurate orbit prediction, and aiming requires accurate tracking. Atmospheric aberration is unavoidable in these scenarios and limits the ability to observe faint objects. Thus ground-based approaches are better suited for larger objects - for example, this could be useful if a collision between two larger fragments is predicted, to prevent the creation of a large cloud of smaller fragments.

Ground-based systems do suffer from some unavoidable disadvantages, however. Firstly, due to non-zero laser divergence, the large distance to the target object significantly disperses the laser energy over a much larger area, delivering a smaller irradiance to the target. For example, a diffraction-limited 1064 nm laser-based system (0.5 m aperture) suffers an irradiance reduction at target of approximately 77% when operating at 1000 km compared with 100 km. This does not take into account atmospheric absorption, which further reduces the delivered irradiance depending on the depth of atmosphere traversed. In order to get good directionality of the applied force (force vector is close to the anti-velocity vector), the laser must be pointed at the object when it is close to the horizon. This not only increases the absolute distance to the target, worsening the effects of divergence, but also increases the depth of atmosphere traversed, further reducing delivered power, and makes the object fainter and harder to track. Additionally, these distance-related effects are more prevalent for fragments in higher orbits, which have longer lifetimes and are thus a more pressing target for removal efforts.

An idea to sidestep some of these limitations was proposed by Calabro and Perrot (2019), where the laser would be placed on top of a 20 km tall tower. However, since this is 24 times as tall as the Burj Khalifa, currently the tallest

artificial structure on Earth, or 2.25 times the height of Mount Everest, the feasibility of this approach is questionable at best, and placing the laser source onboard an orbiting satellite platform is likely a more realistic way to avoid the limitations of ground-based systems.

Up to this point, all discussed concepts have been ground-based, as far fewer concepts have been proposed which employ space-based lasers. One such concept that has been proposed is L'ADROIT (Phipps, 2014), which proposes a debris-cleaning satellite armed with a pulsed UV laser in an elliptical polar orbit (with apogee and perigee altitudes of 960 km and 560 km respectively) which imparts force by ablation. L'ADROIT uses a UV laser (frequency-quadrupled 1064 Nd:YAG source) due to the high atmospheric absorption reducing risk to people and assets on the ground, as well as requiring lesser fluence on the target to optimise thrust coupling, at the cost of significant losses in the frequency conversion process and greater system complexity. The chosen orbital regime allows the spacecraft to target debris at a variety of altitudes. The L'ADROIT spacecraft would use a passive optical sensor to continually scan the sky, searching for debris fragments in the 1-10 cm size range. Upon identification of a fragment, it would point and focus its laser on the target, either ablating a small amount of material (in the case of large objects), or completely vapourising the fragment (in the case of smaller objects). Analytical modelling in the paper showed that the strategy could be effective, however there are several questionable assumptions that may have led to more favourable results. The first of these is the assumption that all interactions occur head-on - that the laser is pointed directly in the fragments' anti-velocity direction, leading to optimised directionality of the applied force. Factors influencing the directionality of the applied impulse are collected into a single 'push efficiency' coefficient η_c, which is used to approximate the combination of shape effects and suboptimal pointing alignment with the anti-velocity direction. η_c is here set to the psychologically convenient value of 0.5, but no mention of how this value was chosen is made in the paper. Other optimising assumptions are the ability to firstly precisely determine the range to a given fragment, and secondly to rapidly and precisely focus the laser beam such

that the beam waist plane coincides with the fragment. Following this assumption, the authors then assume a constant, optimal momentum coupling coefficient throughout the course of a given interaction. Very little detail is provided about how such an extremely large (1.5 m aperture) beam could be rapidly and variably focussed, or the range of focal planes that could be available. These are very important details when it comes to optimising the thrust coupling coefficient, as the slope below the optimum fluence is extremely steep.

Another concept similar to L'ADROIT was recently proposed (**?**), again involving a single satellite in a polar orbit, but with higher-fidelity modelling of the change in velocity of the fragments, taking into account misalignment between the beam propagation axis and the negative velocity vector of the fragment.

From the published literature there is a clear bias toward ground-based systems when it comes to using lasers to affect space debris. At the time of the ORION concept proposal, the authors quoted a cost-to-orbit of $20,000/kg as a prohibitive factor in space-based laser systems. In the time since, this figure has dropped by almost a factor of 10 ($2,719/kg and $2,192/kg for a Falcon 9 with expendable and reused boosters respectively (SpaceX Falcon 9 Capabilities and Services)) with vehicles offering even cheaper mass-to-orbit currently in development. The fully reusable SpaceX Starship is being designed with a LEO payload of 100 - 150 tons, with launch cost estimates of less than $10 million. Using even pessimistic estimates of 50 tons to LEO at $20 million per launch, the cost of mass to LEO would be only $400/kg. These new developments in launch vehicle technology and their reduced cost to orbit bring the deployment of heavy space-based laser systems and large satellite constellations into the realm of feasibility.

Space-based systems offer numerous potential advantages to offset the mass and power restrictions which may make them viable options. These include no atmospheric extinction of the beam, and no atmospheric aberration affecting tracking of fragments. A shorter range to the target offers improved surface irradiance and thus reaction force, as well as improved optical observability, thus the possibility of being able to track and interact with smaller fragments than

would be possible from Earth.

The focus of this Chapter is the use of space-based laser systems for space debris remediation, with a focus on small fragments that may only be trackable with space-based optics. A new mission concept will be proposed and simulated in detail to ingestigate its efficacy, using the high-fidelity interaction models presented in Chapter 4 along with simulated encounter dynamics and realistic assumptions of laser-focusing capabilities to obtain a better representation of what may be possible with space-based systems considering their advantages and limitations.

6.1 A Mission Concept for Debris Mitigation using Space-Borne Lasers

As discussed in the introduction to this Chapter, fewer concepts have been proposed using space-based lasers to affect debris orbits than have been for ground-based concepts. The main reasons for this are the comparatively unlimited size, mass, and power consumption of ground-based devices of any type compared with their space-based counterparts. However, cheaper and more capable modern and near-future launch systems give more credence to the idea of using space-based systems, and as such their efficacy should be more thoroughly investigated. A novel mission concept will now be proposed which aims to use space-based lasers to affect the orbits of small space debris, and a detailed study of its potential for both de-orbiting and collision avoidance is presented.

6.1.1 Concept Overview

The proposed concept is as follows. The targeted population of debris is the sub 10 cm size range - those fragments which are numerous but often too small to be accurately tracked from Earth. A small constellation of satellites is inserted into a shell of inclined orbits around the Earth, with ascending nodes evenly spaced such that the shell covers all longitudes simultaneously. The target altitude would be chosen such that the satellites reside in an altitude band which is particularly

debris-dense, or close to the orbit of a high-value station such as the ISS. This may be as a direct response to a collision and breakup event - after some time, the clouds of fragments from such events have been observed to spread out over the course of months to several years into roughly uniform shells due to differential precession of their nodes because of orbital perturbations (Pardini and Anselmo, 2011), however their altitudes remain fairly tightly clustered.

Each satellite in the constellation is identical and carries two primary instruments: a camera for acquisition and tracking of debris fragments, and a high-power continuous-wave laser which is used to illuminate fragments and affect their orbits via photon pressure. No assumption is made of an ability to know the range to a fragment and/or quickly change the beam focal plane location to track the location of the fragment. Both photon pressure and ablation, respectively using CW and high-power pulsed lasers, will be studied for this mission concept.

Due to the high power consumption of the laser system combined with an expected low overall duty cycle, the laser would be powered by a battery bank onboard the spacecraft rather than directly feeding the laser with solar power. This battery bank would have sufficient capacity to power the laser for the duration of a typical interaction, and solar panels would be sized to recharge batteries fully in the typical inter-encounter time. This battery bank and solar array would also serve to power low-thrust electric propulsion for orbit maintenance or changing, as well as collision avoidance with tracked fragments in the cloud.

The camera onboard continually scans the sky behind the spacecraft, searching for fragments inside its field of view (FOV). Analysis of the visibility of fragments will be presented. When a fragment is found, the laser is steered onto the target fragment and tracks its movement across the sky. No prior knowledge of the fragments' orbits is assumed since small size objects are targeted, thus fragments are optically acquired and interacted with opportunistically, as they pass through the camera's FOV. An additional use of the camera is to reconstruct the orbits of the debris fragments that are encountered and build a more complete catalog of fragments that exist in the deployment altitude. However, this is not a require-

ment to interact using the laser (which requires only real-time optical tracking) and the additional use case for orbit determination and cataloguing will not be studied. Since this concept is aimed at smaller, untracked fragments, this data alone provides valuable information relating to collision risk and avoidance.

6.1.2 Methodology Overview

A high-level overview of the methodology of the mission impact assessment will now be presented in this section before going into further depth. In order to balance computation time with physical accuracy, taking into account the geometries of individual encounter trajectories, the impact of the mission is assessed using a quasi-statistical approach. This uses the output of a moderately large number of high-fidelity numerical simulations of individual encounters to form a sort of database. In the final mission simulation, the net effect of individual interactions in terms of the net momentum transfer vector can be quickly 'generated' by drawing a random entry from this database and scaling appropriately for the fragment's size, rather than needing to process every individual encounter with the laser interaction model. This enables a more rapid testing procedure for different numbers of satellites in the constellation, and different numbers of debris fragments in the population. Additionally, this inherently preserves and complex statistical relations between different parameters such as direction of the net impulse vector and the interaction duration, as there is no guarantee that these are statistically independent.

A population of 632 debris orbits is generated to represent the result of a collision event, with orbital elements generated statistically according to distributions based on those found in the tracked debris from the Iridium-Kosmos collision, as will be discussed in later sections.. A single satellite's orbit, centered in the shell, is propagated for a 10 year mission duration, along with the orbits of the debris population. The trajectories of the fragments and the satellite are analyzed to identify local minima in the separation magnitude. From these local minima, events which are not viable for interaction are filtered out by applying several criteria which aim to determine if the fragment is observable by the onboard

camera, since this is a prerequisite for steering the laser beam onto the target.

For the candidate events that pass this initial selection phase, the trajectories of the object and spacecraft during the interaction window are extracted and passed to a high-fidelity model of laser debris interaction (LDI), developed in the previous Chapter, which calculates the net impulse vector applied in that particular case. The distribution of times between consecutive events in this single-satellite propagation may also be extracted from the generated and processed data.

Finally, to simulate the actual mission, a new population of fragments is generated from the same distributions as those used to create the database, as well as the orbits of all satellites in the constellation. For each satellite, a series of timestamps are generated along with fragment IDs which determines the time at which that particular satellite encounters a fragment, and which fragment it encounters. This allows fragments to be individually propagated for the 10 year duration, with an impulsive ΔV being applied each time it encounters a satellite. Following this, the remaining lifetime of the perturbed and unperturbed fragment orbits are compared to assess the impact of the intervention on the population as a whole.

6.1.3 Altitude Effects on Debris Lifetime

For unperturbed objects in Earth orbit, the primary orbit-lowering effect is atmospheric drag. For this reason, lower orbits decay more quickly than higher orbits. Since the anticipated magnitude of the imparted ΔV is small for photon pressure, this concept should likely not target lower orbits which already decay relatively quickly as small changes in the orbits would not produce meaningful changes to the lifetime. An initial study on the effect of small impulsive ΔV applications on space debris fragments was conducted to inform the selection of an appropriate altitude range at which to target orbit-lowering intervention strategies.

Orbit propagations in this Chapter are performed using a tool developed at the University of Strathclyde (independently of the author) called CALYPSO. CALYPSO propagates orbits semi-analytically, enabling large numbers of propa-

gations to be performed relatively quickly. The tool allows various perturbations such as drag, the J_2 effect, lunar gravity, and others to be included. Since CALYPSO uses mean equinoctal elements, to recover the position of the satellite or fragments, conversions are required first into the mean Keplerian elements, then osculating Keplerian, and finally Cartesian state vectors. In this Chapter, all perturbations except drag (by far the most impactful for lifetime reduction) are disabled to reduce computation time to a manageable level, as the number of propagations required in later sections is extremely large.

Circular orbits of varying altitudes, inclined at 45 degrees were propagated until reentry (altitude < 300 km). An initial impulsive ΔV was applied in the negative velocity direction ranging from zero to 50 ms^{-1}. The effects on the lifetime of the debris can be seen in Figure 6.1. Here, an area-to-mass ratio (AMR) of 0.3391 m^2kg^{-1} is used, corresponding to that of the 3D model of the hexnut used in LDI modelling. This also coincides approximately with the peak of the distribution of the catalogued debris from the Iridium-Kosmos collision (Wang, 2010).

It can be seen that, for higher orbits, a given ΔV application results in a larger absolute lifetime reduction, as expected. For lower orbits, the reduction becomes less meaningful - for example for 700 km altitude, the expected lifetime is already under 10 years, and smaller ΔV interventions may only reduce a fragment's life by a couple of months at best. Whereas for a 1200 km orbit, smaller ΔV has a more significant impact, with an idealised 10 ms^{-1} ΔV reducing lifespan by over 10 years.

Although the effect of the same impulsive ΔV is larger for higher orbits, the risk posed by these fragments is also lower due to the reduced spatial density and collision risk given the same number of fragments. The reduced debris density is also an important consideration for this concept as it relies on opportunistic interactions, and if the debris is sparse then close approaches will be infrequent. Thus it is not attractive to target extremely high orbits; middling altitudes should be targeted instead.

Taking this into account, this concept and impact assessment will consider the

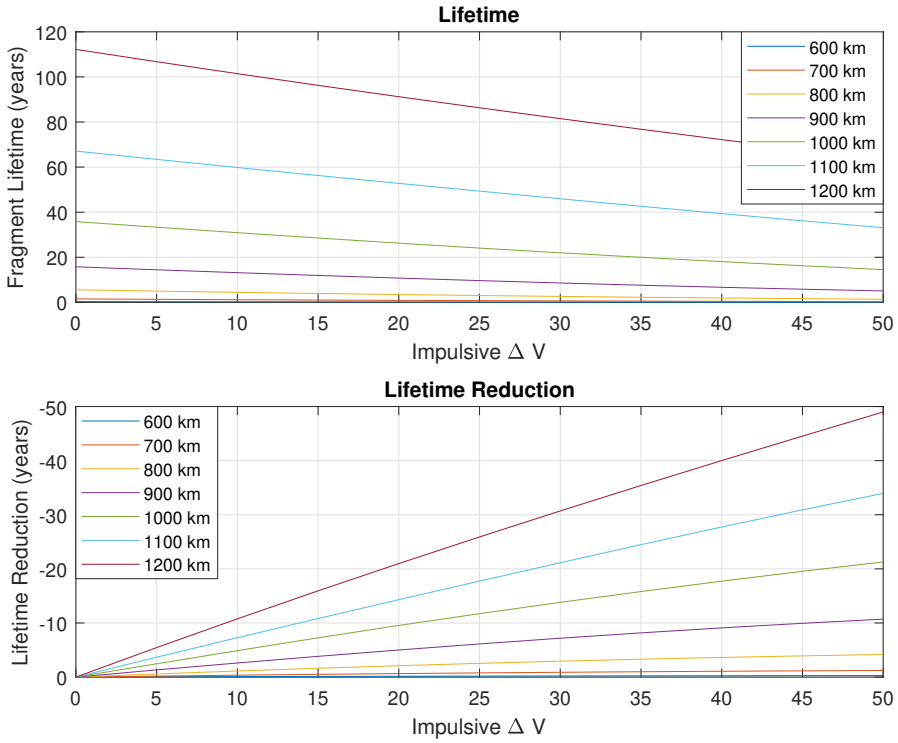

Figure 6.1: Lifetime and lifetime reduction with an impulsive ΔV for circular, 45 degree inclined orbits of varying altitude.

case of a debris shell centered around a moderate 1200 km altitude. This altitude is high enough that the natural lifetime of debris is on the order of a century, so natural de-orbiting is not a viable short-term solution, yet not so high that the collision risk is extremely low along with the encounter rate. This also reduces the developmental risk for the concept, as an expensive program targeting lower altitudes would likely be cancelled in favour of simply waiting for the debris to naturally deorbit no matter the density.

6.1.4 Debris Shell Generation

The first step in the impact assessment is generating a population of debris orbits which will be used to characterise typical interactions and later to assess the impact of the mission. TLE data for the tracked fragments from the 2009 Iridium-Kosmos collision (obtained November 2020 from the Celestrak website) was analyzed to identify distributions in the orbital elements of the fragments and how these compare with the pre-collision orbits of the satellites. These may then be used to formulate new distributions which are used to generate debris orbits with similar statistical properties, to simulate fragments that may be created as a result of a hypothetical future collision event.

The distributions of the orbital elements can be found in Figures 6.2 and 6.3. It was found that the semi-major axes and inclinations of the two debris clouds followed approximately normal distributions, close to the pre-collision values of their respective satellties. Inclination was very tightly clustered around the pre-collision values, with standard deviations of 0.051^o for the Iridium-33 cloud and 0.0326^o for the Kosmos-2251 cloud. Semi-major axes were found to have dissipated more with respect to the pre-collision value, with standard deviations of 76.4 km and 79.0 km, either due to the initial force of the breakup or differential decay in the years since. The eccentricity distributions were found to be well approximated by log-normal distributions, however no link was identified between the satellite eccentricity and the curve parameters. For Kosmos-2251, the right ascension of the ascending node Ω and mean anomaly M had both dispersed to a quasi-uniform distribution, indicating dispersion from a cloud into a

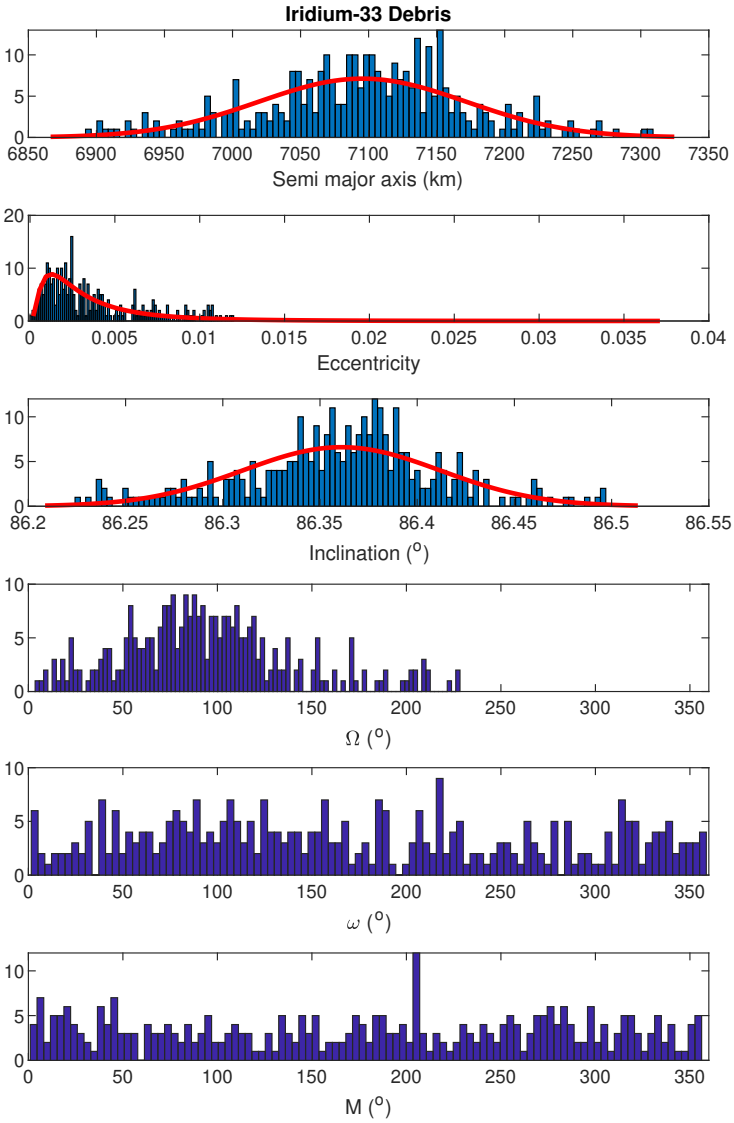

Figure 6.2: Distribution of orbital elements of tracked Iridium-33 debris.

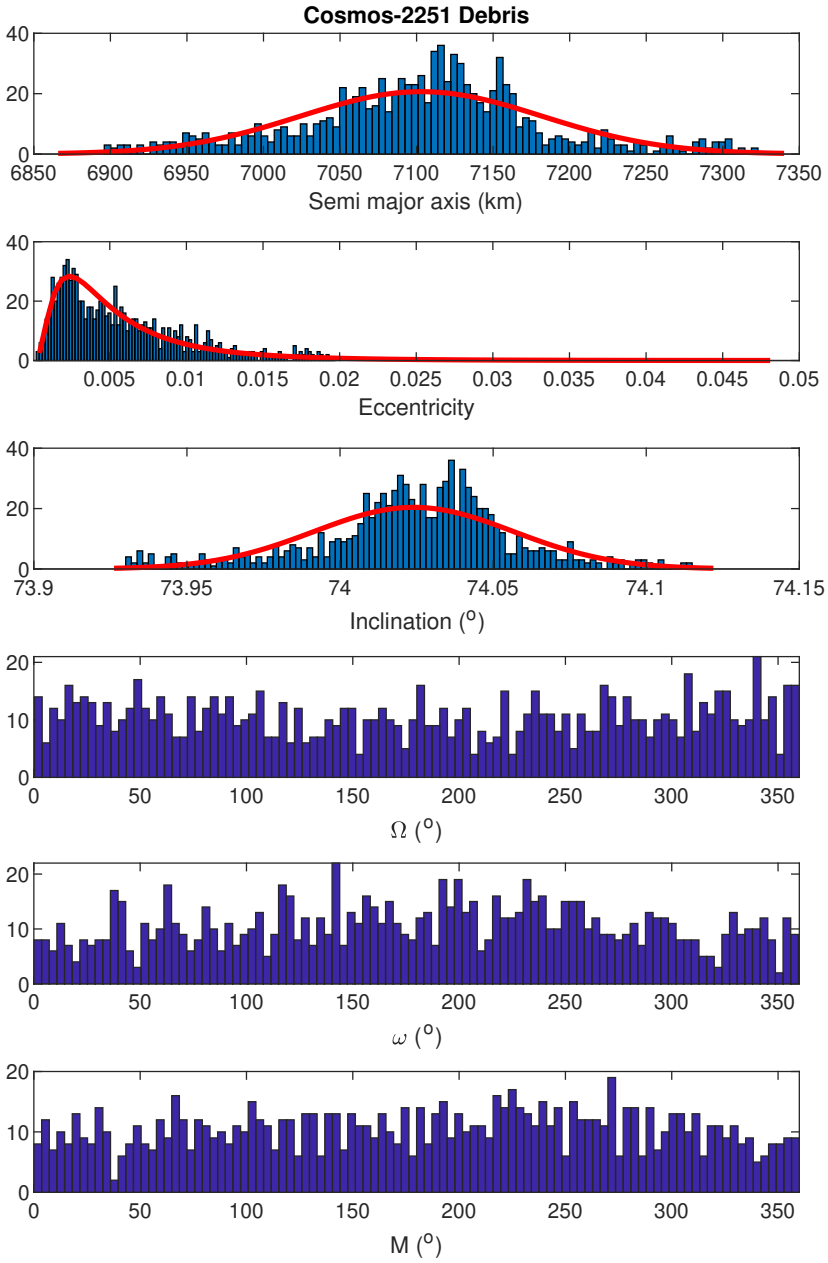

Figure 6.3: Distribution of orbital elements of tracked Kosmos-2251 debris.

a (km)	e	i (^{o})	Ω (^{o})	ω (^{o})	ν (^{o})
7578.1	0.002	45	0	0	0

Table 6.1: Orbital elements of the satellite used for interaction characterisation.

shell, as expected from differential precession from the J_2 perturbation (Pardini and Anselmo, 2011). The dispersion on Ω was smaller for the Iridium-33 debris, because the original satellite was in a more inclined orbit, leading to slower precession (Pardini and Anselmo, 2011).

Taking these findings into account, debris orbits were generated at the chosen central altitude of 1200 km. Semi-major axis and inclination were generated using a normal distribution centered on the pre-collision values of 7571 km (Earth's radius plus 1200 km) and 45 degrees respectively, and standard deviations equal to the average of those in the examined Iridium-Kosmos clouds. Eccentricity was generated using a log-normal distribution, using parameters equal to the average of the Iridium-33 and Kosmos-2251 clouds' distribution parameters. Since the pre-collision inclination is only 45 degrees - far from a polar orbit - it was assumed that the cloud had already spread out into a quasi-uniform shell. Thus, Ω, ω and M were generated as uniform random numbers between 0 and 359.9 degrees.

6.1.5 Target Acquisition and Encounter Characterisation

The next step is to identify a large set of encounters between spacecraft and debris fragments during which the fragment can be optically acquired by the camera, and hence the beam can be steered onto the object.

The orbit of a single satellite is chosen in order to characterise interactions on a per-satellite basis, since the final mission involves multiple satellites. The orbital elements of the satellite are shown in Table 6.1. Here a is the semi-major axis, e is the eccentricity, i is the inclination, Ω is the longitude of the ascending node, ω is the argument of the periapsis, and ν is the true anomaly. Distances are in kilometres and angles in degrees.

Here Ω, ω and ν can take any value since debris is generated uniformly with respect to these variables, and so they are simply set to zero. This semi-major

axis is chosen as the radius of Earth plus the 1200 km central altitude of the debris shell.

Next, the orbits of the satellite and the fragments are propagated for a 10-year mission timespan. After propagation of the orbits with an initial coarse timestep of 10 s (after downselection, the filtered encounters are re-propagated with a 1 s timestep), the satellite and debris orbital states across the entire timespan are saved. The trajectories of individual fragments are then compared with the trajectory of the satellite to obtain a curve $s_n(t)$, which is the separation between fragment n and the satellite as a function of time. These curves oscillate with the orbits of the bodies in question, producing many local minima across the 10-year mission duration.

After propagating the 632 fragments with one satellite for 10 years, over 55 million candidate events (local minima) were identified. Of course, not all of these local minima correspond to close approaches - for example, local minima may occur when the two objects are on opposite sides of the planet from one another. However, the true close approaches much be contained within this set and can be extracted by applying various selection criteria based on the dynamics of each candidate event.

The first downselection is a simple condition on the distance at the instant of closest approach - that it must be less than 1000 km. This removes candidates which are certainly too distant to acquire with the camera, as well as ensuring cases corresponding to the object being on the opposite side of the planet are removed. This initial trimming reduces computation time for the subsequent conditions which involve more detailed trajectory analysis.

The next downselection is performed by setting a requirement on the geometric configuration of the two objects at the moment of closest approach which determines if the object is inside the camera's field of view. If the vector originating at the spacecraft and ending at the fragment is called $\mathbf{S}$, and $\mathbf{V}_{sc}$ is the velocity vector of the spacecraft at the moment of closest approach, then the angle between $\mathbf{S}$ and -$\mathbf{V}_{sc}$ must be less than 15 degrees. This firstly ensures that the fragment is behind the spacecraft during the interaction, which ensures the

resultant momentum will be in an appropriate direction to lower the periapris of the fragment. If the fragment is moving slowly enough across the field of view to be successfully imaged (ensured by the final criterion), the orbits must be similar, and so the difference between the anti-velocity directions cannot be large. This criteria also accounts for the limited field of view of the camera, which is assumed to be 30 degrees in later calculations. Note that the velocity vector of the spacecraft is used rather than the fragment's, as the concept is specifically designed to not rely on knowledge of the fragment's orbit, which would use up valuable time in the limited observation window since Earth-based observations are assumed to not be capable of detecting small, high-altitude fragments.

The second condition relates to detectability by the camera system and determining if sufficient signal to noise ratio (SNR) is achievable for a given encounter event. If the object to be imaged is not moving relative to the image plane, for any given noise condition the exposure duration can always be increased until the required SNR is achieved, in absence of pixel saturation. However, if there is relative motion between the object and the camera and tracking is not possible, the object will move across the field of view. The condition for detectability then becomes that the required SNR must be achievable before the object moves to the next pixel.

To determine if this condition is met, the relative angular velocity of the downselected events must be calculated. Let $\boldsymbol{S}$ be the separation vector originating at the spacecraft and ending at the fragment. Let $\boldsymbol{V}_R$ be the velocity of the fragment relative to the satellite. $\boldsymbol{V}_R$ has a component perpendicular to $\boldsymbol{S}$, which we shall call $\boldsymbol{V}_P$, where $\|\boldsymbol{V}_P\| = \sin(\phi)\|\boldsymbol{V}_R\|$, where ϕ is the angle between $\boldsymbol{S}$ and $\boldsymbol{V}_R$. At the instant of closest approach, the instantaneous relative angular velocity Θ can be found by considering the infinitesimal change in relative angular position of the fragment $d\theta$ over infinitesimal time dt to be

$$\frac{d\theta}{dt} = \Theta = \frac{\|\sin(\phi)\boldsymbol{V}_R\|}{\|\boldsymbol{S}\|} \tag{6.1}$$

as illustrated in Figure 6.4.

The detectability criterion then becomes that Θ must be less than some max-

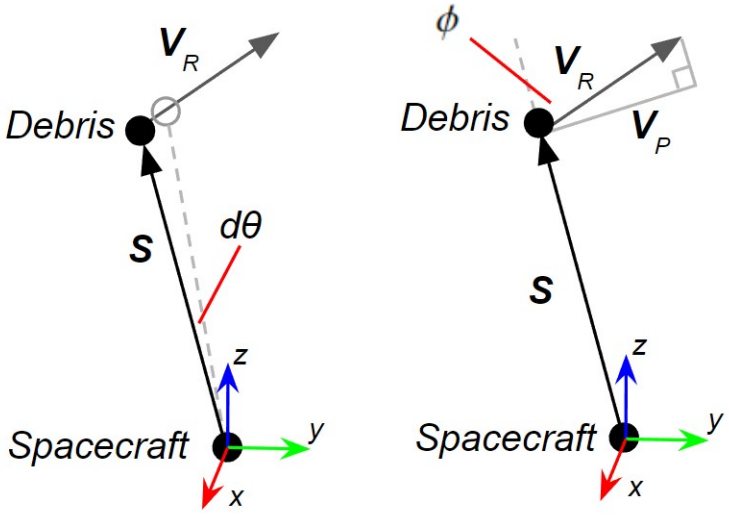

Figure 6.4: Illustration of the geometry for calculation of the instantaneous relative angular velocity.

imum value which is determined by the dynamics and geometry of the encounter.

6.1.5.1 Optical Acquisition of Debris Fragments

Analysis on optical acquisition is performed by estimating the SNR of pixels containing the fragment compared with background pixels. SNR is here defined as the ratio of the mean signal photon count of a pixel containing the fragment μ_s, to the standard deviation of the noise counts in background pixels σ_n. Since photon counting follows Poisson statistics, the SNR can be calculated according to

$$SNR = \frac{\mu_s}{\sigma_n} = \frac{\mu_s}{\sqrt{\mu_n}} \tag{6.2}$$

The expected, or mean, signal photon count per pixel per exposure, μ_s, must now be derived. If the solar irradiance as a function of wavelength λ is $\Phi_\odot(\lambda)$, the albedo of the fragment is α_F, the phase angle of illumination is ϕ and the area of the fragment is A_F, then the total solar energy reflected from the fragment E_{ref} is

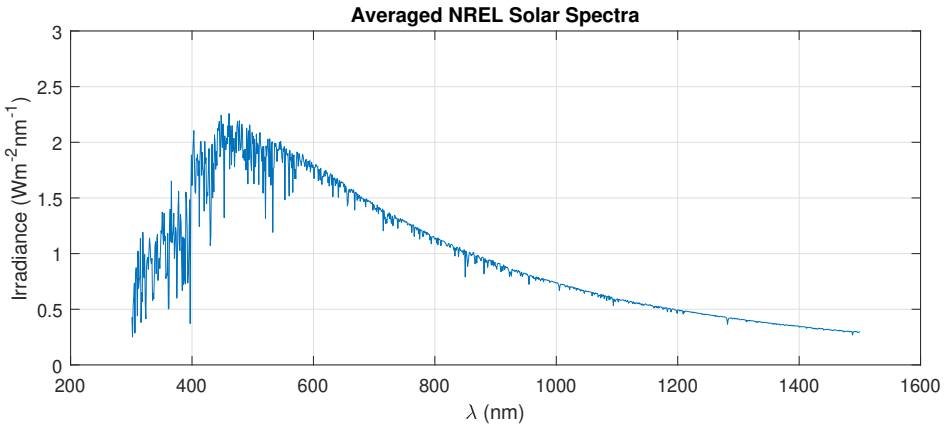

Figure 6.5: Averaged NREL extraterrestrial solar spectra.

$$E_{ref} = A_F \alpha_F \cos 2\phi \int_{\lambda_a}^{\lambda_b} \Phi_{\odot}(\lambda) d\lambda \tag{6.3}$$

where the camera is sensitive to the wavelength band λ_a to λ_b. Spectral data for sunlight from space can be freely obtained from the National Renewable Energy Laboratory website (NREL) (Figure 6.5) and is used to perform this integration and accurately determine the reflected flux.

If one assumes isotropic reflection of this light over a hemisphere, then at some distance R from the fragment, the flux of reflected light Φ_{ref} is

$$\Phi_{ref} = \frac{E_{ref}}{2\pi R^2} \tag{6.4}$$

If the camera has a collecting aperture with area A_{col}, and an overall photon-to-electron system efficiency η_c, and the mean wavelength of the band is λ_m, with an exposure duration t_{exp}, the expected number of signal photons collected per second per pixel μ_s can be written as

$$\mu_s = \frac{A_F \alpha_F \cos 2\phi A_{col} \eta_c \lambda_m}{2\pi R^2 h c n_{px}} \int_{\lambda_a}^{\lambda_b} \Phi_{\odot}(\lambda) d\lambda \tag{6.5}$$

Here n_{px} is an additional factor which accounts for the finite point spread function of real cameras - since the fragment is small and distant, it is expected to be smaller than a single pixel in all cases, and thus the light from the fragment is modelled as being spread evenly over n_{px} pixels due to the point spread function

(PSF) of real optical systems. In reality, the PSF would likely have brighter central pixels compared with the periphery, so the approximation of dividing equally over n_{px} pixels will not give erroneously optimistic results.

Background, or noise, counts in a CCD typically consist of several sources - dark counts, background photons originating from sources inside the field of view, and readout noise. In this case, it is assumed that observations will only be made when the Sun is not inside the FoV, and the camera will always be pointed such that Earth is also out of the FoV - thus there will be no major source of non-image photons entering the aperture. Since the spacecraft does not know in advance where and when fragments will appear, it should point its camera in its negative velocity direction in order to increase likelihood of detecting fragments in similar orbits (with low angular velocity) and better alignment between the separation vector the fragment's negative velocity vector - which, if the orbit is similar, will be close to the spacecraft's negative velocity vector. This can be seen in Figure 6.6.

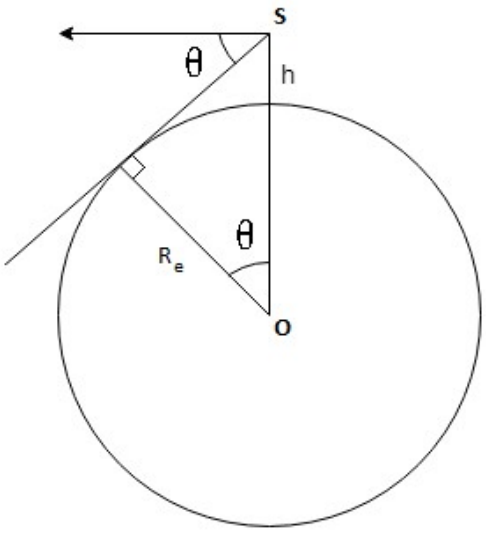

Figure 6.6: Illustration of the maximum field of view half angle that can be used without having Earth in-shot.

If the satellite is at altitude h, then the angle between the negative velocity direction and the horizon is

$$\theta = \cos^{-1}(\frac{R_e}{R_e + h}) \tag{6.6}$$

which is 32.70^o for a 1200 km altitude circular orbit, thus the assumption of Earth being outside the FoV is valid for a camera with a 30 degree (15 degree half-angle) FoV.

Thus the noise is assumed to be dominated by dark noise and readout noise. The mean noise photon count per pixel μ_n can be written as

$$\mu_n = Dt_{exp} + R \tag{6.7}$$

where D is the mean dark count rate per pixel, and R is the mean readout noise per pixel per exposure. In space-based CCD imagers, sub-100 Hzpx^{-1} dark count rates have been demonstrated with active cooling, with around 10 Hzpx^{-1} being achievable at temperatures of -30 Celsius (Gilard et al., 2010). Given the large capacity power delivery and storage systems that will be required for the laser system on board each satellite for this mission, it is reasonable to assume an additional 2-5 Watts of power will be available for CCD active cooling to reduce dark count rate to the 10 Hzpx^{-1} level, and so this is the rate of dark electron generation used in SNR calculations. Thus, using this method, for any given distance and exposure duration, the SNR of the pixels containing the image of the fragment relative to the background can be calculated.

From the above Equations it is possible to determine the minimum required exposure duration to accrue some minimum SNR at any instant in the encounter. At this stage, the camera's exposure duration is considered to be variable, and only the possibility of achieving the desired SNR is to be assessed. For the object to be observable, the time spent on a single pixel must be greater than or equal to the time required for some minimum SNR at that distance $t_{min}(R)$. t_{px} can be expressed simply in terms of the angular size of a pixel and the relative angular velocity, thus the condition for observability at a given instant t (recognising that Θ and R are both functions of t) is

$$\frac{\theta_{px}}{\Theta(t)} \geq t_{min}(R(t)) \tag{6.8}$$

.

The curves $t_{min}(R)$ for the hexnut were calculated for various SNR thresholds using the camera parameters in Table 6.2, and the resulting curves are shown in Figure 6.7.

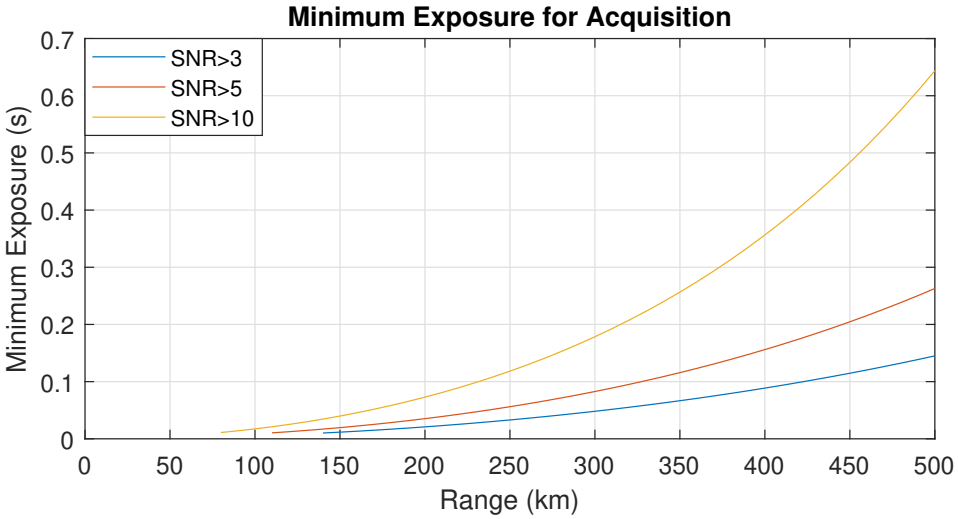

Figure 6.7: Minimum required exposure at a given range to achieve the specified SNR.

It is now possible to determine, for each time point during an encounter, if the object is observable using Equation 6.8, i.e. if there exists some exposure duration which is simultaneously short enough to prevent motion blur, while being long enough to achieve the minimum SNR, which was set to 5. An example of the separation curve (left axis) and the times at which the observability condition is satisfied (right axis) can be seen in Figure 6.8. As can be seen, initially the object is unobservable because the combination of distance and angular velocity result in SNR buildup being too slow. This is followed by a period around the closest approach where SNR buildup rate is fast enough for the fragment to be observed, and then as the fragment recedes the condition is no longer met and it becomes unobservable again. This specific example should not be taken as an indication of a specific maximum observation distance, as this is also dependent on the angular velocity caused by the 'difference' between the two orbits. Observation

windows of several minutes were typical in the studied population, allowing a reasonable length of time to acquire the target, point the laser and illuminate it. The observation window indicates which portion of each encounter should be processed by high-fidelity interaction model, as only the periods where the object is visible should be simulated.

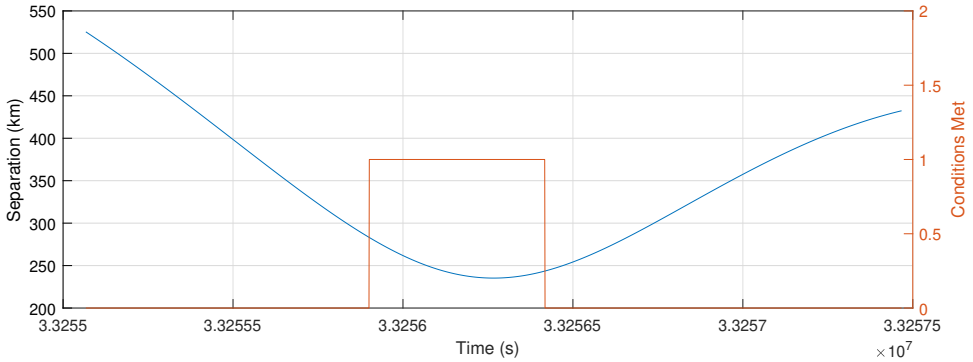

Figure 6.8: Example of information extracted on the dynamics of a single encounter. The orange curve (right axis) is the binary condition where 1 denotes all conditions for observability are met at that instant.

Parameter	Value
Circular Aperture Diameter	20 cm
Fragment Albedo	0.5
Camera Efficiency	40%
Bandwidth	400 - 750 nm
Solar Irradiance	1.5 $Wm^{-2}nm^{-1}$
Debris Illuminated Area	2.034e-4 m^2
PSF	4 pixels
Central Wavelength	550 nm
Dark Count Rate	10 Hz px^{-1}
Mean Read Noise	5 counts $exposure^{-1}$ px^{-1}

Table 6.2: Camera, object and solar parameters used in imaging SNR analysis. The area of the fragment corresponds to the cross-sectional area of the 3D model of the hexnut.

6.1.6 Encounter Time Separation

After the downselection criteria have been applied, we are left with a list of viable encounters between a single satellite and individual fragments in the cloud, the times at which they occur, and the fragment that is involved. From this, it is

also possible to extract information on the encounter rate (e.g. the number of fragments encountered per day per satellite), which will be important in later stages of the analysis. Timestamps of all viable interactions were used to obtain the distribution of the time between each pair of consecutive events, which is shown in Figures 6.9-6.11. There is clear structure in these distributions, with peaks occurring at half-integer multiples of the satellite period ($T_{satellite} = 6558.2$ s). This indicates that in many cases, the satellite re-encounters the same object multiple times over consecutive orbits at their nodal points, as one would expect given that they are in similar orbits. This distribution can be scaled up to an arbitrary size of debris population, as the distribution of time between events will be the same. The mean time between events is 41802 s, or on average 0.483 encounters per day. When scaling up to a more realistic population of 5000, the expected event rate is approximately 4 encounters per day. This high encounter rate suggests that the rate of interaction may be limited by the power system and not the encounter rate.

The distribution of time between consecutive events can be seen in Figures 6.9 - 6.11. These will be used in later sections.

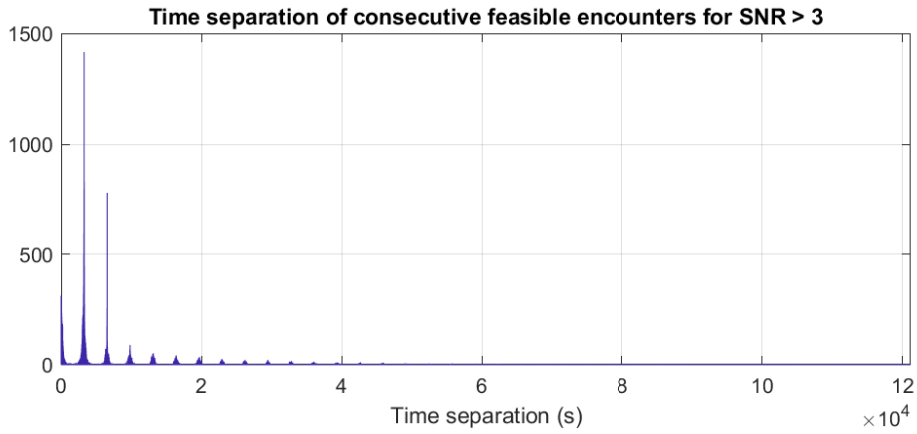

Figure 6.9: Distribution of feasible encounter time separation for SNR > 3.

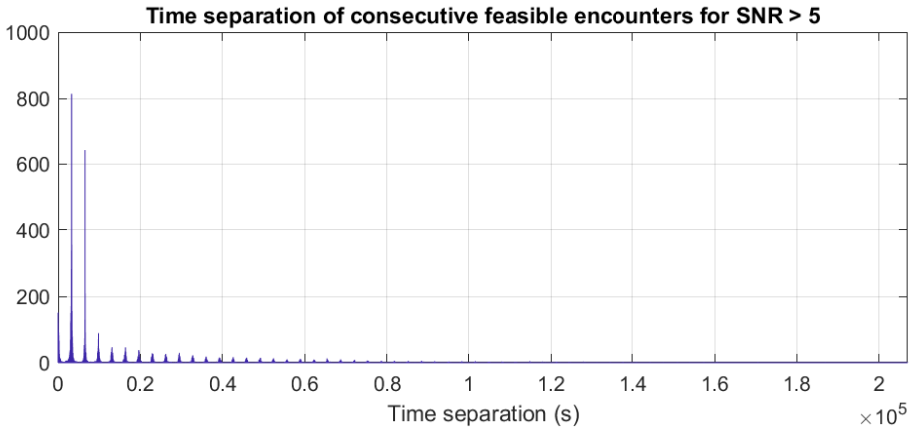

Figure 6.10: Distribution of feasible encounter time separation for SNR > 5.

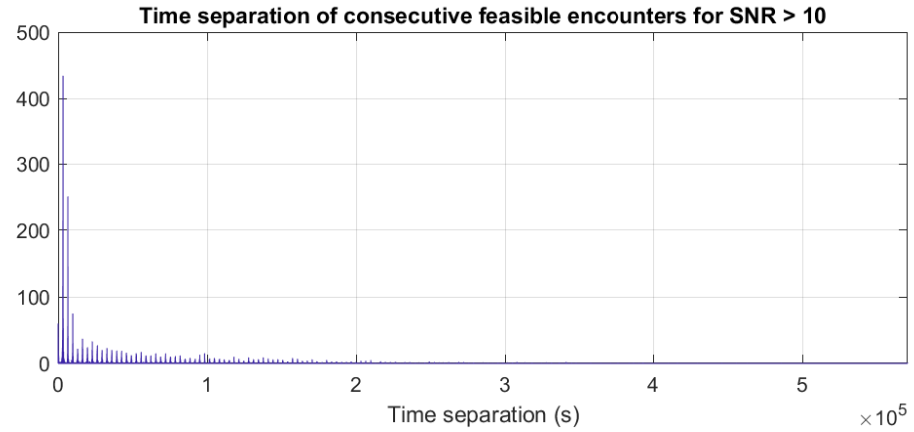

Figure 6.11: Distribution of feasible encounter time separation for SNR > 10.

6.1.7 Longitudinal Laser Profile

As previously mentioned, this concept does not assume the availability of ranging measurements and variable-focus beams. This subsection will discuss optimisations of the focal plane location and waist radius to maximise the irradiance delivered to fragments during interactions.

For a Gaussian, near-single-mode beam, the minimum possible beam divergence is $\theta_d = M^2 \frac{\lambda}{2\pi w_0}$, where λ is the laser wavelength and w_0 is the beam waist radius - the radius of the most tightly focussed point along the beam axis. The factor M^2 (greater than or equal to 1), known as the beam quality factor, captures any deviation from a perfectly Gaussian beam profile.

From this, simple geometry allows the beam radius $w(R)$ at any given longitudinal distance from the focal plane (or beam waist) to be calculated according to

$$w(R) = w_0 + \sqrt{(R - z_0)^2}\tan(\theta_d) \tag{6.9}$$

where R is the distance from the emitter, w_0 is the waist radius, and z_0 is the focal plane's distance from the emitter - thus the term $\sqrt{(R - z_0)^2}$ is the distance of the point of interest from the focal plane.

The simplest approach would be to simply have the waist radius at the emitter, or $z_0 = 0$. However, since this concept deals with long ranges and the effect of the interaction depends strongly on the irradiance incident on a fragment's surface, alternatives should be explored that allow for higher irradiance to increase surface fluence and thus rate of momentum transfer.

It is important to note that z_0 cannot be arbitrarily chosen, but is constrained by the maximum size of the emitter on board the spacecraft. If the waist is located some distance z_0 from the emitter, then the size of the beam at the aperture, (thus the required optics radius) can be obtained from Equation 6.9 by setting $R = 0$. Figure 6.12 shows the relationship between desired waist radius and required emitter size, with z_0 fixed at several values.

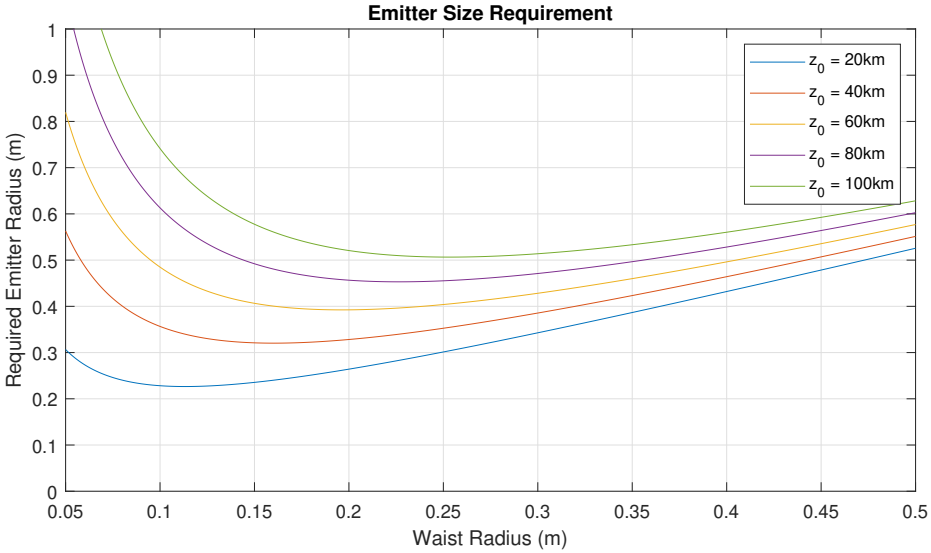

Figure 6.12: Emitter size requirement for various z_0 and w_0.

It can be seen that larger emitters allow the waist to be placed further away from the craft, and thus a higher fluence to be delivered to the target. A constraint on the size of the emitter must exist since it must fit on board the spacecraft, but precisely defining this is outwith the scope of this thesis. An approximate upper limit of $w_e = 0.1$ m was chosen to constrain the parameters z_0 and w_0. Since long-distance interactions are required, it is desirable to have the focal plane as far from the spacecraft as possible for a given emitter size to maximize the fluence at the target. From Figure 6.12, z_0 should be reduced until the the upper limit of $w_e = 0.1$ is tangential to the curve, giving the optimised laser profile to maximise irradiance on the target. The optimal focal plane distance was found to be $z_0 = 15.59$ km with a waist radius $w_0 = 0.1$ m. These optimal parameters are used in the laser-debris interaction modelling in later sections.

6.1.8 Characterisation of Impulse Transfer

After downselecting the database of encounters to only those feasible for camera tracking, it is now possible to pass the dynamics of these events into the high-fidelity laser interaction model described in the previous Chapter to determine the net effect of such interactions on the state of the fragments.

Because the photon pressure model loops over many timesteps, it is fairly slow to run and as such, processing tens of thousands of encounters would be prohibitively slow, and so a method to statistically generate ΔV vectors for each interaction was developed. To achieve this, a random subset of 4500 of the feasible encounters found in the previous section is processed by the interaction model to form a database of net impulse vectors which will retain any statistical relations between the debris orbits relative to the spacecraft, and the net effect of the interaction.

For each encounter that is simulated, the states of the satellite and fragment during the interaction period are used to obtain the incidence direction $\hat{\boldsymbol{i}}(t)$ and range $R(t)$. For each simulation, the initial rotation state and angular velocity vector are randomly generated to account for the fact that debris fragments will be tumbling. The total optical power of the laser was modelled as 10 kW.

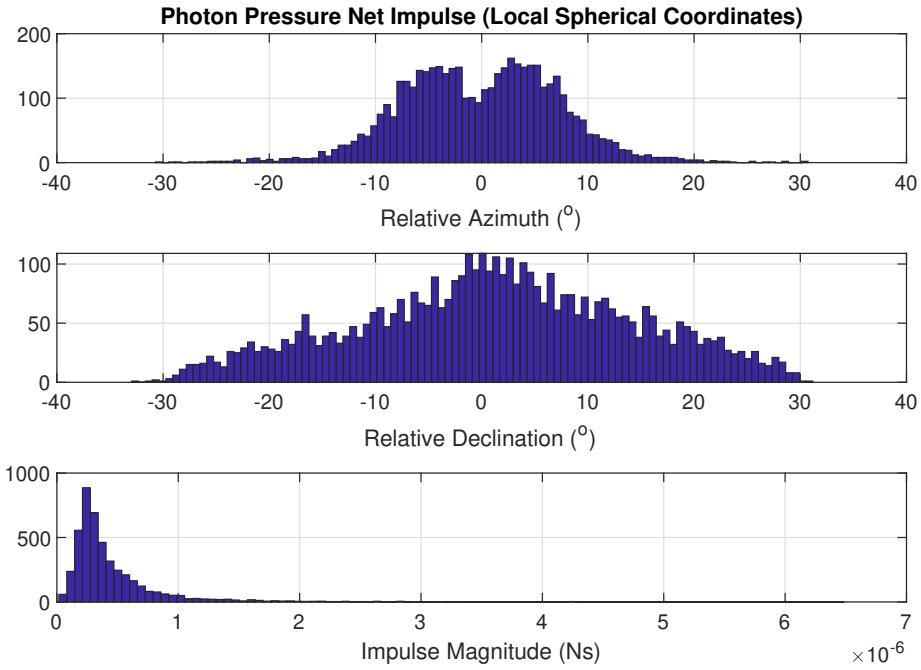

Figure 6.13: Distribution of azimuth, elevation and magnitude of net transferred impulse for photon pressure.

After the LDI model computes the net impulse vector, it is expressed in spherical coordinates relative to the local radial-tangential-normal frame of reference (with the tangential direction parallel with the satellite's negative velocity vector) centered at the location of the satellite at the distance-weighted mean time during the interaction window. These distributions can be seen in Figure 6.13, which are used to generate azimuth, elevation and magnitude values for interactions in later sections.

6.1.8.1 Size and Material Variation

Debris fragments produced in a breakup event will of course not be of uniform size and material composition, unlike the population of fragments simulated. However, as can be seen from Equations 5.22 and 5.27, achieved $\Delta\mathbf{v}$ from laser interaction is directly proportional to the illuminated area (thus $\propto l^2$), and, in the case of ablation, the momentum coupling coefficient C_m. It follows that the change in velocity may then be scaled up or down depending on the physical

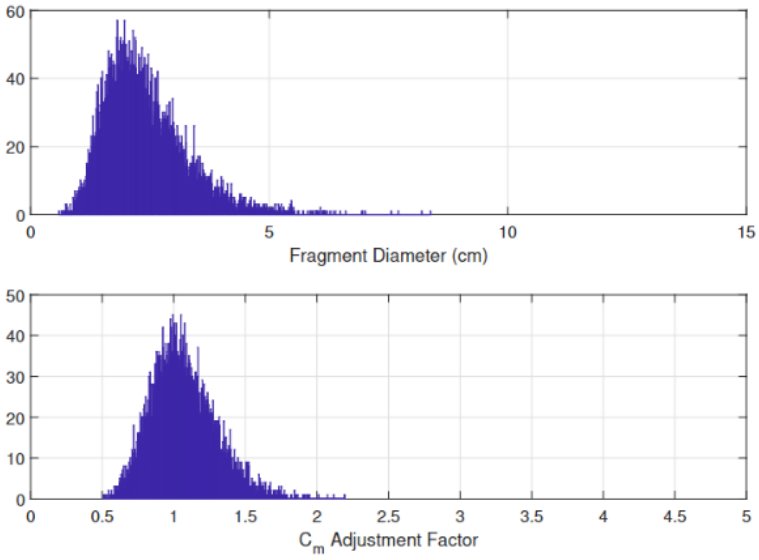

Figure 6.14: Distribution in fragments' diameter d and C_m scaling factor.

parameters of the object in question relative to those of the simulated object. To model variation of fragment diameter and material around the 'typical' values of the actual simulated object, a distribution of fragment diameters and 'adjustment factors' for C_m were generated (Figure 6.14) and assigned to each fragment, and used to appropriately scale the $\Delta\mathbf{v}$ for each encounter.

This approach allows a far lower number of interaction simulations to be performed, reducing simulation time substantially.

6.1.9 Mission Impact Assessment

Now that methods for modelling the velocity change due to laser interaction and quickly generating impulsive interactions have been established, it is possible to use these models to assess the long-term impact of the proposed mission concept.

The single-satellite encounter statistics obtained previously are now used to extend to constellations of N_{sat} satellites. This is done by generating, for each satellite, a series of timestamps representing debris encounters, where each encounter is associated with a randomly assigned fragment identifier number. All encounter events are then combined into a single list, allowing iteration through fragment ID and encounter time to propagate a fragment's orbit piecewise to each encounter, applying an impulsive ΔV each time.

The distribution in Figure 6.10 (for encounters with SNR > 5) is used to generate a series of values of Δt between consecutive events for a single satellite. Time intervals between successive encounters for each satellite are generated which span a mission duration of 10 years. To account for some events occuring in eclipse periods, thus the fragments being invisible to the camera, exactly 50% of these events are removed at random, although the true portion would be slightly less than this.

Recharge time of the onboard batteries was also accounted for, by checking that consecutive events have sufficient time for a full recharge of the batteries. To estimate this, a power draw of 30 kW (i.e. 33% laser efficiency) is assumed. A solar panel area of 5 m^2 with an efficiency of 25%, and an additional correction factor of $\frac{1}{2}$ (to account for eclipses) is assumed to estimate the battery recharge rate. The duration of interaction windows of all identified viable events was analyzed, and a minimum time between successive events $\Delta t_{min} = 32655$ s was chosen which ensures that for 80% of all viable encounters it is possible to recharge sufficiently to illuminate the fragment for the full duration of the interaction. If an event was found to occur less than Δt_{min} after the preceding event, it was removed from the set of encounters to be simulated.

Finally, a fragment identifier number between 1 and N_{frag} is randomly generated and assigned to each generated encounter. These steps are repeated for the number of satellites in the constellation, $N_{sat} = 100$, to produce a database of every viable encounter between any fragment in the shell and any satellite in the constellation over the mission duration.

This database of encounters, containing an event timestamp, fragment identifier and satellite identifier are now sorted in time order, and split into a series of interactions for each individual fragment. This allows each fragment's orbit to be propagated to the timestamp of its next interaction, an impulsive ΔV applied to the state, and its orbit to then be re-propagated to the next interaction time, and so on until the end of the mission duration.

The impact of the mission can be assessed by looking at the reduction in periapsis and reduction in lifetime of the population after the 10 year mission

duration. The latter lifetime comparison was performed by propagating the perturbed and unperturbed fragments' orbits until reentry (defined as when the altitude drops to 300 km). Results for the periapsis change for the fully simulated fragments after 10 years of operation can be found in Figure 6.15.

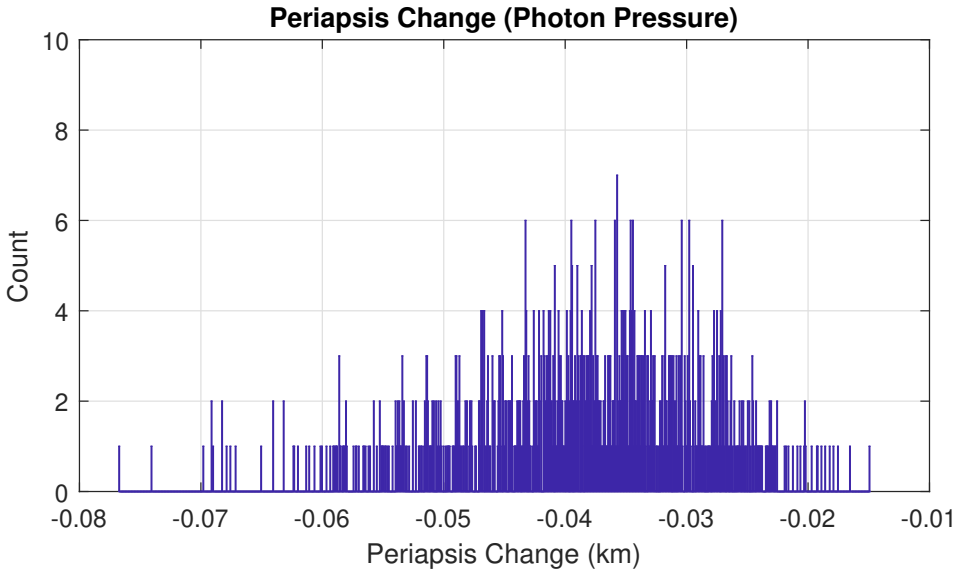

Figure 6.15: Change in periapsis after the 10 year mission duration.

It can be seen from these results that the periapsis change with respect to the unperturbed orbit in the case of photon pressure is only on the order of tens of metres. This did not lead to any meaningful effect on the lifetime of the propagated fragments, which indicates that photon pressure is simply too weak an interaction mode to be practical for the total removal of even small fragments of space debris.

6.2 Concept Adaptation for Collision Avoidance

In the previous section, it was found that opportunistic laser interaction with debris fragments using photon pressure resulted in a negligible change in the periapses of affected fragments. However, for the laser parameters used, the change in velocity for the targeted small fragments, while small, was non-negligible when one considers not lifetime reduction, but simply fragment displacement some time after the interaction. Single interaction velocity changes were on the order of 1

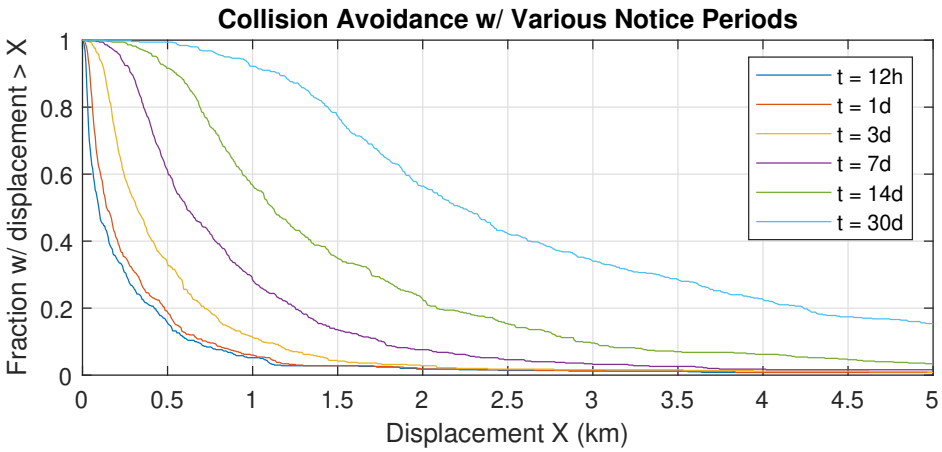

Figure 6.16: Fraction of encounters resulting in displacement > X after a variable notice period.

mms^{-1}. For linear motion, over the course of a single day this results in a displacement of 86.4 metres. For the International Space Station, debris approaching within 2 km radially and 25 km both along-track and out-of-plane are considered to be hazardous enough to potentially warrant collision avoidance maneuvers by the station (Mark Garcia, 2021). With sufficient notice, this level of displacement may be achievable using photon pressure without orbit matching, as proposed in previous sections for the debris removal concept.

To investigate this, the same 2 cm hex nut as in previous simulations was used to represent a typical small fragment. In this case, only a single impulsive ΔV from the database was applied to simulate the effect of a one-time opportunistic interaction using the same 10 kW CW laser on a threatening piece of debris. Displacement from the unperturbed position at future times was calculated for 500 different impulse vectors. This allows the fraction of encounters resulting in a minimum displacement at some notice time t_{notice} to be obtained. This is shown in Figure 6.16. These results show that displacements on the order of 2 km could be achieved with a notice period of approximately two weeks or more, which could be increased with a higher power laser.

In the case of the ISS, the most practical approach is likely to simply perform a collision avoidance maneuver using the existing orbit maintenance system. However, it could be envisioned that future industrial operations in orbit could involve

much larger and more massive stations requiring more robust defences against space debris, and which are also less capable of performing avoidance maneuvers. For example, nuclear reactors may be used to power future heavy industry in space, for which collisions with small pieces of debris could have much more devastating consequences than simply cracking a window. For stations requiring high levels of protection from debris impacts, it is possible that the proposed concept, although ineffective for debris removal, could be adapted for the purposes of collision avoidance - cataloguing the orbits of all passing fragments in the orbital vicinity using angles-only measurements, and using this knowledge to predict collisions and interact with threatening fragments as they are identified.

To investigate the feasibility of this adaptation of the concept, the orbits of an N-satellite constellation were simulated along with that of a randomly generated, single fragment with the same statistics as previously, to investigate the encounter rate between the fragment and any satellite in the constellation. The satellites were initialised in an evenly spaced orbital shell, with identical a, e, i and ω, and with Ω and ν spanning 360 degrees in increments of $\frac{360}{N}$ degrees. Orbits of all bodies were propagated for one day (86400 s), and the separation between the fragment and each satellite was tracked. An example of this can be seen in Figure 6.17, where each curve represents the distance to one of the satellites in the constellation.

With a constellation of only 10 satellites, it was typical to observe a closest approach of < 200 km within a one-day timeframe, which is a typical range for the fragment during an interaction window. Results for the closest encounter with any satellite in the constellation in one day across 500 randomly generated fragments are shown in Figure 6.18.

The time until the first approach closer than 200 km with any satellite is also shown in Figure 6.19. 90% of the sub-200 km encounters occur in less than 27.3 hours, and 95% occur in less than 36.8 hours.

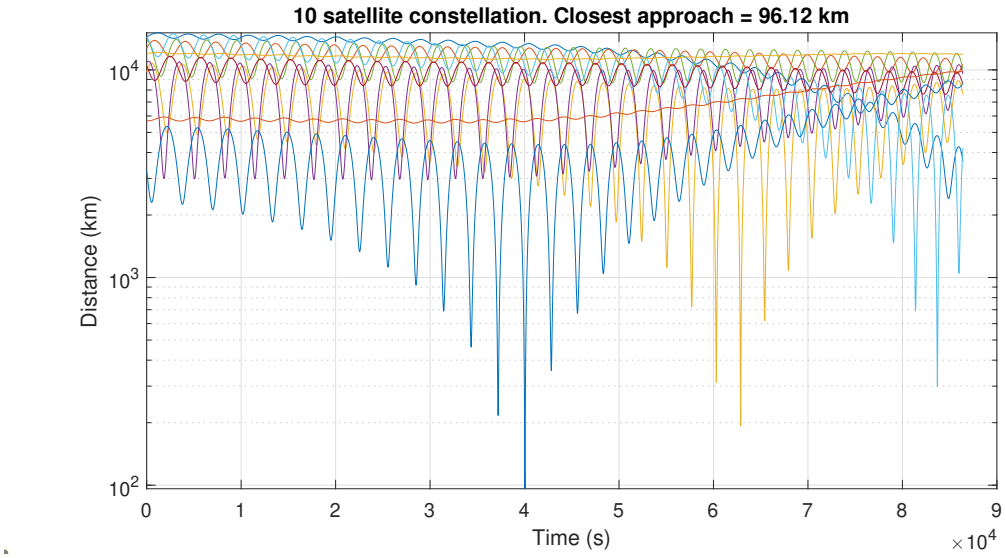

Figure 6.17: Magnitude of separation between a fragment and each satellite in a 10-satellite constellation over one day. Each curve represents the distance to one of the satellites in the constellation.

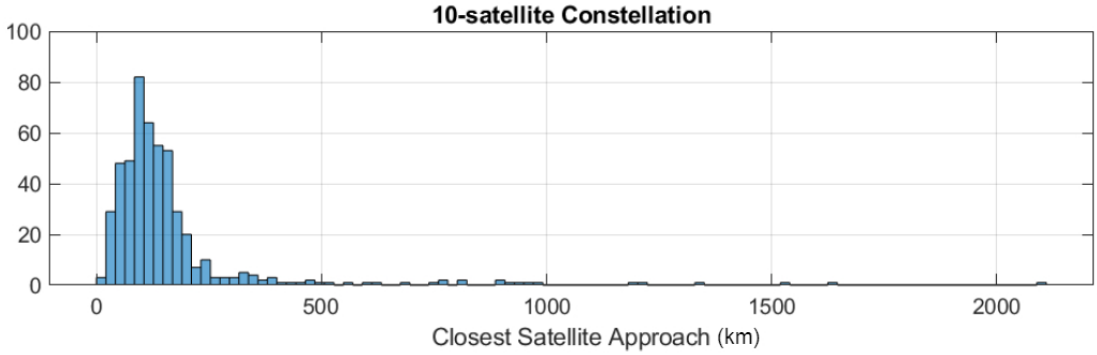

Figure 6.18: Closest approach with any satellite in the constellation for 500 randomly generated fragment orbits after one day.

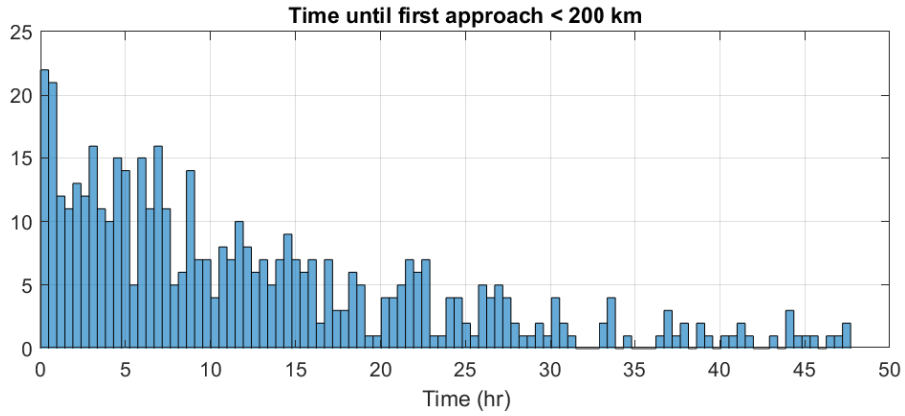

Figure 6.19: Time until the first encounter with any satellite closer than 200 km.

This indicates that with a very reasonably-sized constellation of 10 satellites, fragments in the vicinity of the constellation's orbit will approach close enough to one of the satellites to be nudged by the illumination laser in less than two days after identification of a threat. Unless the notice period is very short, it is likely that a fragment will in fact have multiple encounters with satellites before the moment of the potential collision. This indicates that this concept may indeed have potential to be adapted for the purposes of cataloguing debris fragments in the vicinity of high-value stations and intervening should a collision risk be detected.

6.2.1 Power System Considerations

Two major challenges for deployment of such spacecraft carrying high-powered lasers for debris mitigation are the power demand and heat production. In the photon pressure cases proposed above for both orbit lowering and collision avoidance, a 10 kW (optical) continuous-wave laser was simulated. Assuming an overall electrical-to-optical efficiency of 30%, this would require a total power draw of 33.3 kW. At a further 30% solar panel efficiency, a total panel area of 81 m^2 would be required under ideal illumination conditions to power such a laser directly with solar power. This is at the very least unwieldy, although spacecraft with similar sized arrays have been deployed in the past. Since the laser is only intended to be operational for a small fraction of the total time in orbit, it would likely make

more sense to power the laser with stored energy in batteries, charged using solar panels during inactive periods. For a 3-minute interaction at 33 kW, 1.66 kWh of total electrical energy would be required from the battery pack. Using commercially available lithium ion cells with energy density 265 Whkg^{-1}, sized for a 50% depth of discharge to improve battery life, 12.5 kg of cells would be required to meet the power demands, which is not unreasonable for a small satellite.

In the case of a pulsed laser interacting via ablation, time-averaged electrical-to-optical efficiency is likely to be much lower due to multiple gain stages each requiring one or several multi-Watt pump lasers to excite the active medium, each operating at standard CW laser efficiencies of around 30% - thus pulsed lasers cannot achieve efficiency higher than their pump sources. Non-maximised pulse rates with continuous pumping also lead to wasted energy that does not contribute to pulse energy or peak power. Considering additional power lost to processes such as amplified spontaneous emission and thermal processes which are likely to be a problem in such a high-energy laser system, an overall time-averaged efficiency of 1% is assumed for the pulsed case. For the simulated laser which fires 300 3kJ pulses per interaction, a total energy draw from the battery pack of 25 kWh would be required. Again allowing for a 50% depth of discharge, this would require a 94 kg lithium ion battery pack. Optical power 'lost' to a portion of the oversized beam missing the target has already been accounted for in the interaction model.

6.3 Ablative Interactions

Given that ablation exhibits a significantly larger momentum coupling coefficient than photon pressure, it is possible that adapting the concept presented in Section 6.1 to use ablation may result in a more meaningful reduction in orbital lifetime. This Section will present results of the same mission analysis for the case of ablative interactions.

6.3.1 Reaching the Ablation Threshold

As explained in Chapter 4, there is a minimum fluence threshold for achieving ablation, as well as an optimum fluence Φ_{opt} which is dependent on material, pulse duration and wavelength. For aluminium, the optimum fluence is approximately 14 Jcm^{-2}. Using the same laser and optical design as in the photon pressure concept, to achieve 14 Jcm^{-2} at 200 km would require a laser pulse energy of approximately 660 kJ, which is far beyond the capability of a laser system that could be deployed in space.

Loosening the aperture size restriction however would allow the focal plane to be placed further from the spacecraft, increasing the fluence and thus reducing pulse energy requirements for ablation. Repeating the same longitudinal profile optimisation process as before, this time with $M^2 = 1.3$ (Figure 6.20), an aperture radius of 60 cm was found to be sufficiently large to allow the focal plane to be placed at 200 km, with a spot radius of 30 cm. This yields an angular diameter of 1.5 μrad, which can be taken as an estimate of the pointing accuracy requirement of the beam steering system when operating at 200 km.

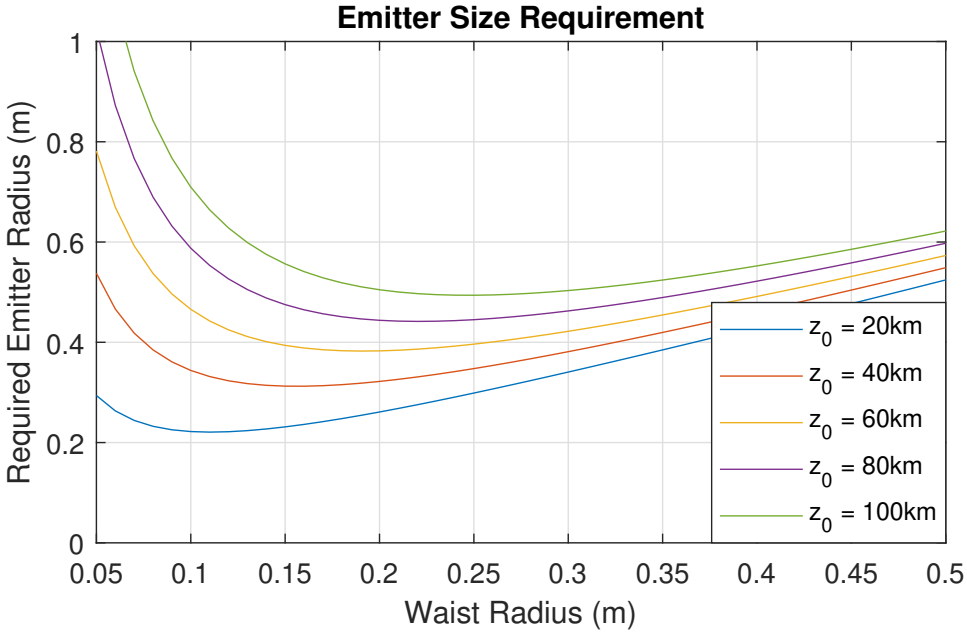

Figure 6.20: Relationship between waist radius, focal plane distance and emitter size for ablation case.

The fluence as a function of distance for this case is plotted in Figure 6.21 for a

pulse energy of 50 kJ. This together with typical C_m curves for aluminium (Figure 5.7) indicates that, for a larger aperture, given sufficient pulse energy, ablation could be achieved at a wide range of distances from the aperture, however the required pulse energy is extremely high, since the low-divergence beam that allows this wide range of operation is inherently larger in area.

While the pulse energy in this case is more moderate than 660 kJ, this is still far in excess of the likely capabilities of a smallsat-scale laser. For this reason, it can be concluded that range tracking and variable focusing is indeed a requirement when utilising ablation to affect the orbits of space debris. Going forward, when considering the adaptation of the previous concept to the case of ablation, it is assumed that these capabilities exist on board the satellite, and that a near-constant fluence on the target, near to Φ_{opt}, can be achieved. Thus, a constant value of $C_m = 20$ NsμJ^{-1} is used.

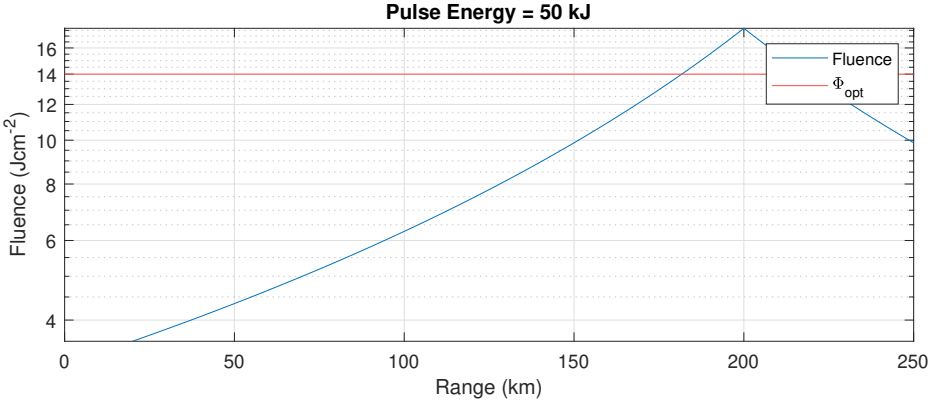

Figure 6.21: Laser fluence as a function of distance for a 60 cm radius aperture. Fluence increases as the beam nears the focal plane.

6.3.2 Mission Impact for the Ablation Case

The same mission impact assessment was repeated for the case of ablative interactions, assuming a beam waist radius of 1 metre, which tracks the target longitudinally as mentioned in Section 6.3.1, and a pulse energy of 3 kJ. 300 pulses are applied in each interaction, at a randomly selected location in time during the interaction window. This assumes that the interaction begins as soon as the object is observed, and that the number of pulses is limited due to cool-

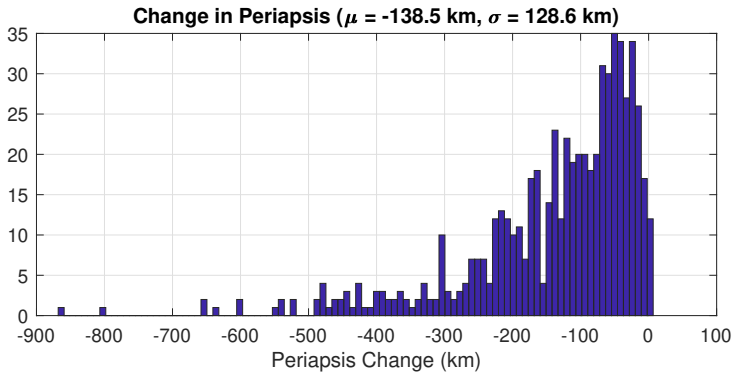

Figure 6.22: Change in periapsis for the propagated fragments using laser ablation.

ing considerations and power storage capacity, so operation of the higher-power pulsed laser for the full interaction window may not be possible. An equivalent database of resultant impulse vectors was constructed for the ablation case, and drawn from to simulate the mission just as in the photon pressure case. A total of 295 fragments were propagated for the 10 year span, simulating the effect of each ablative interaction with the satellites it encounters.

In this case, as expected, there was a much more significant reduction in periapsis than for the photon pressure case. A mean periapsis reduction of 179.5 km was found in the propagated fragments. The distribution of periapsis and lifetime reduction for the ablation case can be seen in Figures 6.22-6.23. These results indicate a significant reduction in orbital lifetime for an entire population of debris fragments may be achievable, given that sufficient fluence on the target is achievable. Although the mechanism of ablation is far more promising than photon pressure, significantly more technological (and likely regulatory) hurdles stand in the way of deployment: producing multi-kilojoule pulse energies on a miniaturised space-borne platform, likely operated using battery power or supercapacitors, dealing with significant amounts of waste heat with only radiative cooling, and constructing large, steerable optics which can withstand such high pulse energies. In comparison with these development risks, more 'obvious' risks such as inadvertently shooting a satellite or person on the ground are easy to deal with.

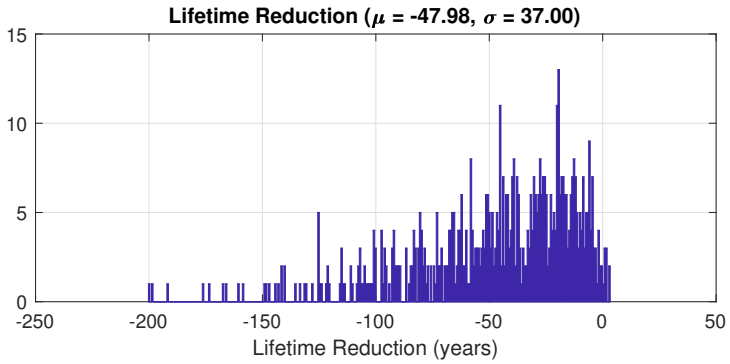

Figure 6.23: Change in orbital lifetime for the propagated fragments using laser ablation.

6.4 Dynamic Effects of Extreme Laser Fluence

In addition to the intended outcome of along-beam-axis momentum transfer, extreme laser fluence on complex geometries will also have additional, unintended effects on the attitude motion and transverse velocity relative to the observer. This Section will study and discuss these effects, enabled by the high-fidelity model developed in Chapter 4.

6.4.1 Attitude Motion Evolution

For arbitrary incidence angles on complex geometries, it is likely that unbalanced forces due to laser pressure or ablation will induce a torque on the object in question, which will in turn begin rotating in microgravity conditions. A reasonable hypothesis is that fragments may, depending on their geometry, tend towards an orientation state that minimises torque, much like an analogous aerodynamic scenario. This was investigated by performing simulations with the previously introduced model for photon pressure, with the laser power raised to an extreme level of 10 GWm^{-2} to accelerate the effect and reduce the required simulation time. This is a good approximation for a rapid-pulse ablation scenario, in which the force could be approximated as continuous.

When considering a thin, square aluminium plate with light incident at an angle $\frac{\pi}{4}$ radians to the local normal on one face, naively one would expect a net torque of zero, since the surface fluence is simply $\Phi_0 \cos\frac{\pi}{4}$ at all locations.

However, due to the model accounting for small tangential components to the reaction force on a surface element, the result is a net torque for all combinations of α and S that do not cause the tangential components to cancel.

The 'low-drag configuration' idea was investigated by simulating again the previously mentioned square plate. With 10 cm side length and 5 mm thickness, and the density of aluminium (2710 kgm^{-3}) the plate had a mass of 135.5 grams. Its principal components of inertia are $I_x = 2.258 \times 10^{-2}$ kgm^2, $I_y = 1.132 \times 10^{-2}$ kgm^2, $I_z = 1.132 \times 10^{-2}$ kgm^2. With the extreme surface fluence, the angular acceleration about the torque axis was only 8.83×10^{-13} rads^{-1}. This indicates that for the flat plate, there is no strong restoring force which tends to bring the object into any preferred orientation as in the aerodynamic scenario.

More complex geometries were simulated as well to investigate attitude evolution. Firstly, an L-shaped block was simulated, again with constant density equal to that of aluminium. For this object it was found that there exist certain metastable orientations (such as the one illustrated in Figure 6.24), where upon initialisation of the simulation with zero angular velocity, the object initially remains almost motionless. However, with the tiniest deviation from this state arising from floating-point precision errors, the orientation begins to oscillate with increasing amplitude before being thrown into a tumbling motion. An example of the time evolution of the angular velocity magnitude can be seen in Figure 6.25. For cases with a random slow initial tumble, over many simulations no attractor states of minimum 'drag' were identified. In these simulations, the direction of the incident light with respect to the inertial frame was held constant, no relative motion between the beam and the object was simulated.

The same hexnut model as in the mission simulation was also simulated, resulting in similar findings to the L-shape with regards to lack of attractor states. However, a preference for spin-up about the short axis was observed, where the short axis maintains a specific angle with respect to the beam axis (similar to the orientation in Figure 5.1, where the beam propagation direction is aligned with the $-z$ axis). This could be considered a quasi-attractor state in the case of the hexnut, with respect only to the direction of the short axis. The time evolution

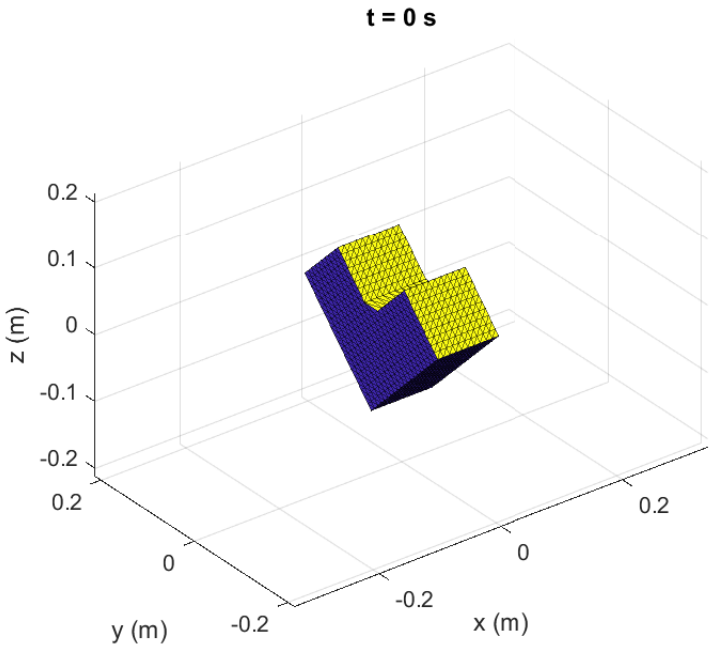

Figure 6.24: L-shaped block in a metastable orientation under ultra-high fluence (10 GW m^{-2}) photon pressure.

of angular velocity and torque magnitudes for the hexnut can be found in Figure 6.26.

These results indicate that under extreme CW illumination, or high repetition rate pulsed interactions, there will be no tendency towards a single preferred orientation which minimises the force applied - rather there is a tendency for the spin-up of more complex objects, which may have preferred pointing directions for a single body axis, although this is dependent on the geometry. However, the effect is small, and only manifested when using unreasonably extreme fluence, and thus is unlikely to be a concern in the case of realistic fluences with photon pressure.

6.4.2 Lateral Movement of Fragments During Ablative Interaction

For complex geometries, the net force from ablation will not always be parallel with the beam axis. Since the impulse from a single pulse can result in a

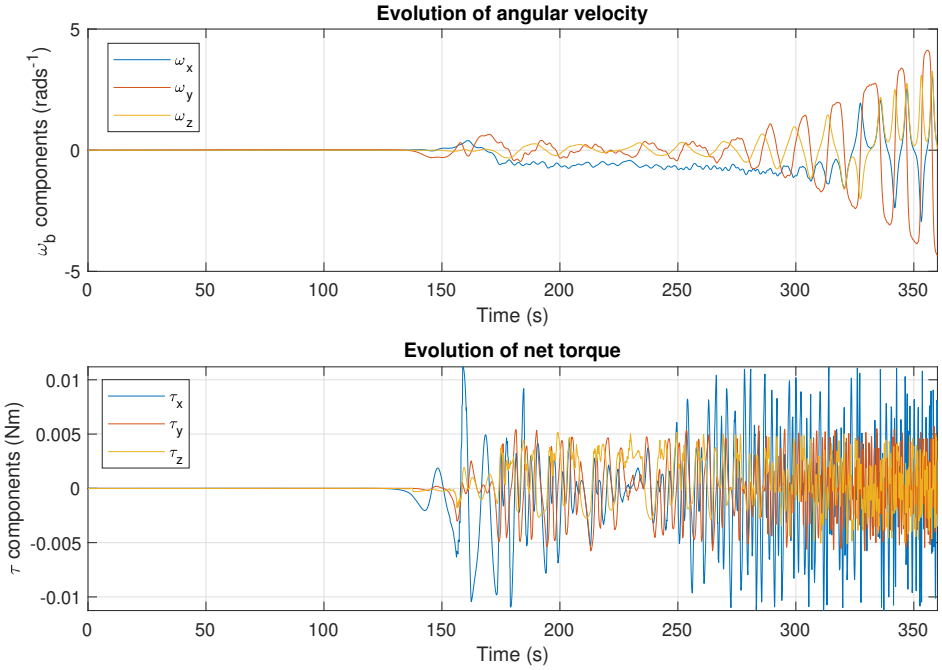

Figure 6.25: Time evolution of angular velocity and net torque components for the L-shaped block under extreme laser fluence (10 GW m^{-2}), starting from the metastable state in Figure 6.24.

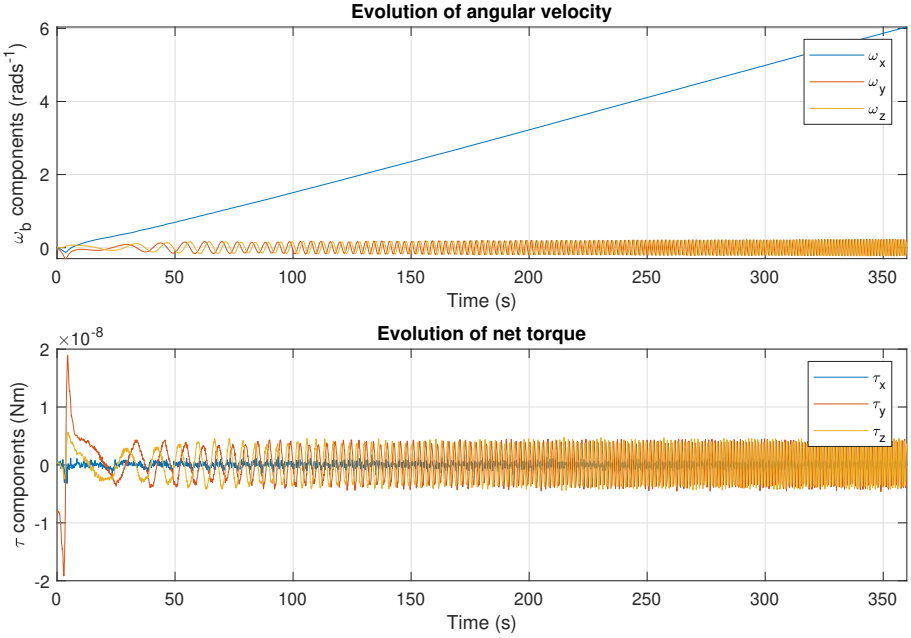

Figure 6.26: Similar spin-up behaviour observed with the hexnut 3D model under a lesser fluence of 0.1 GW m^{-2}. Continual spin-up about the short axis was observed for the hexnut.

meaningful change in velocity for a small, light object, if this effect causes large sideways movement of the fragment relative to the beam direction, beam steering to ensure the target remains illuminated may become an issue.

To investigate this, a test case was set up using the hexnut model, with a pulse energy of 4.4 kJ focussed to a spot of diameter 10 cm, which achieves the optimum fluence of 14 Jcm^{-2} for aluminium. The resultant $\Delta\mathbf{V}$ vector was calculated according to Equation 5.27, and then decomposed into its components parallel and perpendicular to the beam propagation axis. 500 single pulses were simulated, for random initial orientations.

The results of this Monte Carlo simulation can be seen in Figure 6.27, showing a large portion of the resultant impulse is applied in directions perpendicular to the beam axis. This indicates that upon initiation of ablative interaction, a fragment will deviate significantly from its unperturbed path across the sky relative to the spacecraft. Thus a concern for the actual implementation of laser ablation of space debris is the ability to track the fragment as it takes a seemingly random path across the field of view, being kicked in a new direction by each consecutive pulse.

6.5 Discussion

In this Chapter, the use of both continuous-wave and pulsed lasers for the remediation of small debris fragments in Earth orbit was studied in the context of a new space-based mission concept proposal. The concept involved the deployment of a small constellation of satellites into an orbital altitude band that is particularly debris-dense, for example the shell of debris produced by a satellite collision. It was shown that on-board cameras would be capable of optically acquiring passing fragments with no prior knowledge of their orbits from Earth-based observations. This then allows on-board lasers to target the fragment and transfer momentum at a distance without orbit matching, using either photon pressure or ablation of material from the fragment. A detailed surface-element model constructed in the previous Chapter was used to simulate the momentum transfer in both cases

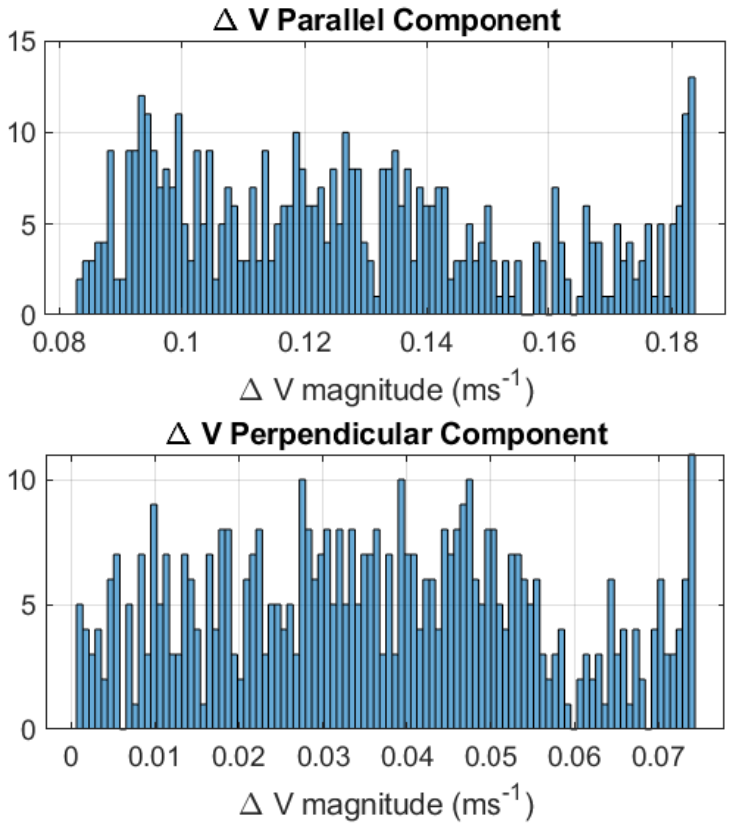

Figure 6.27: Components of the resultant impulsive ΔV from ablation with respect to the beam axis direction for the hex nut.

using the respective interaction equations.

Results indicated that in the case of photon pressure, the effect on the periapses of affected fragments was small, and there was negligible change in the lifetimes of these fragments. However, when simulating the same mission using ablation as the interaction mechanism, a significant lifetime and periapsis reduction was found to be possible. The use of ablation however does require that sufficient fluence on the surface of the object is achievable, likely by a combination of future developments in compact, high-pulse-energy lasers along with variable-focus optics which allow the longitudinal tracking of the focal plane to coincide with the object being ablated. These considerations however are beyond the scope of this Chapter and this thesis. The effect of lateral movement of the fragment due to the off-axial components of the ablation reaction force were also investigated, and it was found that the $\Delta\mathbf{V}$ vector due to a single pulse has significant off-axis components, indicating tracking challenges will be likely in a real mission scenario, especially where the spot size is on the order of tens of centimetres and precise tracking of the target is a necessity.

The constellation approach using photon pressure was also adapted for the goal of collision avoidance, where the satellites could act to defend a high-value space asset from debris by cataloguing debris in the vicinity of the station, and interacting with those fragments that pose a collision risk. It was found that while the notice period would not be suitable for fast, emergency collision avoidance, it would be possible to displace a small fragment by one kilometer with around one week or more of notice, using only a single interaction with a satellite. Encounter rates with a 10-satellite constellation and an individual fragment were also analyzed, and it was found that 95% of satellite encounters occur within 36.8 hours of notification of a collision risk, indicating that a moderately sized constellation may be sufficient to protect such a future space station.

Chapter 7

Conclusions

This thesis presented models and analyses relating to several novel applications of lasers in space safety, specifically the estimation of asteroid masses using a two-way intersatellite ranging system, the development of a new ranging instrument architecture applicable to the previously proposed experiment, and the mitigation of risks posed by space debris by using lasers to affect fragment orbits.

After summarising the context, motivations and contributions of this thesis in Chapter 1, Chapter 2 presented a brief overview of laser physics and some laser system architectures. In Chapter 3, a novel technique for measuring the mass of asteroids and other space objects was presented, using laser ranging to measure the relative trajectory deflection of a pair of satellites due to the gravity field of the target space object. This new technique was shown to be capable of estimating mass with better performance than has been demonstrated in real space missions to date, while being capable of doing so in a fast flyby without the need for rendezvous and orbit insertion maneuvers. It was also shown that the proposed instrumentation architecture could function with low-energy pulses, enabling use on smallsats or nanosats with very limited size, weight and power budgets. The error in mass estimation was investigated with various flyby configurations as a primary measure of system performance, and it was found that an asymmetrical, opposing configuration, with the asteroid passing between the two spacecraft, closer to one than the other, offered the best potential for sensitivity to gravitational perturbation of their trajectories relative to one

another. After accounting for flyby targeting errors, the expected error in the mass estimate was found to be less than 10% for objects heavier than 10^9 kg assuming a 100 m uncertainty in the asteroid's location at the time of flyby, and approximately 30% for objects heavier than 10^8 kg with a 1000 m position uncertainty. This is an important result as the probing of asteroid mass will be critical in the near future, if not for asteroid deflection attempts, certainly for other purposes such as asteroid mining. As these simulations were performed considering a specific asteroid encounter scenario, future work may consider faster and slower encounters with different objects to determine the effect of the flyby speed on the mass estimation error. The range of configurations tested was also rather limited, with a separation of 2 km on the B-plane for all simulations. Future work may consider different configurations such as having one spacecraft much further away to increase the gravity differential and potentially further improve the system performance. Finally, future work may also consider the experiment performance as it relates to the accuracy of the intersatellite ranging system, as better or worse range accuracy than was modelled in this thesis may be achievable in reality which will directly impact the quality of the measurement. Although it is clear that there still remains room for exploration relating to asteroid mass estimation via intersatellite ranging, this thesis has shown that the concept is fundamentally sound.

Chapter 4 then presented a novel technique for performing laser ranging capable of highly accurate measurements, despite using somewhat simple hardware - a long pulsed laser source and a simple CCD sensor. It was shown that this technique is capable of obtaining the level of range accuracy and precision required for the mass estimation experiment proposed in Chapter 3, given sufficient stability in exposure duration of the CCD. One key result and possibly the main advantage of this technique over traditional two-way ranging is the low sensitivity to clock asynchronisation. It was found that, while the systematic error in a traditional TWR system based on time of flight increases linearly with clock asynchronisation, an equivalent clock offset in this system results in a far smaller change in measurement error since the exposure time is far larger than the asynchronisation

offset. While this method has been shown to have potential in these very early simulations, future work should of course consider other sources of error related to real world implementation and instrument assembly such as pulse shape stability and errors in parameters such as optical and quantum efficiency. The lack of sensitivity to clock asynchronisation was a key finding in this Chapter, as this is one of the main limitations of traditional laser ranging systems. The mechanism behind this - the long exposure and pulse duration relative to the error in synchronisation - does suggest however that the technique may also be reasonably insensitive to errors in other parameters which affect the photon count, for the same reason.

Chapters 5 and 6 together consider the remediation of space debris using lasers. Chapter 5 presented a high-fidelity model of the imparted force due to photon pressure and ablation, which enables higher-precision modelling of these effects compared with the simplified approaches generally used in existing mission simulations of laser-based space debris remediation. It was found that the imparted force, due to the geometry of the object as well as the more complex model describing the different components of the photon pressure reaction force, can deviate meaningfully from the direction of the beam axis. This is a very important factor to consider when modelling the effect of these interventions, as it may significantly reduce the orbit-lowering effect of the laser illumination compared with the ideal case.

Finally, Chapter 6 used the high-fidelity model presented in Chapter 5 to simulate the impact of a debris remediation mission concept using a constellation of satellites attempting to remove a shell of debris produced by a collision event. It was found that while photon pressure was not a sufficiently strong interaction mechanism to cause meaningful changes to orbital lifetime or altitude, ablation was indeed capable of lowering the orbits of affected fragments and reducing their lifetimes by a useful amount. The key contribution here was the study of a distributed, space-based swarm of illuminating satellites which interact opportunistically with passing fragments - a novel mission architecture which has not previously been proposed. Another key contribution of this Chapter was to show

the feasibility of optically acquiring previously untracked debris fragments from space with no prior knowledge of their orbits, enabling the laser to track and interact with objects which may not be trackable from ground. The concept was then adapted for the objective of collision avoidance only using photon pressure, and it was found to be a potentially effective strategy to defend future high-value stations, with displacements of several kilometers being achievable from only a single interaction given a notice period of several days. Assuming a new, threatening fragment had just been identified, the likely response time of the constellation was analysed. Using a constellation of only 10 satellites in evenly spaced, inclined orbits, for the simulated debris population it was found that after 27.3 hours, 90% of fragments would encounter a satellite in the constellation, and after 36.8 hours, 95% of fragments would encounter a satellite. Finally, the previously unstudied effect of $\Delta\mathbf{V}$ misalignment with the beam axis, due to target shape and orientation, was investigated for the ablation case. It was found that a significant component of the achieved $\Delta\mathbf{V}$, for the hexnut shape, was in directions perpendicular to the beam axis, likely causing significant, sudden, unpredictable movements of the fragment in the microgravity environment making laser tracking more challenging. Although a higher-fidelity model was developed and used in this thesis, one effect that was not studied and implemented in the model was mass removal, which remains to be investigated in future work. Future studies may also consider a more varied range of geometries of different sizes, as this work used only one 3D model composed of one material, to represent a typical debris fragment.

Bibliography

B. Abbott, R. Abbott, R. Adhikari, P. Ajith, B. Allen, G. Allen, R. Amin, S. Anderson, W. Anderson, M. Arain, et al. LIGO: the laser interferometer gravitational-wave observatory. *Reports on Progress in Physics*, 72(7):076901, 2009.

B. P. Abbott, R. Abbott, T. Abbott, M. Abernathy, F. Acernese, K. Ackley, C. Adams, T. Adams, P. Addesso, R. Adhikari, et al. Observation of gravitational waves from a binary black hole merger. *Physical Review Letters*, 116(6): 061102, 2016.

S. Amoruso, R. Bruzzese, C. Pagano, and X. Wang. Features of plasma plume evolution and material removal efficiency during femtosecond laser ablation of nickel in high vacuum. *Applied Physics A*, 89(4):1017–1024, 2007.

G. Avanzini. Spacecraft attitude dynamics and control. *Politecnico di Torino, Tech. Rep*, 2008.

C. Bamann, U. Hugentobler, S. Scharring, J. Kästel, and S. Setty. Analysis of collision avoidance via ground-based laser momentum transfer. *Journal of Space Safety Engineering*, 7(3):312–317, 2020.

O. Barnouin, M. Daly, E. Palmer, C. Johnson, R. Gaskell, M. Al Asad, E. Bierhaus, K. Craft, C. Ernst, R. Espiritu, et al. Digital terrain mapping by the OSIRIS-REx mission. *Planetary and Space Science*, 180:104764, 2020.

P. Battocchio, J. Terragni, N. Bazzanella, C. Cestari, M. Orlandi, W. Burger, R. Battiston, and A. Miotello. Ballistic measurements of laser ablation generated impulse. *Measurement Science and Technology*, 32(1):015901, 2020.

Blue Canyon Technologies. Blue Canyon Technologies XACT Series CubeSat ACDS Datasheet. URL https://satcatalog.s3.amazonaws.com/components/84/SatCatalog_-_Blue_Canyon_Technologies_-_XACT-100_-_Datasheet.pdf?lastmod=20210708022807. Retrieved August 2021.

C. Bombardelli and J. Peláez. Ion beam shepherd for asteroid deflection. *Journal of Guidance, Control, and Dynamics*, 34(4):1270–1272, 2011.

C. Bonnal, C. Dupont, S. Missonnier, L. Lequette, M. Merle, and S. Rommelaere. Just-in-time collision avoidance (JCA) using a cloud of particles. *LPI Contributions*, 2109:6062, 2019.

D. M. Boroson and B. S. Robinson. The lunar laser communication demonstration: NASA's first step toward very high data rate support of science and exploration missions. In *The lunar atmosphere and dust environment explorer mission (LADEE)*, pages 115–128. Springer, 2015.

F. Brandi, N. Burdet, R. Carzino, and A. Diaspro. Very large spot size effect in nanosecond laser drilling efficiency of silicon. *Optics Express*, 18(22):23488–23494, 2010.

M. Calabro and L. Perrot. XXI century tower: Laser orbital debris removal and collision avoidance. *Acta Astronautica*, 158:220–230, 2019.

J. Campbell. Project ORION: Orbital debris removal using ground-based sensors and lasers. *NASA Technical Memorandum 108522*, 1996.

D. Casanova, A. Petit, and A. Lemaître. Long-term evolution of space debris under the J2 effect, the solar radiation pressure and the solar and lunar perturbations. *Celestial Mechanics and Dynamical Astronomy*, 123(2):223–238, 2015.

J. F. Cavanaugh, J. C. Smith, X. Sun, A. E. Bartels, L. Ramos-Izquierdo, D. J. Krebs, J. F. McGarry, R. Trunzo, A. M. Novo-Gradac, J. L. Britt, et al. The Mercury Laser Altimeter instrument for the MESSENGER mission. *Space Science Reviews*, 131(1):451–479, 2007.

Celestrak. NORAD general perturbations (GP) element sets. URL `https://www.celestrak.com/NORAD/elements/`. Retrieved: November 2020.

T. D. Cole, A. F. Cheng, M. Zuber, and D. Smith. The laser rangefinder on the Near Earth Asteroid Rendezvous spacecraft. *Acta Astronautica*, 39(1-4): 303–313, 1996.

E. Conca, I. Cusini, F. Severini, R. Lussana, F. Zappa, and F. Villa. Gated spad arrays for single-photon time-resolved imaging and spectroscopy. *IEEE Photonics Journal*, 11(6):1–10, 2019.

E. Cordelli, A. Di Mira, T. Flohrer, S. Setty, I. Zayer, S. Scharring, H. Dreyer, G. Wagner, J. Kästel, E. Schafer, et al. Ground-based laser momentum transfer concept for debris collision avoidance. *Journal of Space Safety Engineering*, 9 (4):612–624, 2022.

A. De Brum and F. Da Cruz. Reviewed plan of the ALR, the laser rangefinder for the ASTER deep space mission to the triple asteroid 2001-SN263. In *Journal of Physics: Conference Series*, volume 911, page 012016. IOP Publishing, 2017.

G. Ehret, P. Bousquet, C. Pierangelo, M. Alpers, B. Millet, J. B. Abshire, H. Bovensmann, J. P. Burrows, F. Chevallier, P. Ciais, et al. MERLIN: A French-German space LIDAR mission dedicated to atmospheric methane. *Remote Sensing*, 9(10):1052, 2017.

A. Einstein. Zur quantentheorie der strahlung. *Phys. Z.*, 18:124, 1917.

E. Eloranta. *Range-Resolved Optical Remote Sensing of the Atmosphere*. Springer, 2008.

European Space Agency. Space debris by the numbers. URL `https://www.esa.int/Safety\_Security/Space\_Debris/Space\_debris\_by\_the\_numbers`. Retrieved: 29 April 2022.

J. L. Forshaw, G. S. Aglietti, N. Navarathinam, H. Kadhem, T. Salmon, A. Pisseloup, E. Joffre, T. Chabot, I. Retat, R. Axthelm, et al. RemoveDEBRIS: An

in-orbit active debris removal demonstration mission. *Acta Astronautica*, 127: 448–463, 2016.

J. L. Forshaw, G. S. Aglietti, T. Salmon, I. Retat, M. Roe, C. Burgess, T. Chabot, A. Pisseloup, A. Phipps, C. Bernal, et al. Final payload test results for the RemoveDebris active debris removal mission. *Acta Astronautica*, 138:326–342, 2017.

G. Ganguli, C. Crabtree, L. Rudakov, and S. Chappie. Active debris removal by micron-scale dust injection. In *2012 IEEE Aerospace Conference*, pages 1–9. IEEE, 2012.

A. Gibbings, M. Vasile, I. Watson, J.-M. Hopkins, and D. Burns. Experimental analysis of laser ablated plumes for asteroid deflection and exploitation. *Acta Astronautica*, 90(1):85–97, 2013.

O. Gilard, C. Boatella-Polo, J.-C. Dolado-Perez, M. Auvergne, G. Quadri, and M. Boutillier. CoRoT satellite: analysis of the in-orbit CCD dark current degradation. *IEEE Transactions On Nuclear Science*, 57(3):1644–1653, 2010.

K.-H. Glassmeier, H. Boehnhardt, D. Koschny, E. Kührt, and I. Richter. The rosetta mission: flying towards the origin of the solar system. *Space Science Reviews*, 128:1–21, 2007.

J. Guo and C. Han. Where is the limit: The analysis of cubesat ADCS performance. In *4S Symposium 2016, Valletta, Malta*, pages 1–15. European Space Agency and the Centre National d'Etudes Spatiales, 2016.

K. Gwinner, F. Scholten, F. Preusker, S. Elgner, T. Roatsch, M. Spiegel, R. Schmidt, J. Oberst, R. Jaumann, and C. Heipke. Topography of Mars from global mapping by HRSC high-resolution digital terrain models and orthoimages: Characteristics and performance. *Earth and Planetary Science Letters*, 294(3-4):506–519, 2010.

M. A. Itzler, X. Jiang, M. Entwistle, K. Slomkowski, A. Tosi, F. Acerbi, F. Zappa,

and S. Cova. Advances in InGaAsP-based avalanche diode single photon detectors. *Journal of Modern Optics*, 58(3-4):174–200, 2011.

M. Jutzi and P. Michel. Hypervelocity impacts on asteroids and momentum transfer i. numerical simulations using porous targets. *Icarus*, 229:247–253, 2014.

S. Katz, A. Tal, and R. Basri. Direct visibility of point sets. In *ACM SIGGRAPH 2007 Papers*, pages 24–es. 2007.

T. Kelso et al. Analysis of the iridium 33-cosmos 2251 collision. *Advances in the Astronautical Sciences*, 135(2):1099–1112, 2009.

D. J. Kessler, N. L. Johnson, J. Liou, and M. Matney. The kessler syndrome: implications to future space operations. *Advances in the Astronautical Sciences*, 137(8):2010, 2010.

D. Kucharski, G. Kirchner, F. Koidl, C. Fan, R. Carman, C. Moore, A. Dmytrotsa, M. Ploner, G. Bianco, M. Medvedskij, et al. Attitude and spin period of space debris ENVISAT measured by satellite laser ranging. *IEEE Transactions on Geoscience and Remote Sensing*, 52(12):7651–7657, 2014.

D. Kucharski, G. Kirchner, J. Bennett, M. Lachut, K. Sośnica, N. Koshkin, L. Shakun, F. Koidl, M. Steindorfer, P. Wang, et al. Photon pressure force on space debris TOPEX/Poseidon measured by satellite laser ranging. *Earth and Space Science*, 4(10):661–668, 2017.

R. Kwok, T. Markus, N. Kurtz, A. Petty, T. Neumann, S. Farrell, G. Cunningham, D. Hancock, A. Ivanoff, and J. Wimert. Surface height and sea ice freeboard of the arctic ocean from ICESat-2: Characteristics and early results. *Journal of Geophysical Research: Oceans*, 124(10):6942–6959, 2019.

D. Lauretta, S. Balram-Knutson, E. Beshore, W. Boynton, C. Drouet d'Aubigny, D. DellaGiustina, H. Enos, D. Golish, C. Hergenrother, E. Howell, et al. Osiris-rex: sample return from asteroid (101955) bennu. *Space Science Reviews*, 212: 925–984, 2017.

M. A. Lefsky, D. J. Harding, M. Keller, W. B. Cohen, C. C. Carabajal, F. Del Bom Espirito-Santo, M. O. Hunter, and R. de Oliveira Jr. Estimates of forest canopy height and aboveground biomass using ICESat. *Geophysical Research Letters*, 32(22), 2005.

D. Liedahl, A. Rubenchik, S. B. Libby, S. Nikolaev, and C. R. Phipps. Pulsed laser interactions with space debris: target shape effects. *Advances in Space Research*, 52(5):895–915, 2013.

D. A. Liedahl, S. B. Libby, and A. Rubenchik. Momentum transfer by laser ablation of irregularly shaped space debris. In *AIP Conference Proceedings*, volume 1278, pages 772–779. American Institute of Physics, 2010.

H. Linz, D. Bhatia, L. Buinhas, M. Lezius, E. Ferrer, R. Förstner, K. Frankl, M. Philips-Blum, M. Steen, U. Bestmann, et al. Infrared astronomy satellite swarm interferometry (IRASSI): overview and study results. *Advances in Space Research*, 65(2):831–849, 2020.

R.-A. Lorbeer, M. Zwilich, M. Zabic, S. Scharring, L. Eisert, J. Wilken, D. Schumacher, M. Roth, and H.-A. Eckel. Experimental verification of high energy laser-generated impulse for remote laser control of space debris. *Scientific reports*, 8(1):1–9, 2018.

E. T. Lu and S. G. Love. Gravitational tractor for towing asteroids. *Nature*, 438 (7065):177–178, 2005.

P. Lubin, G. B. Hughes, M. Eskenazi, K. Kosmo, I. E. Johansson, J. Griswold, M. Pryor, H. O'Neill, P. Meinhold, J. Suen, et al. Directed energy missions for planetary defense. *Advances in Space Research*, 58(6):1093–1116, 2016.

H. Luo, B. Xu, H. Xu, J. Chen, and Y. Fu. Maximum detection range limitation of pulse laser radar with geiger-mode avalanche photodiode array. *Journal of Modern Optics*, 62(9):761–768, 2015a.

T. Luo, Z. Wang, D. Zhang, X. Liu, Y. Wang, and R. Yuan. Global dust distribution from improved thin dust layer detection using a-train satellite LIDAR observations. *Geophysical Research Letters*, 42(2):620–628, 2015b.

T. H. Maiman et al. Stimulated optical radiation in ruby. *Nature*, 187:493–494, 1960.

N. Mark Garcia. Space Debris and Human Spacecraft, 2021. URL `https://www.nasa.gov/mission\_pages/station/news/orbital\_debris.html`.

T. Markus, T. Neumann, A. Martino, W. Abdalati, K. Brunt, B. Csatho, S. Farrell, H. Fricker, A. Gardner, D. Harding, et al. The ice, cloud, and land elevation satellite-2 (ICESat-2): science requirements, concept, and implementation. *Remote Sensing of Environment*, 190:260–273, 2017.

J. Mason, J. Stupl, W. Marshall, and C. Levit. Orbital debris–debris collision avoidance. *Advances in Space Research*, 48(10):1643–1655, 2011.

P. Michel, M. Küppers, A. C. Bagatin, B. Carry, S. Charnoz, J. De Leon, A. Fitzsimmons, P. Gordo, S. F. Green, A. Hérique, et al. The esa hera mission: detailed characterization of the dart impact outcome and of the binary asteroid (65803) didymos. *The planetary science journal*, 3(7):160, 2022.

J. Müller, T. W. Murphy, U. Schreiber, P. J. Shelus, J.-M. Torre, J. G. Williams, D. H. Boggs, S. Bouquillon, A. Bourgoin, and F. Hofmann. Lunar Laser Ranging: a tool for general relativity, lunar geophysics and earth science. *Journal of Geodesy*, 93(11):2195–2210, 2019.

A. L. Neuenschwander and L. A. Magruder. Canopy and terrain height retrievals with ICESat-2: A first look. *Remote Sensing*, 11(14):1721, 2019.

NREL. National renewable energy laboratory solar spectra. URL `https://www.nrel.gov/grid/solar-resource/spectra.html`. Retrieved: November 2020.

U. Paffrath, C. Lemmerz, O. Reitebuch, B. Witschas, I. Nikolaus, and V. Freudenthaler. The airborne demonstrator for the direct-detection doppler wind LIDAR ALADIN on ADM-Aeolus. part II: Simulations and Rayleigh receiver

radiometric performance. *Journal of Atmospheric and Oceanic Technology*, 26 (12):2516–2530, 2009.

C. Pardini and L. Anselmo. Physical properties and long-term evolution of the debris clouds produced by two catastrophic collisions in earth orbit. *Advances in Space Research*, 48(3):557–569, 2011.

J. I. Peltoniemi, O. Wilkman, M. Gritsevich, M. Poutanen, A. Raja-Halli, J. Näränen, T. Flohrer, and A. Di Mira. Steering reflective space debris using polarised lasers. *Advances in Space Research*, 67(6):1721–1732, 2021.

C. Phipps and J. Luke. Diode laser-driven microthrusters: a new departure for micropropulsion. *AIAA Journal*, 40(2):310–318, 2002.

C. Phipps, G. Albrecht, H. Friedman, D. Gavel, E. George, J. Murray, C. Ho, W. Priedhorsky, M. Michaelis, and J. Reilly. ORION: Clearing near-earth space debris using a 20-kw, 530-nm, earth-based, repetitively pulsed laser. *Laser and Particle Beams*, 14(1):1–44, 1996.

C. R. Phipps. L'ADROIT–a spaceborne ultraviolet laser system for space debris clearing. *Acta Astronautica*, 104(1):243–255, 2014.

C. R. Phipps, J. R. Luke, D. J. Funk, D. S. Moore, J. Glownia, and T. Lippert. Measurements of laser impulse coupling at 130 fs. In *High-Power Laser Ablation V*, volume 5448, pages 1201–1209. International Society for Optics and Photonics, 2004.

C. R. Phipps, M. Boustie, J.-M. Chevalier, S. Baton, E. Brambrink, L. Berthe, M. Schneider, L. Videau, S. A. Boyer, and S. Scharring. Laser impulse coupling measurements at 400 fs and 80 ps using the LULI facility at 1057 nm wavelength. *Journal of Applied Physics*, 122(19):193103, 2017.

O. Reitebuch, C. Lemmerz, E. Nagel, U. Paffrath, Y. Durand, M. Endemann, F. Fabre, and M. Chaloupy. The airborne demonstrator for the direct-detection doppler wind LIDAR ALADIN on ADM-Aeolus. part I: Instrument design

and comparison to satellite instrument. *Journal of Atmospheric and Oceanic Technology*, 26(12):2501–2515, 2009.

B. Sallé, O. Gobert, P. Meynadier, M. Perdrix, G. Petite, and A. Semerok. Femtosecond and picosecond laser microablation: ablation efficiency and laser microplasma expansion. *Applied Physics A*, 69(1):S381–S383, 1999.

J. Sang and J. C. Bennett. Achievable debris orbit prediction accuracy using laser ranging data from a single station. *Advances in Space Research*, 54(1): 119–124, 2014.

J. R. Sanmartín, A. Sánchez-Torres, S. Khan, G. Sánchez-Arriaga, and M. Charro. Optimum sizing of bare-tape tethers for de-orbiting satellites at end of mission. *Advances in Space Research*, 56(7):1485–1492, 2015.

W. O. Schall. Orbital debris removal by laser radiation. *Acta Astronautica*, 24: 343–351, 1991.

S. Scharring, J. Wilken, and H.-A. Eckel. Laser-based removal of irregularly shaped space debris. *Optical Engineering*, 56(1):011007, 2016.

B. E. Schutz, H. J. Zwally, C. A. Shuman, D. Hancock, and J. P. DiMarzio. Overview of the ICESat mission. *Geophysical Research Letters*, 32(21), 2005.

J. B. Sloane and R. J. Sedwick. Direct force measurement of pulsed laser ablation of asteroid simulants. *Journal of Propulsion and Power*, 36(4):551–559, 2020.

B. Smith, H. A. Fricker, N. Holschuh, A. S. Gardner, S. Adusumilli, K. M. Brunt, B. Csatho, K. Harbeck, A. Huth, T. Neumann, et al. Land ice height-retrieval algorithm for NASA's ICESat-2 photon-counting laser altimeter. *Remote Sensing of Environment*, 233:111352, 2019.

D. E. Smith, M. T. Zuber, G. B. Jackson, J. F. Cavanaugh, G. A. Neumann, H. Riris, X. Sun, R. S. Zellar, C. Coltharp, J. Connelly, et al. The Lunar Orbiter Laser Altimeter investigation on the lunar reconnaissance orbiter mission. *Space Science Reviews*, 150(1):209–241, 2010a.

D. E. Smith, M. T. Zuber, G. A. Neumann, F. G. Lemoine, E. Mazarico, M. H. Torrence, J. F. McGarry, D. D. Rowlands, J. W. Head III, T. H. Duxbury, et al. Initial observations from the Lunar Orbiter Laser Altimeter (LOLA). *Geophysical Research Letters*, 37(18), 2010b.

Z. Sodnik, B. Furch, and H. Lutz. Optical intersatellite communication. *IEEE Journal of Selected Topics in Quantum Electronics*, 16(5):1051–1057, 2010.

SpaceX Falcon 9 Capabilities and Services. URL `https://www.spacex.com/media/Capabilities&Services.pdf`. Retrieved: May 2021.

A. G. Straume, A. Elfving, D. Wernham, F. de Bruin, T. Kanitz, D. Schuettemeyer, J. von Bismarck, F. Buscaglione, O. Lecrenier, and P. McGoldrick. ESA's spaceborne LIDAR mission ADM-Aeolus; project status and preparations for launch. In *EPJ Web of Conferences*, volume 176, page 04007. EDP Sciences, 2018.

X. Sun, G. A. Neumann, J. B. Abshire, and M. T. Zuber. Mars 1064 nm spectral radiance measurements determined from the receiver noise response of the Mars Orbiter Laser Altimeter. *Applied Optics*, 45(17):3960–3971, 2006.

M. B. Syal, D. S. Dearborn, and P. H. Schultz. Limits on the use of nuclear explosives for asteroid deflection. *Acta Astronautica*, 90(1):103–111, 2013.

M. B. Syal, J. M. Owen, and P. L. Miller. Deflection by kinetic impact: Sensitivity to asteroid properties. *Icarus*, 269:50–61, 2016.

N. Thiry and M. Vasile. Statistical multi-criteria evaluation of non-nuclear asteroid deflection methods. *Acta Astronautica*, 140:293–307, 2017a.

N. Thiry and M. Vasile. Theoretical peak performance and optical constraints for the deflection of an S-type asteroid with a continuous wave laser. *Advances in Space Research*, 59(5):1353–1367, 2017b.

K. Thyagarajan and A. Ghatak. *Lasers: Fundamentals and Applications*. Springer Science & Business Media, 2010.

D. Tran, A. Yogo, H. Nishimura, and K. Mori. Impulse and mass removal rate of aluminum target by nanosecond laser ablation in a wide range of ambient pressure. *Journal of Applied Physics*, 122(23):233–304, 2017.

G. Tyler, V. Eshleman, J. Anderson, G. Levy, G. Lindal, G. Wood, and T. Croft. Radio science with Voyager 2 at Saturn: Atmosphere and ionosphere and the masses of Mimas, Tethys, and Iapetus. *Science*, 215(4532):553–558, 1982.

G. Tyler, D. Sweetnam, J. Anderson, J. Campbell, V. Eshleman, D. Hinson, G. Levy, G. Lindal, E. Marouf, and R. Simpson. Voyager 2 radio science observations of the Uranian system: Atmosphere, rings, and satellites. *Science*, 233(4759):79–84, 1986.

M. Vasile and C. A. Maddock. On the deflection of asteroids with mirrors. *Celestial Mechanics and Dynamical Astronomy*, 107(1):265–284, 2010.

M. Vetrisano, J. Branco, J. P. Sanchez Cuartielles, D. Garci Yarnoz, and M. L. Vasile. Deflecting small asteroids using laser ablation: deep space navigation and asteroid orbit control for LightTouch2 mission. In *AIAA Guidance, Navigation, and Control (GNC) Conference, Boston, USA*, page 5250, 2013.

M. Vetrisano, N. Thiry, and M. Vasile. Detumbling large space debris via laser ablation. In *2015 IEEE Aerospace Conference, Montana, USA*, pages 1–10. IEEE, 2015.

M. Vetrisano, C. Colombo, and M. Vasile. Asteroid rotation and orbit control via laser ablation. *Advances in Space Research*, 57(8):1762–1782, 2016.

L. Walker, M. Di Carlo, C. Greco, M. Vasile, and M. Warden. A mission concept for the low-cost large-scale exploration and characterisation of near earth objects. *Advances in Space Research*, 67(11):3880–3908, 2021.

B. Wang. Laser ablation impulse generated by irradiating aluminum target with nanosecond laser pulses at normal and oblique incidence. *Applied Physics Letters*, 110(1):014101, 2017.

T. Wang. Analysis of debris from the collision of the Cosmos 2251 and the Iridium 33 satellites. *Science & Global Security*, 18(2):87–118, 2010.

S.-i. Watanabe, Y. Tsuda, M. Yoshikawa, S. Tanaka, T. Saiki, and S. Nakazawa. Hayabusa2 mission overview. *Space Science Reviews*, 208:3–16, 2017.

R. C. Wiens, S. Maurice, B. Barraclough, M. Saccoccio, W. C. Barkley, J. F. Bell, S. Bender, J. Bernardin, D. Blaney, J. Blank, et al. The ChemCam instrument suite on the Mars Science Laboratory (MSL) rover: Body unit and combined system tests. *Space Science Reviews*, 170(1):167–227, 2012.

F. Y. Yang, B. Nelson, J. Aziz, R. Carlino, A. D. Perez, N. Faber, C. Foster, C. Frost, C. Henze, A. G. Karacalıoğlu, et al. LightForce photon-pressure collision avoidance: Efficiency analysis in the current debris environment and long-term simulation perspective. *Acta Astronautica*, 126:411–423, 2016.

D. Yeomans, P. Antreasian, J.-P. Barriot, S. Chesley, D. Dunham, R. Farquhar, J. Giorgini, C. Helfrich, A. Konopliv, J. McAdams, et al. Radio science results during the NEAR-Shoemaker spacecraft rendezvous with Eros. *Science*, 289 (5487):2085–2088, 2000.

D. K. Yeomans, J.-P. Barriot, D. Dunham, R. Farquhar, J. Giorgini, C. Helfrich, A. Konopliv, J. McAdams, J. Miller, W. Owen Jr, et al. Estimating the mass of asteroid 253 Mathilde from tracking data during the NEAR flyby. *Science*, 278(5346):2106–2109, 1997.

X.-T. Zhao, F. Tang, B. Han, and X.-W. Ni. The influence of laser ablation plume at different laser incidence angle on the impulse coupling coefficient with metal target. *Journal of Applied Physics*, 120(21):213103, 2016.

M. T. Zuber, D. E. Smith, R. J. Phillips, S. C. Solomon, W. B. Banerdt, G. A. Neumann, and O. Aharonson. Shape of the northern hemisphere of Mars from the Mars Orbiter Laser Altimeter (MOLA). *Geophysical Research Letters*, 25 (24):4393–4396, 1998.

M. T. Zuber, D. E. Smith, R. S. Zellar, G. A. Neumann, X. Sun, R. B. Katz, I. Kleyner, A. Matuszeski, J. F. McGarry, M. N. Ott, et al. The Lunar Reconnaissance Orbiter laser ranging investigation. *Space Science Reviews*, 150(1): 63–80, 2010.